UNIVERSITY OF CALIFORNIA, SAN DIEGO

Strong correlation effects in itinerant systems and space-time symmetry in dynamical condensed matter systems

A dissertation submitted in partial satisfaction of the
requirements for the degree
Doctor of Philosophy

in

Physics

by

Shenglong Xu

Committee in charge:

Professor Congjun Wu, Chair
Professor Daniel Arovas
Professor Jorge Hirsch
Professor John McGreevy
Professor Justin Roberts

2017

The dissertation of Shenglong Xu is approved, and it is acceptable in quality and form for publication on microfilm and electronically:

_____

_____

_____

_____

_____

Chair

University of California, San Diego

2017

DEDICATION

To my parents who love me and stimulate my curiosity towards nature,

and my fiancée who is always there for me.

EPIGRAPH

And lost be the day to us

in which a measure hath not been danced.

—Friedrich Nietzsche

TABLE OF CONTENTS

LIST OF FIGURES

LIST OF TABLES

ACKNOWLEDGEMENTS

First, I would like to thank my advisor, Professor Congjun Wu. The past four years working with him fundamentally influences my perspective and taste of research. He points me to the power and importance of physical picture and intuition with his vivid understanding of condensed matter physics and the ability to elucidate complex phenomena in a simple manner. He has greatly expanded my horizon and gives me the freedom to explore many aspects of the condensed matter physics. Without him, all of work presented in this thesis would not be possible.

I am also grateful to Professor Nandini Trivedi, who kindly advised me for two years. She and Professor Mohit Randeria guided me into the field of condensed matter theory. And Professor John McGreevy. I benefit tremendously from his open door policy. He always answers my questions with great patience. To me, John is a knowledgeable friend that I am never tired to discuss physics with. And Professor Daniel Arovas. I will always remember all the insightful discussions in his office, on the way back forth to UC Irvine and over the tables in Pho La Jolla. I am grateful for his encouragement and help on my postdoc application. And Professor Yi Li. I am not lucky enough to have overlap with her in UCSD, but benefit greatly from her previous work. Her cheerful personality and the perseverance in pursuing physics deeply touch me. I would also like to acknowledge my committee members who encourage me and give feedbacks on my thesis work.

Chapter 2 contains material published by American Physical Society in: Shenglong Xu, Yi Li and Congjun Wu, "Sign-Problem-Free Quantum Monte Carlo Study on Thermodynamic Properties and Magnetic Phase Transitions in Orbital-Active Itinerant Ferromagnets", Physical Review X 5(2), 021032, 2015. The dissertation author was the primary investigator and author of this paper.

Chapter 3 contains material from the following preprint being prepared for sub-

mission for publication: Shenglong Xu, Julio Barreiro, Yu Wang, and Congjun Wu. ”Interaction effects from the parity of N in SU (N) symmetric fermion lattice systems.” arXiv:1707.01463 (2017). The dissertation author was the primary investigator and author of this paper.

Chapter 4 contains material from the following preprint being prepared for submission for publication: Shenglong Xu, Congjun Wu, ”Space-time crystal and space-time group symmetry”, arXiv:1703.03388 (2017). The dissertation author was the primary investigator and author of this paper.

I am indebted to my other collaborators, Professor Brian Swingle, Professor Julio Barreiro, Professor Da Wang and Professor Tianxing Ma. Finally, I would like to thank all my friends in graduate school, especially Matt Warren, Chuck Bryant , Hudson Smith, Daniel Ben-Zion, Emiliy Nardoni, Devin Cela, Elizabeth Wicks, Wang Yang, Chao Xu, Gufeng Zhang, Zhiyuan Sun. We grew up together in the past few years and went through all the happy and difficult moments. With their company, I am not lonely on the way pursuing my love of physics.

VITA

$2013 \sim 2017$	Ph. D. in Physics, University of California, San Diego
$2011 \sim 2013$	Ohio State University, Columbus, Ohio
$2007 \sim 2011$	B. S. in Physics, Nanjing University, Nanjing, China

PUBLICATIONS

S. Xu, Y. Li, and C. Wu, "Sign-Problem-Free Quantum Monte Carlo Study on Thermodynamic Properties and Magnetic Phase Transitions in Orbital-Active Itinerant Ferromagnets", Phys. Rev. X 5, 021032 (2015).

S. Xu, C. Wu, "Space-time crystal and space-time group symmetry", arxiv 1703.03388 (2017).

W. Yang, J. Wu, **S. Xu**, Z. Wang, C. Wu, "Quantum spin dynamics of the axial antiferromagnetic spin-12 XXZ chain in a longitudinal magnetic field", arxiv 1702.01584

S. Xu, J. T. Barreiro, Y. Wang and C. Wu, "Interaction effects from the parity of N in SU(N) symmetric fermion lattice systems", arxiv 1701.01463 (2017)

W. Zhe, J. Wu, W. Yang, A. K. Bera, D. Kamenskyi, A. T. M. Islam, **S. Xu** et al. "Experimental Observation of Bethe Strings." arxiv 1706.04181 (2017).

D. Wang, **S. Xu**, Y. Wang, and C. Wu, "Detecting edge degeneracy in interacting topological insulators through entanglement entropy", Phys. Rev. B 91, 115118 (2015).

G. Yang, **S. Xu**, W. Zhang, T. Ma, and C. Wu, "Room-temperature magnetism on the zigzag edges of phosphorene nanoribbons", Phys. Rev. B 94, 075106 (2016).

B. Swingle, J. McGreevy, and **S. Xu**, "Renormalization group circuits for gapless states", Phys. Rev. B 93, 205159 (2016).

Z. Wang, J. Wu, **S. Xu**, *et. al*, "From confined spinons to emergent fermions: Observation of elementary magnetic excitations in a transverse-field Ising chain", Phys. Rev. B 94, 125130 (2016).

S. Xu, *et. al*, "A molecular understanding of the gas-phase reduction and doping of graphene oxide" Nano Res. 5, 361 (2012).

ABSTRACT OF THE DISSERTATION

Strong correlation effects in itinerant systems and space-time symmetry in dynamical condensed matter systems

by

Shenglong Xu

Doctor of Philosophy in Physics

University of California, San Diego, 2017

Professor Congjun Wu, Chair

One of the central goals of condensed matter theory is to understand the behavior of electrons under various circumstances. This dissertation focuses on the some relatively unexplored effects brought by lattices, in a general setting.

One ingredient that lattices introduce is the orbital degrees of freedom, resulting from the interaction between electrons and background ions. We have non-perturbatively studied a strongly coupled multi-orbital electron liquid, which has a fully polarized ground state. Both Hund's coupling and electron itinerancy are essential to building up the global spin coherence. At finite temperature, the system exhibits both Curie-Weiss

type spin susceptibility and finite compressibility, demonstrating the coexistence of spin coherence and charge incoherence. At low temperature, the single particle excitation extends over the entire Brillouin zone rather than the vicinity of the Fermi surface due to the spin fluctuation.

Another dramatic effect of lattices on electrons is the formation of Mott insulators. We consider a special type of Mott insulators occurring at non-integer fillings, which has a finite single-particle gap but strong local charge fluctuation. As an example, we studied 1D Hubbard model with SU(N) symmetry at half-filling. The systems are insulating for all values of N, but the filling is half-integer when N is odd. We demonstrate that the systems with N even and N odd exhibit distinct energy scales of charge and spin gaps. In the case of odd N, the local charge fluctuation leads to spin gap much greater than the super exchange energy scale. The difference between the systems with opposite parity of N is gradually smeared out as N increases.

The symmetry of lattices can also enforce band touchings and band crossing, leading to nodal-line and nodal-point semi-metals. We explore the symmetry constraints on electrons imposed by generalized lattices with space-time mixing periodicities. which include the Floquet lattice systems as a special case. Compared to space and magnetic groups, the symmetry group of such systems is augmented by "time-screw" rotations and "time-glide" reflections involving fractional time translations. A complete classification of the 13 space-time groups in 1+1D and 275 space-time groups in 2+1D are performed. Kramers-type degeneracy can arise from space-time symmetries without the half-integer spinor structure, which constrains the winding number patterns of spectral dispersions. In 2+1D, non-symmorphic space-time symmetries enforce spectral degeneracies, leading to protected Floquet semi-metal states.

Chapter 1

Introduction

Condensed matter theory is a subject to study collective phenomena from the microscopic degrees of freedom. One of the central goals is to understand the behavior of electrons as much as possible, motivated by the following fundamental phenomena found in electronic materials: metal, insulator, magnetism, superconductivity and quantum Hall. Enormous efforts have been made to explain these phenomena, and various paradigms have been established.

Among all these phenomena, the metallic behavior of electrons is special because of the vanishing single particle gap. The current understanding of metal is based on Landau's Fermi liquid (FL) theory, which is one of the most successful paradigms of interacting electrons [1]. It states that interacting fermions are adiabatically connected to noninteracting fermions, and the Fermi surfaces are robust against interaction. The role of interaction is to reduce the quasi-particle weight Z from 1, the value of free fermions. Using this picture of quasi-particle, one can explain the thermodynamic properties and transport properties, such as the temperature dependence of heat capacities, spin susceptibilities, and conductivities, observed in a wide variety of metals.

Since Fermi surfaces are so robust in electrons systems, it is natural to ask what

conditions can dramatic change this picture. There are quite a few possibilities, including considering attractive interactions[2], magnetic field[3], coupling the electrons to bosonic degrees of freedom[4], disorder[5], lattice, etc. This dissertation will be mainly focused on the effects of lattice symmetries.

In materials, electrons are moving in the crystals formed by ions. The orbital degrees of freedom arise due to the Coulomb attraction between the electrons and ions. In the atomic limit, the orbitals are labeled by the angular moments, whereas in the presence of the crystal field, the orbitals are labeled by the irreducible representations (irrep) of local point group symmetry, i.e. T_{2g}, and E_g and so on. As promised by the symmetry, orbitals within one irrep are degenerate. These degenerate orbitals do not simply lead to multi copies of Fermi liquid, but significantly affect both the dispersion and the interaction. First, due to the shapes of orbitals, the kinetic term is not isotropic anymore and neither the Fermi surface. In principle, there are also hybridization between orbitals, if allowed by the symmetry, and the Fermi surface can carry orbital texture. Second, the inter-orbital interaction, especially the Hund's rule coupling, is not considered within the framework of FL theory, which was developed to describe liquid Helium. The Hund's coupling favors that local spins in different orbitals point to the same direction. Since the kinetic energy usually favors unpolarized state, the local polarization may not be sufficient to induce fully polarized state. In this case, the electron systems remain paramagnetic, and what the Hund's coupling does is suppressing charge coherence and reduce the quasi-particle weight [6]. On the other hand, if under certain conditions, the ground state of the system becomes polarized because of the local polarization, then the Hund's coupling is simply zero in the sub Hilbert space of the fully polarized states, and the quasi-particle weight is restored. In Chapter 2, we study a particular model where the Hund's coupling does lead to global polarization. We demonstrate that the collective effect of Hund's coupling, orbital anisotropy, electron itineracy and strong correlation

gives rise to the fully polarized state. We further study the thermodynamic behavior of the resulting orbital-active itinerant ferromagnet non-perturbatively using Quantum Monte Carlo.

Another effect of lattices is to gap out the charge excitation in the Fermi Liquid, leading to insulating states, which can be classified into band insulators and Mott insulators. The Mott insulators are the consequences of interaction and can be understood in the atomic limit. Consider the simplest case that each atom only contains one orbital which is filled with one electron [7]. Then one electron needs to overcome a barrier due to Coulomb repulsion to move to its neighboring site, and it also takes a finite amount of energy to put one extra electron into the system. Therefore the system is an insulator but would be metallic if the interaction is turned off. This seemly oversimplified picture of atomic Mott insulator is the starting point to understand magnetic properties of many materials. One can perform second order perturbation theory on all the degenerate states of different spin configurations and obtain an effective Hamiltonian, the Heisenberg model. It describes the antiferromagnetic interaction between neighboring spin with the super exchange energy $J = 4t^2/U$ where t is energy scale on the order of the Fermi energy and U is on the order of single particle charge gap. Mott insulator can also happen at the weak coupling limit due to Fermi surface nesting, such as in square lattice at half-filling with nearest neighboring hopping. In this situation, the system is an antiferromagnetic Mott insulator for any positive repulsion. The Mott insulator in the weakly coupling limit is adiabatically connected to the strong Mott insulator in the atomic limit, as confirmed by Quantum Monte Carlo study [8]. There are also other cases where Mott insulators occur at non-integer fillings [9, 10] and therefore are not adiabatically connected to the atomic Mott insulator. The Mott insulators with non-integer fillings exhibit strong local charge fluctuations even in the strong coupling limit, and the usual approach to analyze the magnetic properties by thinking about virtual hopping fails. In chapter 3, we study

one example of such non-integer filling Mott insulators and demonstrate that in that case, the energy scale in the spin channel is proportional to the Fermi energy, much higher than the super exchange energy.

The lattice symmetry can also significantly affects the shape of the Fermi surface and even change its dimensionality, leading to nodal-line and nodal-point semi-metals. For example, nonsymmorphic symmetries, which are combinations of fractional translations and point group symmetries, can enforce band degeneracies at high symmetry points in the Brillouin zone. The reason is that the wave functions at these specific points are in the projective representation of the point group symmetries that leave the momentum invariant, and projective representation is alway more than one dimension [11]. The nonsymmorphic symmetry also enforces crossing of two bands if they carry different eigenvalues of the symmetry operation, resulting in nodal points or nodal lines but not necessary at high symmetry K point [12]. Furthermore, point group symmetry alone can also protect nodal point on certain kinds of lattices. For example, the single-particle wave functions on honeycomb lattice at A and B sublattices with momentum K are the two-dimensional representation of the C_{3v} point group symmetry of the lattice and thus have to be degenerate. Inspired by these interesting effect of lattice symmetry, we generalize the space group symmetry to the space-time group symmetry and investigate the constraints of these exotic symmetries on the behavior of electrons subjected to periodic driving force. This part is included in Chapter 4.

These effects of lattices are not independent but interplay with each other. There are multi-orbital Mott insulators with orbital orders, for example, see [13], and even more exotic spin-orbit coupled Mott insulators. In some lattices, flat bands appear in the spectrum, giving rise to ferromagnetism [14] and Mott insulators with enlarged unit cell [10], stabilized by interactions. The strain field in lattices mimics magnetic field and simulates Landau levels. The idea of topology that was originally applied in the

field quantum Hall has been used to further classify band insulators, Mott insulators, semi-metals [15]. The presence of nodal structure in the Fermi surface modifies the usual partial wave analysis of the pairing symmetry in superconductors due to topological property of nodal points [16] or nodal lines. All the different aspects of the collective behavior of electron entangle together and constitute the current vivid understanding of electrons, and there is still enormous unknown territory to explore.

We have explained the motivation for the works presented in this dissertation and their relation to previous research. In the following, we summarize the main results of these works.

In chapter 2, we present a comprehensive study of a strongly coupled Curie-Weiss metal, which exhibits ferromagnetic ground state and unusual finite temperature properties. The microscopic mechanism of itinerant ferromagnetism is a long-standing problem due to the lack of non-perturbative methods to handle strong magnetic fluctuations of itinerant electrons. We have non-pertubatively studied thermodynamic properties and magnetic phase transitions of a two-dimensional multi-orbital Hubbard model exhibiting ferromagnetic ground states. Quantum Monte-Carlo simulations are employed, which are proved in a wide density region free of the sign problem usually suffered by simulations for fermions. Both Hund's coupling and electron itinerancy are essential for establishing the ferromagnetic coherence. No local magnetic moments exist in the system as a priori, nevertheless, the spin channel remains incoherent showing the Curie-Weiss type spin magnetic susceptibility down to very low temperatures at which the charge channel is already coherent exhibiting a weakly temperature-dependent compressibility. For the SU(2) invariant systems, the spin susceptibility further grows exponentially as approaching zero temperature in two dimensions. In the paramagnetic phase close to the Curie temperature, the momentum space Fermi distributions exhibit strong resemblance to those in the fully polarized state. The long-range ferromagnetic ordering appears when the symmetry is

reduced to the Ising class, and the Curie temperature is accurately determined. These simulations provide helpful guidance to searching for novel ferromagnetic materials in both strongly correlated d-orbital transition metal oxide layers and the p-orbital ultra-cold atom optical lattice systems.

In chapter 3, we study the strong correlation effects for Mott insulating states, especially insulating states with non-integer fillings. We argue that due to the residue local charge fluctuation, the energy scale in the spin channel is higher than the super exchange energy scale. The simplest example is the SU(N) symmetric Hubbard chains at *half* filling (N/2 particles per site on average). Weak interaction analysis [9] tells that the systems are insulating for all values of N, although the filling is half-integer when N is odd. We systematically study the effects of the large symmetry on the non-integer Mott insulators and compare them with their close relatives, the SU(N) Hubbard chains with N even. As N increases, the density per component stays the same, and the large-N physics is fundamentally different from $1/N$ filling. The difference between even-N and odd-N systems is most pronounced for small values of N and strong interactions, affecting both charge and spin channels. The odd-N chains, which are Mott insulators at half-integer filling, exhibit a strong tendency to dimerization at the temperature comparable to the Fermi energy due to the local charge fluctuation. As N increases, the interaction effects are suppressed and the boundary between the two sets of Hubbard chains is smeared out by the large symmetry.

In chapter 4, we focus on the space-time symmetry of dynamic condensed matter system. Crystal structures and the Bloch theorem play a fundamental role in condensed matter physics. The lattice symmetries significantly affects the the properties of the Fermi surface, leading to band insulators, nodal point semi-metals and nodal line semi-metals. We propose "space-time" crystals exhibiting the general intertwined space-time periodicities in $D+1$ dimensions, which include the Floquet lattice systems as a special

case. Their crystal symmetry structures are described by "space-time" groups. The full discrete space-time symmetries of space-time crystals form groups – dubbed "space-time" groups, which are generalizations of space groups for static crystals by including "time-screw" and "time-glide" operations. A complete classification of the 13 space-time groups in 1+1 D, and 275 space-time groups in 2+1 D are performed. We demonstrate that the non-symmorphic space-time symmetry operations, similar to their static space-group counterparts, lead to spectral degeneracies for periodically driven systems, even when the instantaneous spectra are gapped at any given time t.

Chapter 2

Strongly-coupled itinerant systems: Curie-Weiss metal and the role of Hund's coupling

2.1 Introduction

Itinerant ferromagnetism (FM) is one of the central topics of condensed matter physics [17, 18, 19, 20, 21, 22, 23, 24, 25, 26, 27, 28, 29, 30, 31, 32, 33, 34, 35, 36, 37, 38, 39]. It has also become a research focus both experimental and theoretical of ultra-cold atom physics [40, 41, 42, 43, 44, 45, 46, 47]. The mechanism of itinerant FM has been a long-standing problem. Stoner proposed the exchange interaction among electrons with parallel spins as the driving force for itinerant FM [17]. Along this direction, the local density approximation (LDA) of the density functional theory has achieved great success [48, 49]. For example, the ground state magnetic moments of FM metals can be calculated accurately [50]. The implementation of correlation effects in LDA has also been improved by the methods of LDA+U [51], LDA+DMFT(dynamical mean-field

theory) [52, 53, 54], and LDA+GP (Gutzwiller projection) [55, 56, 57].

Nevertheless, itinerant FM systems are also strongly correlated, and their physics is often non-perturbative. Usually repulsive interactions need to be sufficiently strong to overcome the kinetic energy cost of polarizing electron spins, and thus itinerant FM has no well-controlled weak-coupling starting point. The Stoner criterion overlooks correlation effects among electrons with opposite spins [39]: Electrons can delicately organize their wavefunctions to reduce repulsions and still remain unpolarized even in the presence of strong interactions. For example, the Lieb-Mattis theorem proves that the ground state of a rigorously one-dimensional (1D) system is a spin singlet no matter how strong the interaction is [21].

It is more appropriate to start with electron orbitals to construct lattice model Hamiltonians to address the strong correlation aspect of itinerant FM. Exact theorems establishing FM, which are usually based on lattice models, are indispensable to provide reference points for further investigations. Well-known examples include the Nagaoka theorem [22, 58, 59, 60, 61, 62], which applies to the infinite U Hubbard models in two and above dimensions with doping a single hole on the half-filled background, and the "flat-band" FM in certain lattices with dispersionless band structures [14, 29]. In the former case, FM arises because the spin polarized background maximally facilitates the hole's coherent hopping, while in the latter case, the band flatness reduces the kinetic energy cost for polarizing spin to zero.

One central issue of itinerant FM is the role of orbital degeneracy which widely exists in FM metals. Hund's coupling is a prominent feature in multi-orbital systems, which favors electrons on the same site to align their spins. However, Hund's coupling is local physics which usually cannot polarize itinerant electrons in the absence of local moments. Under what precise conditions Hund's coupling can lead to the global FM coherence in itinerant systems is still an open question.

The difficulty in achieving unambiguous FM ground states is only one side of the story of strongly-correlated itinerant FM, the finite-temperature thermodynamic properties are another challenge [63, 26, 64, 7]. At first looking, it might not look so striking: the ferromagnetic susceptibilities show the standard mean-field Curie-Weiss (CW) law in the off-critical region as

$$\chi(T) = \frac{C}{T - T_0}, \tag{2.1}$$

where C is the Curie constant [65] and T_0 is the Curie temperature at the mean-field level. The CW law manifests spin incoherence, which is common in the paramagnetic state based on local moments. But it is difficult to understand in itinerant FM metals still possessing Fermi surfaces. For example, the transport and the charge channel properties, such as resistance and compressibility, remain metallic, *i.e.*, they are featured by the Fermi surface physics.

Within the itinerant picture, the Pauli magnetic susceptibility augmented by the random phase approximation (RPA) yields $\chi(T) \propto 1/(T^2 - T_0^2)$, but it is not commonly observed in experiments [26, 64, 7]. In fact, the CW law in FM metals applies to a wide range of temperatures $T_f \gg T > T_0$ (T_f is the Fermi temperature) which shows spin-incoherence well below T_f. The reason is that RPA treats the paramagnetic phase as a weakly correlated Fermi liquid state with slightly thermally broadened Fermi distributions. Actually, this phase is rather complicated: Dynamic FM domains strongly fluctuate, which is beyond the RPA description and is difficult to handle analytically. The paramagnetic state of itinerant FM exhibits much higher entropy capacity than the usual weakly correlated paramagnetic Fermi liquid state, which significantly suppresses the genuine Curie temperature T_c, or, the renormalized one, away from the mean-field value T_0. Consequently, T_c is often significantly overestimated by weak coupling approaches

[26, 64, 7].

A key question is how itinerant systems can exhibit the CW law and further develop FM purely based on itinerant electrons without involving local moments such that the charge channel remains coherent? Significant efforts have been made, including the self-consistent renormalization theory including spin mode coupling [25, 63, 26], the direct exchange from the Coulomb integral [27, 66], spin incoherence due to Hund's coupling [67], and the orbital-selective Mott transition [68, 69]. An important progress is that the CW law can be obtained from the combined method of LDA+DMFT [70] away from the critical region. However, none of these methods are non-perturbative in nature.

Another issue is the nature of the FM phase transitions in FM metals, which has been been widely studied but is still under intensive debates [24, 30, 32, 34, 35, 33]. Compared to the superconducting phase transitions in which the fermion degree of freedom is gapped below transition temperatures, the FM phase transitions are more involved because systems remain gapless across transitions due to the existence of Fermi surfaces. The FM domain fluctuations combined with the Landau damping of particle-hole excitations around Fermi surfaces complicates FM transitions. It would be important to perform a non-perturbative study.

Recently, the ground states of a multi-orbital Hubbard model have been proved fully spin polarized in the strong coupling regime in the 2D square and 3D cubic lattices [37]. It is showed that inter-orbital Hund's coupling combined with electron itinerancy in the quasi-1D band structure drive the FM ground states. Compared to the Nagaoka FM, this new theorem proves a stable FM phase with nodeless ground state wavefunctions over the entire electron density region $0 < n < 2$, where n is the occupation number per site, thus it sets up a solid starting point for further studying the strong correlation aspect of itinerant FM. It also opens up the possibility of performing sign-problem free quantum Monte Carlo (QMC) simulations away from half-filling by employing the bases under

which the many-body Hamiltonians satisfy the Perron-Frobenius condition.

Although this theorem only sets up the ground state properties, it establishes an unambiguous FM phase as a starting point for further studying both thermodynamic properties and magnetic phase transitions over a wide region of electron density. In order to handle the strong magnetic fluctuations, QMC simulations would be the ideal method, however, they usually suffer the notorious sign problem for fermions and thus are generally speaking inapplicable for itinerant FM. Remarkably, we prove that for the systems in which the ground state FM theorem mentioned above [37] applies, the fermion sign problem can be eliminated in the entire electron density region. This provides a new opportunity to study the finite temperature thermodynamic properties and magnetic phase transitions in an asymptotically exact way.

For later convenience, we briefly discuss the FM critical fluctuations which are particularly important in two-dimensions. According to the Landau-Ginzburg-Wilson paradigm of critical phenomena, T_c is suppressed from T_0 but remains finite in 3D. As T is lowered from T_0 and approaches T_c, the system crosses over from the mean-field region to the critical region, and $\chi(T) \propto (T - T_c)^{-\gamma}$ due to non-Gaussian fluctuations and γ is the critical exponent. In 2D, T_c remains finite if the system symmetry is reduced to the Ising class, or, the easy axis class. However, for the isotropic class, thermal fluctuations suppress T_c to zero according to the Mermin-Wagner theorem [71]. Nevertheless, even in this case the mean-field T_0 is still an important temperature scale below which the FM order develops its magnitude. However, the orientation fluctuations of the FM order suppress the long-rang-order. In other words, this region is characterized by fluctuating FM domains and the correlation length increases exponentially as lowering temperatures. Consequently, the FM susceptibility deviates from the CW law and crosses over into an exponential growth.

In this article, we will present a systematic non-perturbative study on thermo-

dynamic properties and magnetic phase transitions of itinerant FM by performing the sign-problem free QMC simulations. Our results show that itinerant FM can indeed exhibit both spin incoherence and charge coherence simultaneously without forming local moments. In other words, the system exhibits the feature of the CW metal as a combined effect of Hund's coupling and electron itinerancy. The model we simulate can be realized in both d-orbital transition metal oxide layer and p-orbital ultra-cold atom optical lattices, which do not contain local moments as a priori. The spin magnetic susceptibility exhibits the CW law as a signature of spin incoherence, while, the compressibility weakly depends on temperature as a consequence of itinerancy. The mean-field Curie temperature T_0 is extracted based on the CW law in the off-critical region, which is much lower than the temperature scale of charge coherence T_{ch}. The filling dependence of T_0 is calculated and the maximal T_0 reaches one tenth of the hopping integral. The Fermi distribution functions in momentum space are calculated in the strongly correlated paramagnetic phase. The fermion occupation numbers are strongly suppressed from the saturated value even for wavevectors close to the center of the Brillouin zone. When entering the critical region, for the SU(2) symmetric models, $\chi(T)$ grows exponentially. The true FM long range order is achieved by reducing the model symmetry to the Ising class and the FM critical temperature T_c is determined accurately by the finite size and critical scaling.

2.2 The Model Hamiltonian and the absence of the sign problem

In this section, we present the model Hamiltonians, whose ground states were proved to be ferromagnetic [37]. Furthermore, we also explain that the QMC sign-problem is absent, and thus, this model provides an ideal preliminary to study the thermodynamic properties and magnetic phase transitions of strongly-correlated itinerant

FM in a controllable way.

2.2.1 The model Hamiltonians

We consider the case of the 2D square lattice: On each site there are two orthogonal orbitals forming a quasi-1D band structure. For simplicity, below we use the 2D p-orbital system as an example, and the physics is also valid for the d_{xz} and d_{yz}-orbitals systems in 2D. The relevance of this model to the current experiment efforts of searching for novel itinerant FM systems will be discussed in Sect. 2.7. For the band structure, we only keep the σ-bonding $t_{\parallel}$ term, i.e., electrons in the $p_{x(y)}$-orbital only move longitudinally along the $x(y)$-direction, respectively. The following Hamiltonian is defined in the square lattice as

$$\begin{aligned} H_{kin,\parallel} &= -t_{\parallel}\sum_{\vec{r},\sigma}\Big\{p^{\dagger}_{x\sigma}(\vec{r}+\hat{e}_x)p_{x\sigma}(\vec{r})+p^{\dagger}_{y\sigma}(\vec{r}+\hat{e}_y) \\ &\times \quad p_{y\sigma}(\vec{r})+h.c.\Big\}-\mu\sum_{\vec{r}}n(\vec{r}), \end{aligned} \tag{2.2}$$

in which we neglect the small transverse bonding $t_{\perp}$-term. For realistic p-orbital systems, the sign of $t_{\parallel}$ is negative due to the odd parity of p-orbital Wannier wavefunctions. Nevertheless, for the bipartite lattice such as the square lattice, the sign of $t_{\parallel}$ can be flipped by a gauge transformation. Without loss of generality, $t_{\parallel}$ is scaled to 1 below, which serves as the unit for all other quantities carrying energy unit in this article.

The interaction part H_{int} contains the standard multi-orbital Hubbard interaction

[72, 73, 74, 75] as

$$\begin{aligned} H_{int} &= U\sum_{\vec{r},a=x,y} n_{a,\uparrow}(\vec{r})n_{a,\downarrow}(\vec{r}) + V\sum_{\vec{r}} n_x(\vec{r})n_y(\vec{r}) \\ &- J\sum_{\vec{r}}\left\{\vec{S}_x(\vec{r})\cdot\vec{S}_y(\vec{r}) - \frac{1}{4}n_x(\vec{r})n_y(\vec{r})\right\} \\ &+ \Delta\sum_{\vec{r}}\left\{p^{\dagger}_{x\uparrow}(\vec{r})p^{\dagger}_{x\downarrow}(\vec{r})p_{y\downarrow}(\vec{r})p_{y\uparrow}(\vec{r}) + h.c.\right\}, \end{aligned} \tag{2.3}$$

where $a = x, y$ referring to the orbital index; $n_{a,\sigma} = p^{\dagger}_{a,\sigma}p_{a,\sigma}$ and $n_a = n_{a,\uparrow} + n_{a,\downarrow}$; $\vec{S}_a = p^{\dagger}_{a,\alpha}\vec{\sigma}_{\alpha\beta}p_{a,\beta}$ is the spin operator of the a-orbital. The U and V-terms describe the intra- and inter-orbital Hubbard interactions, respectively; the J-term is Hund's coupling and $J > 0$ represents its FM nature; the Δ-term describes the pairing hopping process between two orthogonal orbitals.

In order to gain an intuitive understanding of the interaction parameters, let us consider a single site problem. There are in total six states which can be classified as a set of spin triplet states and three different spin singlet states. The triplet states are with energy V, defined as

$$p^{\dagger}_{x,\uparrow}p^{\dagger}_{y,\uparrow}|0\rangle,\ \ \frac{1}{\sqrt{2}}(p^{\dagger}_{x,\uparrow}p^{\dagger}_{y,\downarrow} + p^{\dagger}_{x,\downarrow}p^{\dagger}_{y,\uparrow})|0\rangle,\ \ p^{\dagger}_{x,\downarrow}p^{\dagger}_{y,\downarrow}|0\rangle, \tag{2.4}$$

respectively, where $|0\rangle$ is the vacuum state. The other three spin singlet states are

$$\frac{1}{\sqrt{2}}(p^{\dagger}_{x,\uparrow}p^{\dagger}_{y,\downarrow} - p^{\dagger}_{x,\downarrow}p^{\dagger}_{y,\uparrow})|0\rangle,\ \ p^{\dagger}_{x,\uparrow}p^{\dagger}_{x,\downarrow}|0\rangle,\ \ p^{\dagger}_{y,\uparrow}p^{\dagger}_{y,\downarrow}|0\rangle, \tag{2.5}$$

among which the first one involves both orbitals and its energy is $V + J$; the other two singlets only occupy the same orbital with the average energy U and the hybridization matrix element between them is Δ. In the limit of $U \to +\infty$, the states of $p^{\dagger}_{x,\uparrow}p^{\dagger}_{x,\downarrow}|0\rangle$, and $p^{\dagger}_{y,\uparrow}p^{\dagger}_{y,\downarrow}|0\rangle$ are projected out. Nevertheless, the other four doubly occupied states are kept

in the physical Fock space, including one set of spin-triplet states and one inter-orbital singlet state.

The ground states of the Hamiltonians Eq. 2.2 plus Eq. 2.3 are fully spin polarized at any generic filling n for arbitrary values of V under the condition that $U \to +\infty$ and $J > 0$. The detailed proof and its generalization to the 3D cubic lattice are presented in Ref. [[37]]. Below we present an intuitive physical picture. The band structure of Eq. 2.2 is quasi-1D, consisting of orthogonal rows and columns, and electrons do not transit among different lines. In the absence of Hund's coupling, then the intra-chain physics in the limit of $U \to +\infty$ would correspond to the 1D infinite-U Hubbard model whose ground states are highly degenerate regardless of the spin configurations. Then let us turn on $J > 0$, and the inter-chain Hund's coupling lifts the degeneracy and selects the fully polarized state as the unique ground state: When one electron in a row meets another one in a column at the crossing site, their spins are aligned to save the energy of J. Thus different from the usual case that Hund's coupling can only polarize electrons on the same site. Remarkably, in this case it does polarize electrons in the entire system [37, 36]. Although the electron band structure is quasi-1D, interactions couple electron spins in different chains together, and thus, the FM correlations and ordering are genuinely 2D, or, 3D.

For completeness, we also present the Hamiltonian of the inter-chain hopping with a small value of $t_\perp$ as

$$\begin{aligned} H_{kin,\perp} &= -t_\perp \sum_{\vec{r},\sigma} \Big\{ p^\dagger_{x\sigma}(\vec{r}+\hat{e}_y) p_{x\sigma}(\vec{r}) \\ &+ p^\dagger_{y\sigma}(\vec{r}+\hat{e}_x) p_{y\sigma}(\vec{r}) + h.c. \Big\}, \end{aligned} \tag{2.6}$$

which will be used in Sect. 2.7.1. Again, in the square lattice the sign of $t_\perp$ can be flipped by a gauge transformation, and without loss of generality, it is assumed to be positive.

We set $t_\perp = 0$ in most part of this article except in Sect. 2.7.1.

2.2.2 The absence of the QMC sign problem

The many-body Hamiltonian matrix of Eq. 2.2 plus Eq. 2.3 possesses an important sign structure in the limit of $U \to +\infty$ under which the ground state FM theorem applies [37]. In the coordinate representation, a convenient set of many-body bases are defined by ordering fermions according to their real space positions along one row by another and then along one column by another. The periodical and anti-periodical boundary conditions are employed for each chain if the particle number in that chain is odd and even, respectively, which is feasible because the particle number in each chain is separately conserved. This particular choice of boundary conditions should not change the bulk physics. Under these bases and boundary conditions, in the limit of $U \to +\infty$, the electron hopping term and the spin-flip term from Hund's coupling do not change the sequence of fermion ordering. When electrons hop across the boundary, no extra minus sign appears either due to the above boundary condition. Then the many-body Hamiltonian matrix satisfies the prerequisite of the Perron-Frobenius theorem: All the non-zero off-diagonal matrix elements are either $-t$ or $-J$ arising from the kinetic energy term and Hund's coupling, respectively, and thus they are semi-negative-definite. We do not need to consider the pair hopping process which is completely suppressed in the limit of $U \to +\infty$. Remarkably, the above sign structure of the off-diagonal matrix elements renders the ground state many-body wavefunction nodeless, and also leads to the disappearance of the QMC sign problem for the ground states.

For the finite temperature thermodynamic properties, we use the stochastic series expansion (SSE) QMC method with the directed loop update algorithm [76, 77, 78, 79, 80]. This method is usually used for boson systems and 1D fermion systems. In our case, although the band structure of Eq. 2.2 is quasi-1D like, the interaction Eq. 2.3 couples all

the chains together. In particular, the total spin of each chain is not conserved, and thus its magnetic properties in truly 2D. Remarkably, we find for this model the sign problem is absent at finite temperatures in the entire electron density region $0 < n < 2$. In the SSE method, the partition function is expanded as

$$Z = \sum_{n=0}^{+\infty} \frac{\beta^n}{n!} \sum_{\alpha_i^n} \prod_{i=1}^{n} \langle \alpha_i^n | - H | \alpha_{i-1}^n \rangle , \tag{2.7}$$

where $H = H_{kin,\parallel} + H_{int}$; $|\alpha_i^n\rangle$ runs over the set of many-body bases defined above and $|\alpha_n^n\rangle = |\alpha_0^n\rangle$. A negative constant is added to the many-body Hamiltonian matrix to make all of its diagonal matrix elements negative, and then all the matrix elements of $-H$ become positive. The grand canonical ensemble is employed to ensure the ergodicity of the particle number distribution in each chain. We have carefully adjusted the chemical potential μ according to the temperature to maintain the targeted filling factor.

The QMC sign problem does appear in the presence of the $t_\perp$-term , i.e., Eq. 2.6, because electrons become mobile in a two-dimensional manner. Nevertheless, the QMC simulations can still be performed when the sign problem is not so severe, which will be presented in Sect. 2.7.1.

2.3 Thermodynamic quantities in the off-critical region

In this section, we present the results of QMC simulations on the spin magnetic susceptibility $\chi(T)$ and the compressibility $\kappa(T)$ in the off-critical temperature region. $\chi(T)$ exhibits the celebrated CW law at temperatures well-below the kinetic energy scale of the system, while $\kappa(T)$ typically weakly depends on temperature.

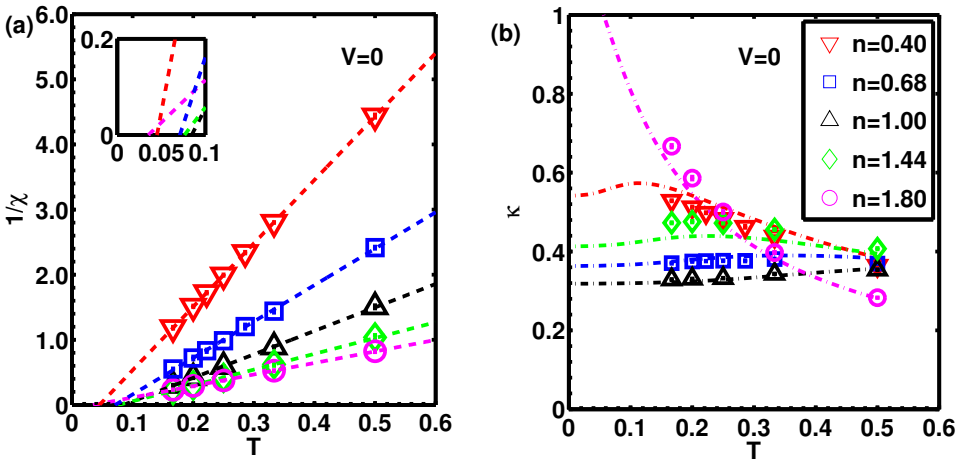

Figure 2.1: The temperature dependence of the spin-susceptibility and the compressibility for various fillings at $V = 0$. (a) $\chi^{-1}(T)$ exhibits the CW law at different values of n. The inset shows interceptions corresponding to the mean-field value of Curie temperature T_0. (b) The compressibility $\kappa(T)$ at different values of n. The dashed lines represent $\kappa(T)$ of 1D spinless fermions at the same densities for comparison. Values of n in (a) and (b) are represented by the same legend. $V = 0$ and $J = 2$ for both figures. The error bars of the QMC data are smaller than the symbols.

2.3.1 The temperature dependence of spin susceptibility $\chi(T)$ and compressibility $\kappa(T)$

The spin susceptibility χ and compressibility κ are two fundamental thermodynamic properties in interacting fermion systems in the spin and charge channels, respectively. In usual paramagnetic Fermi liquid states, both χ and κ at zero temperature exhibit the itinerant feature controlled by the density of states at the Fermi energy. Furthermore, they are renormalized by interaction effects characterized by the Landau parameters F_a^0 and F_s^0 in the spin and charge channels, respectively. At finite temperatures much lower than the Fermi temperature, $\chi(T)$ and $\kappa(T)$ are only weakly temperature dependent. However, in FM metals $\chi(T)$ and $\kappa(T)$ behave dramatically differently exhibiting local-moment-like and itinerant features, respectively, which will be shown from the QMC simulation results.

Because the total spin is conserved, the spin magnetic susceptibility χ is represented by the equal-time correlation function as

$$\chi(T) = \lim_{L\to+\infty} \frac{\beta}{L^2} \sum_{\vec{r}_1,\vec{r}_2} \langle S_z(\vec{r}_1) S_z(\vec{r}_2)\rangle. \tag{2.8}$$

The QMC results of $\chi^{-1}(T)$ at $V = 0$ are presented in Fig. 2.1 (a) in the off-critical region based on the finite size scalings. For all the values of n presented, χ exhibits the CW-law in the off-critical region. The values of T_0 extracted from the linear form $\chi^{-1}(T)$ range from 0.01 to 0.1, which means that spin remains incoherent at temperatures well below $t_{\|}$ (scaled to 1).

It is not surprising that $\chi(T)$ should asymptotically scale as $1/T$ in the high temperature limit $T \gg T_f$ where T_f is the Fermi temperature because in this limit spin channel is completely incoherent. Nevertheless, the spin incoherence persists into a much lower temperature scale T_0 below T_f. Although T_0 is a mean-field energy scale which does not mean the FM long-range order, it remains important roughly equal to the energy cost of flipping an individual electron spin in the ground state. Due to non-Gaussian fluctuations, the actual FM critical temperature T_c significantly deviates from T_0 defined in Eq. 2.1. In the current SU(2) invariant case, actually $T_c = 0$ due to the Mermin-Wagner theorem [71].

The compressibility $\kappa(T)$ reflects the coherence in the charge channel. Because the total particle number is a conserved quantity, it is also defined as an equal-time correlation function as

$$\kappa(T) = \lim_{L\to+\infty} \frac{\beta}{L^2} \sum_{\vec{r}_1,\vec{r}_2} \langle n(\vec{r}_1) n(\vec{r}_2)\rangle. \tag{2.9}$$

The QMC results of $\kappa(T)$ at $V = 0$ are presented in Fig. 2.1 (b). Again κ is proportional

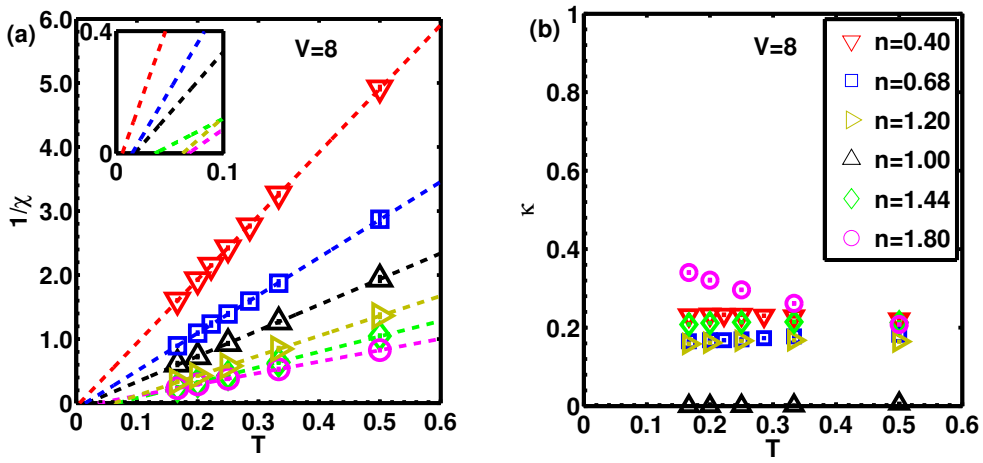

Figure 2.2: The temperature dependence of the spin-susceptibility and the compressibility for various fillings at $V = 8$. (a) $\chi^{-1}(T)$ and (b) $\kappa(T)$ at a large value of $V = 8$ in the temperature regime of $1/6 < T < 1/2$. Different values of n are shown in the legend in (b). At $n = 1$, the system is in the Mott-insulating state, and thus $\kappa(T)$ drops to nearly zero at low temperatures. The error bars of the QMC data are smaller than the symbols.

to $1/T$ in the high temperature incoherent regime as shown in Eq. 2.9, and it saturates at low temperatures in the metallic phase. The crossover temperature scale T_{ch} between these two regimes is typically the chemical potential at zero temperature. In the usual Fermi liquid state, κ is typically the density of state at the Fermi energy renormalized by Landau parameters. In our case, the situation is different due to the prominent FM fluctuations. At $V = 0$, due to the infinite U and the 1D band structure, T_{ch} is roughly the Fermi temperature of spinless fermions at the same density. For most values of n presented in Fig. 2.1 (b), T_{ch} is at the order of $t_{\|}$, and thus κ saturates in the temperature region presented. As for the case of a low hole density $n = 1.8$, T_{ch} can be estimated around 0.1, and thus $\kappa(T)$ does not saturate yet in the simulated temperature region. Because of the strong FM tendency, the inter-orbital interaction vanishes at $V = 0$ and $\kappa(T)$ can be well fitted by that of spinless fermions as shown in Fig. 2.1 (b).

Comparing $\chi(T)$ and $\kappa(T)$, the spin coherence temperature T_0 is much lower than the charge coherence temperature T_{ch}. These two distinct coherence temperature scales in

spin and charge channels are an important feature of FM metals. A common phenomenological interpretation is to divide electrons into two parts: local moments and itinerant electrons which are responsible for the spin and charge channel behaviors, respectively. However, this dividing is artificial for metals when all the electrons are itinerant with equivalent band structures such as in our case. Based on the QMC simulations above, we have shown unambiguously that the CW-law can indeed appear in strongly correlated systems without local moment formation. A similar feature also appears in the CW metal states [81, 82] and the 1D spin incoherent Luttinger liquids [83]. The difference is the behavior of χ below the spin coherence temperature T_0. In the case of the CW-metal, χ saturates exhibiting the Pauli-like behavior but strongly enhanced by interactions, and in the 1D case, antiferromagnetic correlations develops. In our case, as will be shown in Fig. 2.6 in Sect. 2.5, χ evolves into an exponential growth as a reminiscence of the FM long-range ordered ground state [37].

Next we consider the effects of a large inter-orbital repulsion V to $\chi^{-1}(T)$ and $\kappa(T)$. The ground states remain fully spin polarized as proved in Ref. [[37]], and the QMC results of $\chi^{-1}(T)$ still exhibit the CW law at all the fillings as shown in Fig. 2.2 (*a*). The most prominent effect of V is the suppression of $\kappa(T)$ at the commensurate filling of $n = 1$ as shown in Fig. 2.2 (*b*), in which the system is in the Mott-insulating state. In this case, electrons become local moments due to the opening of charge gap. As a result, $\kappa(T)$ is suppressed to nearly zero at $0 < T < 0.5$, which is still small compared to the charge gap at the order of V. In the Mott-insulating ground state at $n = 1$, the orbital channel can develop the antiferro-orbital ordering with a staggered occupation of p_x and p_y-orbitals. The QMC simulation results on the antiferro-orbital ordering transition are presented in the section 2.6. As n moves away from 1, electrons become itinerant again. Nevertheless, the values of $\kappa(T)$ at $V = 8$ are significantly suppressed compared to those with the same values of n and T at $V = 0$.

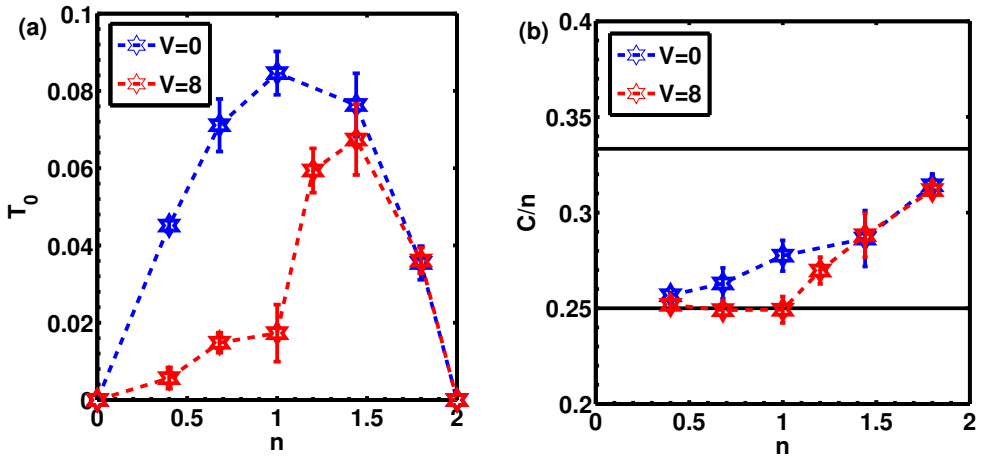

Figure 2.3: The density-dependence of the Curie temperature and the Curie constant. (*a*) The density-dependence of the Curie temperature $T_0(n)$ at $V = 0$ and 8 with $J = 2$, respectively. (*b*) The density-dependence of the reduced Curie constant: C/n *v.s.* n. The lower and upper bold lines represent the limits of the spin-$\frac{1}{2}$ and spin-1 moments, respectively. Plots are based on the results of $\chi(T)$ in Fig. 2.1 (*a*) and Fig. 2.2 (*a*).

2.3.2 The density dependences of $T_0(n)$ and the Curie constant $C(n)$

The ground state FM survives in all the filling region $0 < n < 2$, nevertheless, its robustness against thermal fluctuations varies at different densities, which reflects through the density dependences of $T_0(n)$ and $C(n)$.

The relation $T_0(n)$ is presented in Fig. 2.3 (*a*) for both cases of $V = 0$ and $V = 8$. The FM coherence is built up due to the itinerancy of fermions [37], thus T_0 approaches zero in both limits of $n \to 0$ (the particle vacuum) and $n \to 2$ (the hole vacuum). At $V = 0$, the maximal T_0 appears around $n = 1$ where electrons are most mobile. $T_0(n)$ at $V = 0$ is nearly symmetric with respect to $n = 1$ exhibiting an approximate particle-hole symmetry. In contrast, it is highly asymmetric at large V. In this case, T_0 is strongly suppressed at $0 < n < 1$, in which both charge and spin carriers are electrons. A large V penalizes two electrons occupying the same site, thus the effectiveness of Hund's rule is suppressed. After n passes 1, a quick increase of T_0 appears because extra electrons on top of the Mott background of $n = 1$ can move easily to build up the FM coherence.

T_0 reaches the maximum roughly at the middle point between $n = 1$ and 2. As $n \to 2$, T_0 becomes insensitive to V. In this region, most sites are doubly occupied in the states of spin-1 moments, and holes are itinerant but do not carry spin. Hole's motion threads spin moments along its trajectory and aligns their orientations, and this process is not much affected by V. At $V = 8t_{\|}$ and $J = 2t_{\|}$, the maximal $T_0 \approx 0.06t_{\|}$ which appears around $n \approx 1.4$. In other words, at large values of V, there is an approximate particle-hole symmetry between $n = 1$ to 2 on the background of one electron per site.

Next we present the results of the Curie constant C. Assuming the local moment picture, the simple molecule field method yields C per spin moment as $\frac{1}{3}S(S+1)$ [26], where S is the spin magnitude. In our case mostly itinerant, the magnitudes of S fluctuate: $C = 0$ for the empty site, $\frac{1}{4}$ for the singly occupied site, and $\frac{2}{3}$ for the doubly occupied site in the spin-1 configuration, respectively. We plot the normalized Curie constant C/n *v.s.* n in Fig. 2.3 (*b*). C/n approaches $\frac{1}{4}$ as $n \to 0$, and $\frac{1}{3}$ as $n \to 2$ where most sites are spin-1 moments. Generally, C/n lies between these two limits. At $V = 0$, as n increases, the number of onsite triplets smoothly increases and so does C/n. Nevertheless, at large V, the onsite triplet formation is strongly suppressed at $0 < n < 1$, and thus C/n is stuck at $\frac{1}{4}$. After n passes 1, C/n starts to increase nearly linearly toward 1/3. As $n \to 2$, V hardly affects the number of onsite triplets, and thus C/n also becomes insensitive to V as T_0 does.

2.3.3 The onsite charge fluctuations and spin moments

To further clarify the nature of our system whether it is itinerant or local-moment-like, we calculate the onsite charge fluctuations and the average spin moments below. The onsite charge fluctuations are defined as

$$\delta = \langle n_i^2 \rangle - n^2, \tag{2.10}$$

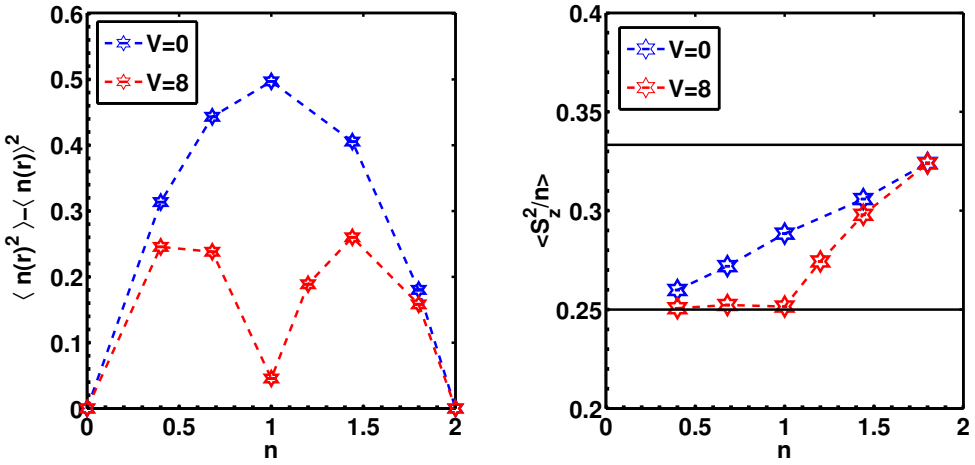

Figure 2.4: (a) The onsite particle number fluctuation δ defined in Eq. 2.10. (b) The QMC results for the normalized onsite spin moment $\langle S_z^2\rangle/n$. The parameters $\beta = 6$, $J = 2$ and $L = 30$.

where n_i is the total particle number on site i. Due to the translation symmetry, δ is independent of the site index i, and the simulation results are plotted in Fig. 2.4. At $V = 0$, the charge fluctuations are significant in the entire filling region except very close to the particle vacuum at $n = 0$ and the hole vacuum at $n = 2$. The maximum is reached at the approximate particle-hole symmetric point of $n = 1$. The large onsite charge fluctuations clearly reflect the itinerant nature of the system, which is consistent with the compressibility results in Fig. 2.1 (b). When the inter-orbital repulsion V goes large, charge fluctuations are greatly suppressed near the commensurate filling $n = 1$. In this case, the system becomes local-moment-like, which agrees with the vanishing compressibility shown in Fig. 2.2 (b). Nevertheless, as moving away from $n = 1$, the system becomes itinerant again exhibiting significant onsite charge fluctuations.

We also calculate the square of the z-component of the onsite spin moment $\langle S_{i,z}^2\rangle$ which equals $\frac{1}{3}\langle \vec{S}_i^2\rangle$ since the SU(2) symmetry is not broken. In order to compare with the Curie constant C/n, we plot its values normalized by the filling, i.e. $\langle S_{i,z}^2\rangle/n$ as presented in Fig. 2.4(b), which is nearly the same as the Curie constant C/n plotted in Fig. 2.3

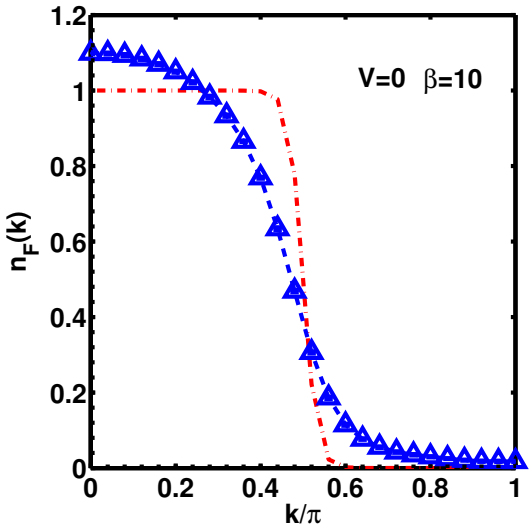

Figure 2.5: The momentum space distribution $n_F(k)$ ($0 \leq k \leq \pi$) at $\beta = 10$ and $n = 1$, and $n_F(k)$ of the non-interacting spinless fermion (the red dashed line) is plotted for comparison. The system size $L = 50$. The parameter values are $V = 0$ and $J = 2$. The error bars of the QMC data are smaller than the symbol.

(b). At $V = 0$, $\langle \vec{S}_i^2 \rangle$ varies smoothly with n: the probable onsite configurations include empty, singly occupied (spin-$\frac{1}{2}$), and doubly occupied (spin-1) states. At $V = 8$ and the commensurate filling $n = 1$, $\langle \vec{S}_i^2 \rangle \approx \frac{3}{4}$, which manifests the formation of the local moment of spin-$\frac{1}{2}$ in consistent with the suppressed charge fluctuations. At $0 < n < 1$, each site is nearly either empty or singly occupied, and thus $\langle \vec{S}_i^2 \rangle \approx \frac{3}{4}n$. At $1 < n < 2$, the probable onsite configurations include the singly occupied spin-$\frac{1}{2}$ moment and doubly occupied spin-1 moment. Thus the system remains itinerant even in at large V when moving away from $n = 1$.

2.4 The momentum space fermion occupation

An important feature of the itinerant FM is the fluctuating FM domains in real space in the paramagnetic phase close to T_0. This prominent FM fluctuations also strongly affect the momentum space fermion occupation as shown below. Basically, the fermion

occupation functions still resemble those in the fully polarized systems with thermal broadening.

Because the particle number of each chain is separately conserved, the momentum space distribution function is essentially 1D-like. Nevertheless, each chain is not isolated but interacts with others through multi-orbital interactions, and thus spin is not conserved separately in each chain. Without loss of generality, we define $n_F(k) = \sum_\sigma \langle p_{x,\sigma}(k) p_{x,\sigma}(k) \rangle$ for a horizontal x-chain. The case of $n = 1$ is studied below as a representative, which is equivalent to $n_x = 0.5$ in this x-chain. Its mean-field Curie temperature $T_0 \approx 0.08$ as shown in Fig. 2.3 (a) before. The simulated results of $n_F(k)$ are presented in Fig. 2.5 with the periodical boundary condition.

We define a reference wavevector as the Fermi wavevector $k_f^0 = \frac{\pi}{2}$ of spinless fermions at the same density. At a low temperature $T = 1/\beta = 0.1$ close to T_0, as shown in Fig. 2.5, $n_F(k)$ is only slightly larger than 1 even at $k \ll k_f^0$. It smoothly decays to zero with a half-width approximately equal to k_f^0. $n_F(k)$ is rounded off compared to that of spinless fermions at the same temperature. Although $n_F(k)$ does not look much different from that of spinless fermions, it is a consequence of strong interactions because the system is in the paramagnetic state! The system remains unpolarized with a finite FM correlation length ξ.

The above result implies that the phase space for thermal fluctuations is not restricted to a small region close to $\pm k_f^0$, but extends over the entire Brillouin zone because of the spin fluctuation. This is the reason that usual approaches, such as random phase approximation, that only deal with the degrees of freedom in the vicinity of the Fermi surface fail. In addition, such form of momentum distribution indicates that the entropy capacity is higher than that expected from Fermi liquid. This is a good sign for implementing this system in ultracold atom experiments.

and thus its entropy capacity is enhanced. It is consistent with the real space

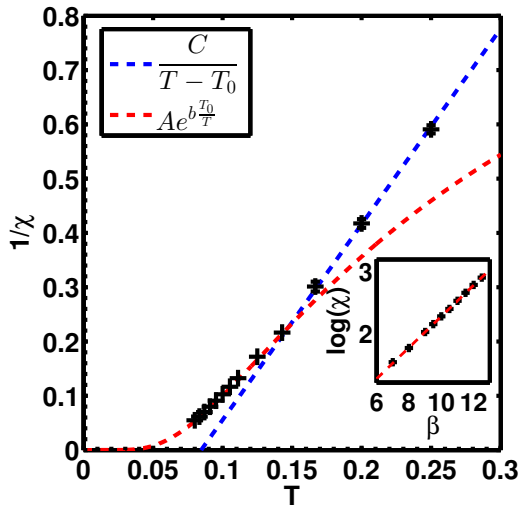

Figure 2.6: The SU(2) invariant model in the critical region: $\chi^{-1}(T)$ at $n = 1$, $J = 2$ and $V = 0$. It crosses over from the CW law to the exponential form of $\chi(T) = Ae^{b\frac{T_0}{T}}$. The inset shows the linear scaling of $\ln\chi(T)$ v.s. β.

picture of fluctuating FM domains as T approaches T_0. This is highly non-perturbative showing the power of the QMC simulations.

2.5 The low temperature critical region

So far we have discussed the FM properties in the off-critical region. In this section we will further study the magnetic critical behavior through QMC. The FM order parameter is a conserved quantity, and thus there are no quantum fluctuations, however, in 2D thermal fluctuations are so strong that long-range FM ordering cannot appear at any finite temperatures for SU(2) symmetric models [71, 84]. Nevertheless, magnetic properties still behave qualitatively differently in the off-critical and critical regions. We will also consider the model in the Ising class in which true FM long range ordering can appear, and determine the renormalized Curie temperature T_c.

In spite of the quasi-1D band structure, the magnetic properties of our model are

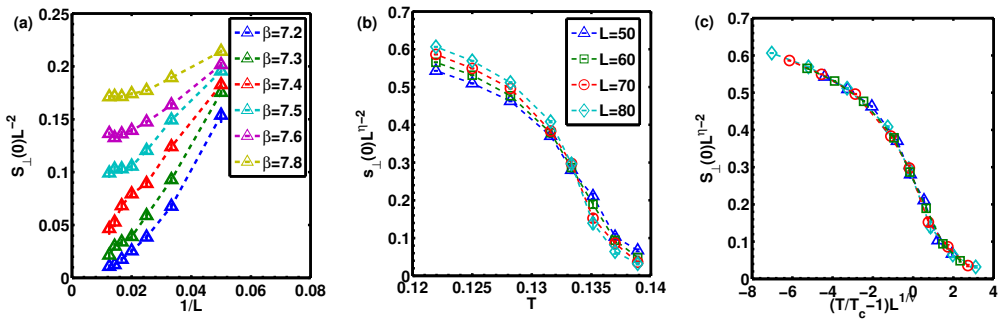

Figure 2.7: The FM long-range ordering of the Ising symmetric model with parameters $J_\perp = 2J_\parallel = 4$, $n = 1$, and $V = 0$. (a) The finite size scaling of $S_\perp/L^2$. The FM critical temperature is extracted as $T_c = 1/\beta_c = 0.134 \pm 0.002$ with $\beta_c \approx 7.4 \sim 7.5$. ($b$) The critical scaling: $S_\perp L^{-2+\eta}$ v.s. T with $\eta = \frac{1}{4}$. The crossing of curves at different values of L yields $T_c \approx 0.134$. (c) The data collapse of the scaling form $S_\perp(0)L^{-2+\eta} = f((T-T_c)L^{1/\nu})$ fitted by the parameters of $\nu = 1$, $\eta = \frac{1}{4}$ and $T_c = 0.1337$.

intrinsically 2D because Hund's interaction couples spins of different chains together and the total spin of each chain is not separately conserved. In Fig. 2.6, we present the crossover of $\chi^{-1}(T)$ from the off-critical region to the critical region based on the finite size scaling. Although there is no distinct phase transition between the off-critical and critical regions, the temperature dependence of $\chi(T)$ changes qualitatively. The clear deviation from the CW law starts from $T \sim T_0 = 0.08$. In the critical region, the FM order parameter already develops a non-zero magnitude, and its directional fluctuations are described by the O(3) non-linear σ-model. The FM correlation length increases exponentially as approaching zero temperature. $\chi(T)$ evolves to the exponential form fitted by $\chi = Ae^{b\frac{T_0}{T}}$ [85, 86], and the result in Fig. 2.6 shows $b = 3.1 \pm 0.3$ at $n = 1$, $V = 0$, and $J = 2$.

In order to obtain the FM long-range order, we modify Hund's coupling of Eq. 2.3 to reduce its symmetry from the SU(2) to the Ising class: We introduce $J_\parallel$ and $J_\perp$ for the spin components in the xy-plane and along the z-direction, respectively, and choose $J_\perp > J_\parallel$. The z-component FM structure factor is defined as $S_\perp(T,L) = T\chi(T,L)$. For the case presented in Fig. 2.7 (a), the finite size scaling of $S_\perp(T,L)/L^2$ yields the critical

temperature $T_c \approx 0.134$. This result is also checked from the scaling in the critical region in Fig. 2.7 (b) and (c). $S_\perp L^{-2+\eta}$ *v.s.* T is plotted with $\eta = \frac{1}{4}$ from the anomalous dimension of the 2D Ising universal class. The crossings of curves yield the value of T_c consistent with that of the previous scaling. Furthermore, a good data collapse is achieved by employing the scaling form

$$S_\perp L^{-2+\eta} = f((T - T_c)L^{\frac{1}{\nu}}) \tag{2.11}$$

with $\nu = 1$ of the 2D Ising class.

The mean-field value $T_0 \approx 0.20$ is extracted based on the extrapolation of the CW behavior of the spin susceptibility. Compared to the mean-field value T_0, T_c is about 67% of T_0 as a result of the critical non-Gaussian fluctuations. For the 2D Ising mode with only nearest neighbor coupling on the square lattice, the Onsager solution gives rise to $T_c = 2/\ln(\sqrt{2}+1) \approx 2.269$ which is 57% of the Bragg-Williams mean-field results $T_0 = 4$. Thus the critical fluctuation strength of the case presented in Fig. 2.7 is weaker compared to that in the 2D Ising model in spite of the effect of the transverse component $J_\parallel$. This is due to the itinerant nature of our model such that the effective FM coupling is beyond two nearest neighboring sites.

2.6 The orbital ordering at the commensurate filling $n = 1$

Here we present the QMC simulations on the orbital ordering with a large value of the inter-orbital repulsion V. Large V suppresses doubly occupied on-site states, and at the commensurate filling $n = 1$, the ground state is in the Mott-insulating state. In this case, fermions become local moments. At zero temperature, even though electron spins

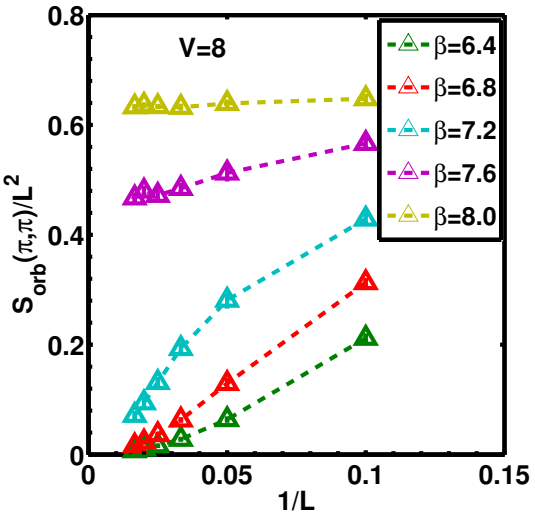

Figure 2.8: The finite size scaling of $S_{orb}(\pi,\pi)/L^2$ with the parameter values $J_\perp = J_\parallel = 2$, $n = 1$ and $V = 8$. The system sizes range from $L = 10$ to 60 and the values of inverse temperature β are presented in the legend. The orbital ordering occurs at β between 7.2 to 7.6, which corresponds to $T_{orb}/t_\parallel \approx 0.132 \sim 0.139$.

are fully polarized, the orbital degree of freedom enables the superexchange in the orbital channel [13]. The orbital exchange is described by an antiferro-orbital Ising model

$$H_{ex} = J_{orb} \sum_{\vec{r},\vec{r}'} \tau_z(\vec{r})\tau_z(\vec{r}'), \tag{2.12}$$

where $J_{orb} = t_\parallel^2/V$ and $\tau_z = p_x^\dagger p_x - p_y^\dagger p_y$. At low temperatures, due to the prominent FM tendency, the above orbital exchange model still applies, thus below the temperature scale around J_{orb}, the antiferro-orbital ordering, i.e., the staggered occupation of p_x and p_y-orbitals, will appear.

We define the equal-time orbital structure factor as:

$$S_{orb}(\vec{q},\tau) = \frac{1}{L^2} \sum_{\vec{r}_1,\vec{r}_2} \langle m_{orb}(\vec{r}_1,\tau) m_{orb}(\vec{r}_2,\tau)\rangle e^{i\vec{q}\cdot(\vec{r}_2-\vec{r}_1)}, \tag{2.13}$$

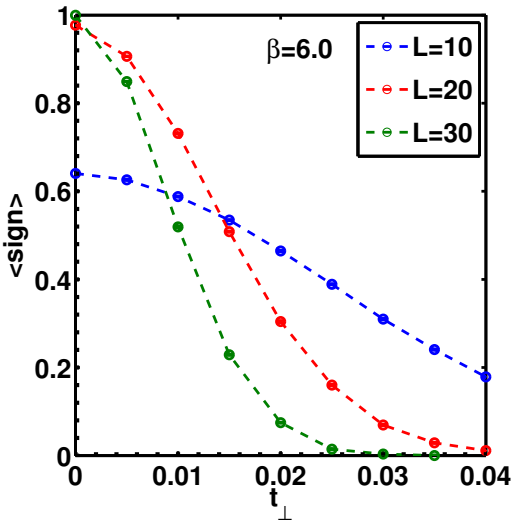

Figure 2.9: The average of the fermion sign v.s. $t_\perp$ at different values of L. The parameters are $V = 0$, $J = 2$, $n = 1$, and $\beta = 6$.

where $m_{orb}(\vec{r},\tau) = n_x(\vec{r},\tau) - n_y(\vec{r},\tau)$ is the on-site orbital polarization. Since the orbital ordering occurs at the wavevector (π,π), we present the QMC simulation of the finite scaling of $S_{orb}(\pi,\pi)/L^2$ in Fig. 2.8. It indicates that the antiferro-orbital ordering appears at low temperatures, and the critical temperature $T_{orb}/t_{\|}$ lies between 0.132 and 0.139.

2.7 Discussions on the $t_\perp$-term and the finite U

In this section, we discuss the situations when the conditions for the absence of sign problem are loosed, including the presence of a small transverse hopping $t_\perp$-term as shown in Eq. 2.6, and the case of finite values of U.

2.7.1 QMC simulations with small transverse hopping term

The presence of the $t_\perp$-term enables electrons moving in the entire two-dimensional lattice, thus the fermion sign problem does appear. Nevertheless, the sign problem is not severe at small values of $t_\perp$, such that QMC simulations can still be performed. In

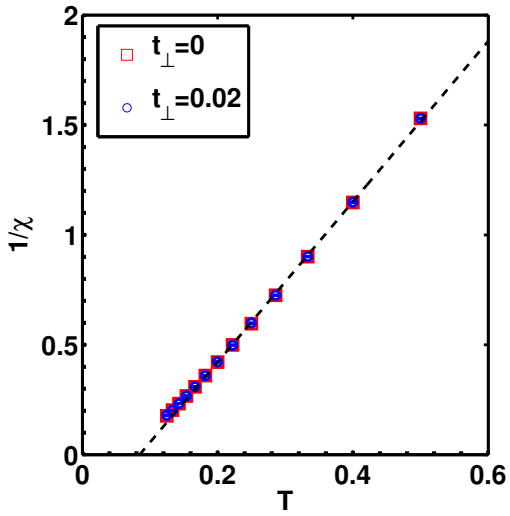

Figure 2.10: $\chi^{-1}(T)$ at $t_\perp = 0$ and 0.02, respectively, with the system size $L = 20$. Periodical boundary conditions are used. The parameters are $V = 0$, $J = 2$, $n = 1$.

Fig. 2.9, the average of sign is calculated from $t_\perp = 0$ to 0.05 at small and intermediate sample sizes with $\beta = 6$. We use the periodical boundary condition for the entire system, which is different from the boundary condition used in previous calculations in order to eliminate the sign problem when electrons hop across the boundary. The previous boundary condition is feasible at $t_\perp = 0$ because particle number in each chain is conserved as explained in Sect. 2.2.2. Now under the periodical boundary condition, even at $t_\perp = 0$ the sign is not positive definite: when one electron hops across the boundary, if the fermion number in that chain is an even number, the matrix element acquires an extra sign. This boundary effect is more prominent at small sample sizes (e.g. $L = 10$) but already becomes negligible at intermediate sample sizes, say, $L > 20$. As $t_\perp$ deviates from 0, the 2D motion of electrons suppresses the average sign and it drops more rapidly at larger sample sizes.

We have simulated the spin susceptibility and presented its inverse $\chi^{-1}(T)$ in Fig. 2.10 with $t_\perp = 0.02$. The results at $t_\perp = 0$ under the periodical boundary condition are also plotted for a comparison. An intermediate sample size ($L = 20$) is used and

the simulation is performed from the high to intermediate temperature regions. The results at $t_\perp = 0.02$ are nearly the same as those at $t_\perp = 0$, which still exhibit the CW behavior. At the lowest temperature simulated $\beta = 6$, the average sign at $t_\perp = 0.02$ is already significantly below 1. Nevertheless, the difference between $\chi^{-1}(T)$'s at $t_\perp = 0$ and 0.02 remains negligible. These results show that the magnetic properties are not so sensitive to $t_\perp$ when $t_\perp/t_\parallel \ll 1$.

Certainly, when $t_\perp$ reaches the same order as $t_\parallel$, the band structure will become genuinely two-dimensional. In this case, the previous ground FM theorem does not apply, and a quantum phase transition is likely to occur from the FM to paramagnetic ground states. Unfortunately, the sign problem will be very severe and thus reliable QMC simulations cannot be performed. It would be interesting to further develop other analytic and numeric methods to investigate this problem.

2.7.2 The effect of the finite U

As explained in Sect. 2.2.2, the many-body bases for simulations, which are also used for the proof of FM ground state theorems in Ref. [37], are constructed by ordering electrons according to their locations along one chain by another regardless of their spin configurations. This set of bases are convenient to accommodate to the spin-flip term of Hund's coupling to be free of the sign problem, nevertheless, finite U does cause this problem. If U is finite, states with doubly occupied orbitals are allowed, and electrons with opposite spins can exchange their locations which causes the sign problem. We will defer the QMC simulations for this case to a later publication, but briefly analyze the physical effect below.

Basically, a large but finite U introduces an antiferromagnetic (AFM) energy scale of $J_{AF} = 4t_\parallel^2/U$ for two electrons lying in adjacent sites in the same chain. Its effect in the low electron density region is unimportant but becomes important in the limit

of $n \to 2$ in which most sites are occupied as spin-1 moments. In this region, the FM energy scale $T_0(n)$ is suppressed because of the low density of mobile holes and finally it becomes weaker than J_{AF}. Consequently, we expect a ground state phase transition at a critical density n_c close to $n = 2$, which marks a transition from the FM ordering at $n < n_c$ to the AFM ordering at $n_c < n < 2$.

2.8 Experiment realizations

The QMC simulations presented above are not only of academic interests but also provide new directions to explore new FM materials in various physical systems, including both the ultra-cold atom optical lattices and the strongly correlated transition metal oxides.

Recently, the study of itinerant FM states has become a research focus in ultra-cold cold atom physics [40, 41, 42, 43, 44, 45, 46, 47]. However, so far it is still in debate whether the experiment results based on the upper branches of the Feshbach resonances have shown the existence of itinerant FM or not. Our work suggests a new direction for the further experiment exploration of itinerant FM in the high orbital bands in optical lattices. Our band Hamiltonian can be accurately implemented in the p-orbital band in the ultra-cold atom optical lattices [87, 88, 89]. Due to the anisotropy of p-orbital orientation, the transverse π-bonding amplitude $t_\perp$ is usually much smaller than the longitudinal σ-bonding $t_\parallel$. The ratio of $t_\perp/t_\parallel$ decreases as increasing the optical potential depth V_0. As shown in Ref. [87], as $V_0/E_R = 15$ where E_R is the recoil energy of the laser forming the optical lattice, $t_\perp/t_\parallel \approx 5\%$, such that we can neglect the $t_\perp$ term in Eq. 2.2. Furthermore, the interaction strength is also tunable in optical lattices by simply varying laser intensities, and the strong coupling regime can be reached. A variation study based on the Gutzwiller projection also shows that the ground state FM may start from

intermediate coupling strength [89]. Our simulations on the thermodynamic properties provide important guidance for future experiments.

Our work is also helpful for the current effort of searching for novel FM materials in transition metal oxides, in particular, in systems with the t_{2g}-orbital bands, i.e., d_{xz}, d_{yz}, and d_{xy} bands, with the quasi-2D layered structure. In fact, FM has been observed experimentally in the (001) interface of $3d$-orbital transition-metal oxides such as $SrTiO_3/LaAlO_3$ [90, 91, 36, 92], which has been a recent research focus in condensed matter physics. The dispersions of d_{xz} and d_{yz}-orbital bands are also highly anisotropic,*i.e.*, the longitudinal bonding parameter $t_{\|}$ is much larger than the transverse one $t_{\perp}$, as described in Eq. 2.2 by replacing $p_{x(y)}$ with $d_{x(y)z}$. The onsite repulsive interaction of the $3d$-electrons are particularly strong, such that the projection of doubly occupied orbitals is a good approximation.

Even though there is an additional quasi 2D-d_{xy}-orbital band in the $SrTiO_3/LaAlO_3$ interfaces, which is presumably paramagnetic by itself, it is conceivable that the overall system remains FM as shown in experiments and our results still apply qualitatively. The reason is that the quasi-1D bands $d_{x(y)z}$ do not hybridize with the quasi-2D d_{xy} band by the nearest neighboring hopping due to their different parity eigenvalues under the reflections with respect to xy, yz and zx-planes, respectively. It is a good approximation that the particle numbers in the d_{xy}-band and in the $d_{x(y)z}$ bands are separately conserved, and they only couple through interactions. The coupling is ferromagnetic by nature due to Hund's rule. Since the quasi-1D bands by themselves are already FM in the strong coupling regime, their coupling to the paramagnetic d_{xy}-band is like to use a permanent ferromagnet to polarize a paramagnet, and it is conceivable that in overall the ferromagnetism is enhanced.

2.9 Conclusions

In summary, we have non-perturbatively investigated the thermodynamic properties of an unambiguous itinerant FM system with multi-orbital structures through the method of the SSE QMC. The simulations are proved to be sign problem free in all the electron density region, and thus reliable numerical results can be obtained at high numeric accuracy. Due to the nature of asymptotic exactness of our simulations, they provide a solid reference point for the study of the strong correlation effects of the thermodynamic properties of itinerant FM systems. There is a wide temperature region $T_0 < T < T_{ch}$, in which the spin channel is incoherent without local moments existing as a priori, while the charge channel exhibits the metallic behavior. The spin magnetic susceptibility exhibits the CW law in the off-critical region as a result of strong correlations. It further crosses over to the exponential growth in the critical region. The compressibility is weakly temperature dependent and saturates to its zero temperature value. The true FM long-range transition appears when the symmetry class is reduced from SU(2) to Ising. The finite size scaling in the critical region gives rise to an accurate determination of the FM transition temperature. Our work is also closely related to the experiment efforts of searching for novel FM states of matter in both ultra-cold atom optical lattices and in the $3d$ transition metal oxide materials.

This chapter contains material published by American Physical Society in: Shenglong Xu, Yi Li and Congjun Wu, "Sign-Problem-Free Quantum Monte Carlo Study on Thermodynamic Properties and Magnetic Phase Transitions in Orbital-Active Itinerant Ferromagnets", Physical Review X 5(2), 021032, 2015. The dissertation author was the primary investigator and author of this paper.

Chapter 3

Mott insulators in SU(N) symmetric Alkaline-earth fermion systems at non-integer filling

3.1 Introduction

Mott insulators are a consequences of the interplay between the lattice structure and strong interaction. Consider a lattice model with integer number of electrons per site, due to Coulomb repulsion, it takes finite amount of energy which is proportional to the repulsion strength to add one more electron into the system, resulting in an insulator. The charge fluctuations vanish as the repulsion goes to infinite. As a paradigm to study magnetism, the Heisenberg model is obtained by considering the virtual hopping on top of the Mott background. The same strategy can also be applied to electronic systems with orbital degrees of freedom. The effective spin exchange / orbital exchange model always have energy scales proportional to $J = 4\frac{t^2}{U}$, the so-called super exchange energy scales, where t is the hopping magnitude and U is the single-particle gap. However,

Mott insulators can also occur at non-integer fillings. For example, in Kagome lattice or honeycomb lattice with P orbitals, the destructive interference of hopping gives rise to localized single-particle states, and flat bands appear in the noninteracting energy spectrum. The states are not localized to a single site but a cluster of sites. At suitable fillings where electrons fill in non-overlapping clusters, the nearest neighboring repulsion can stabilize Mott insulators with charge fluctuation within the cluster. Due the speciality of the flat bands, these systems favors ferromagnetism.

An alternative way to achieve Mott insulators with non-integer fillings is enlarging the symmetry of the Hubbard model to $SU(\mathrm{N})$ with N larger than 2. The simplest example is the SU(N) symmetric Hubbard chains at *half* filling (N/2 particles per site on average). Weak interaction analysis [9] tells us that the systems are insulating for all values of N and the filling is half-integer when N is odd.

Historically, SU(N) symmetry of spin systems was studied to systematically approach the realistic SU(2) symmetric cases and handle the strong correlation [93, 85, 94, 95]. It is found that the larger symmetry groups enhance quantum fluctuation and suppress Neel correlation [93, 9, 85, 96]. This stimulates intensive theoretical research interests predicting the possibilities to realize exotic paramagnetic states, such as various valence bond solid states and spin liquids [97, 98, 99, 100, 101, 102, 103] in systems with large symmetries. However, the large symmetries are quite rare in conventional solid state systems. Although the Hund's coupling facilitates local moments with large spin, the symmetry of the systems usually remains SU(2).

Alternatively, the ultracold atom systems open up new exciting possibilities to physically realize these systems studied theoretically before. The key is that fermionic atoms carry nuclear hyperfine spin larger than 1/2 and allow for the existence of larger symmetry. For example, it is proposed that systems of spin $\frac{3}{2}$ alkali and alkaline-earth atoms exhibit SP(4) symmetry without fine tuning, and the symmetry can be further

enlarged to SU(4) if the interaction is spin-independent [104, 105]. In principle, one can achieve the symmetry as large as SU(10) with ^{87}Sr atoms carrying $9/2$ nuclear spin. Furthermore, the interplay between the nuclear spin and electron orbital degrees of freedom can lead to more complex systems with spin-orbital coupling [106]. Past few years have witnessed significant experimental progress in the field. Various quantum degenerate gases and Mott insulating states of alkaline-earth fermions with large nuclear hyperfine spin have been realized [107, 108, 109, 110, 111, 112, 113, 114, 115, 116]. In particular, G. Pagano and co-workers [116] set up one-dimensional quantum gas of ^{173}Yb atoms with tunable symmetry up to SU(6), providing an experimental route to directly study the evolution of systems of SU(N) symmetry as N increases with flexible control of the interaction strength.

Previous research on the Mott physics in SU(N) symmetric ultracold atom systems mostly focused on integer fillings. In one dimension, both the SU(N) Hubbard chains and Heisenberg chains have been studied at the $1/N$ filling (one fermion per site) in detail, regarding their magnetic and thermal properties [117, 118, 119, 120]. The ground state properties are also investigated for the Heisenberg chains at other fillings [121, 122].

In this work, we focus on the case of half filling, which is integer for even N and half-integer for odd N. We systematically study the effects of the large symmetry on the odd-N systems and compare them with their close relatives, the SU(N) Hubbard chains with N even. As N increases, the density per component stays the same, and the large-N physics is fundamentally different from $1/N$ filling. The difference between even-N and odd-N systems is most pronounced for small values of N, affecting both charge and spin channels. The residual charge fluctuation further suppresses the Neel correlation in the odd-N chains, which shows a stronger tendency to dimerization comparing with even-N chains at typical temperature in ultra-cold atom experiments. As N increases, the boundary between the two sets of Hubbard chains is smeared out by the large symmetry.

Furthermore, we also demonstrate that in the large coupling region, the interaction effects are also suppressed by N. We conjecture that in the large N limit with fixed interaction strength U, the fermionic Hubbard chains are described by the same infrared physics independent U and the parity of N.

3.2 SU(N) Hubbard Model

We consider the 1D SU(N) Hubbard model,

$$H = -t \sum_{\langle ij\rangle,\alpha} c^{\dagger}_{i,\alpha} c_{j,\alpha} + \frac{U}{2} \sum_i n_i(n_i - 1) - \mu \sum_i n_i, \tag{3.1}$$

where $\langle\rangle$ represents the nearest-neighboring bond; the spin index α runs from 1 to N; $n_i = \sum_\alpha c^{\dagger}_{i,\alpha} c_{i,\alpha}$ is the total particle number at site i; $t = 1$ is set as the energy unit. Eq. 3.1 possesses a particle-hole symmetry at $\mu = \frac{N-1}{2}U$, which corresponds to half-filling, i.e., the average particle number per site equals $\frac{N}{2}$.

We will investigate strong correlation effects at large values of N quantitatively, in which the Hilbert space on each site grows exponentially. The typical method for 1D systems of the density-matrix renormalization group becomes difficult to apply. Instead, we will employ the QMC method, which is well-known to be sign-problem free in the path-integral framework in 1D at any filling. The stochastic-series-expansion (SSE) QMC method will be applied with the directed-loop algorithm [80], which allows us to perform the large-scale simulations efficiently to investigate strong correlation effects at large values of N. We will focus on the insulating states at half-filling and the system size is set at $L = 100$ for all simulations below. The finite size effects have been checked to be negligible for the quantities calculated below.

3.3 Ground State Properties

Before presenting the numerical results, let us briefly explain the the relation and difference between the SU(N) spin chains with N even and N odd. The ground states of Eq. 3.1 at half filling are insulating for all values of N when U is repulsive. The systems exhibit spontaneous dimerization with finite spin gaps except for the SU(2) case which is algebraic antiferromagnetic ordered and gapless in the spin sector. In the weak interacting region, the dimerization and the charge gap opening is due to the Umklapp scattering regardless of even and odd values of N. When $N > 2$, the Umklapp scattering couples the charge and spin sector and thus generates a spin gap as well. In this region, there is no qualitative difference between systems with N even and N odd. The charge and the spin gap increase monotonically with N.

However, in the strong coupling limit, the cases of even and odd values of N are crucially different from each other. The average particle numbers are integers and half-integers for even and odd N's, respectively. In the odd-N case, every two sites contain an odd number of fermions on average. Forming two-site singlets is inevitably companied with local charge hopping, which saves extra kinetic energy. Hence, for the odd-N case, there exist both strong intra-dimer charge and spin fluctuations, and both charge and spin gaps are on the order of the hopping amplitude and independent of U. On the other hand, for the even-N case, the dimers are mostly spin-dimers with very small on-site charge fluctuations. The charge is on the order of U and the spin gap is $\sim \frac{t^2}{U}$ from the super exchange mechanism.

These distinct behaviors for system with N odd and even gradually approach each other as the number of flavor increases, which enhances the inter-dimer tunneling. This picture is important for understanding all the even-odd effects that will be studied below.

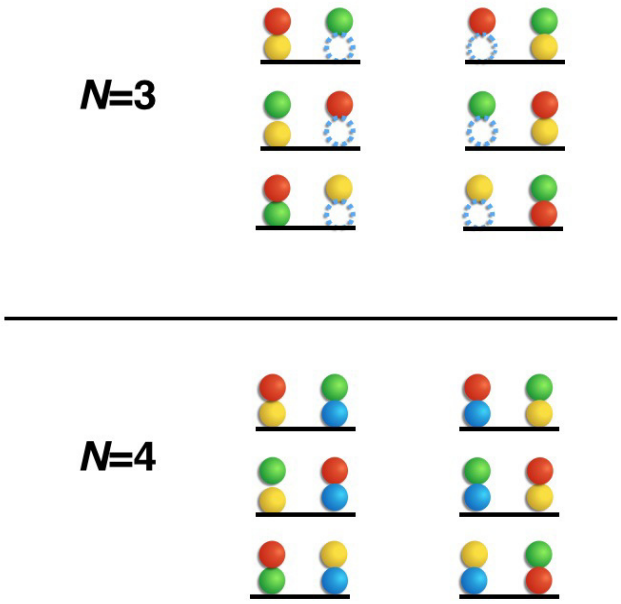

Figure 3.1: The resonating spin configurations for a two-site SU(N) s inglet in the large U limit. The numbers of spin configurations are the same for $N = 2m$ and $N = 2m-1$. The cases of $N = 3$ and $N = 4$ are shown.

3.3.1 Two-site problem and the estimation of the spin gap and the charge gap

In this section, we solve the two-site problem in the large-U limit for both even and odd values of N to gain intuition. We also calculate the corresponding single-particle gaps and the spin gaps.

In the case of even $N = 2m$, each site is filled with m fermions in the large-U limit. The single particle gap is simply $\Delta_{spg} = \frac{U}{2}$. The size of the truncated Hilbert space of the two-site problem is $\left(\frac{(2m)!}{(m!)^2}\right)^2$. The degeneracy of these states is lifted by considering virtual hopping to high energy states. By performing second order perturbation theory, the effective Hamiltonian within the truncated Hilbert space is

$$H_{eff,e} = \frac{2t^2}{U}\left(\sum_{\alpha,\beta} S_{\alpha\beta}(1)S_{\beta\alpha}(2) - \frac{N}{4}\right). \tag{3.2}$$

The ground state of Eq. (3.2) is an SU(N) singlet, denoted as $|0\rangle$, which satisfies

$$(S_{\alpha\beta}(1)+S_{\alpha\beta}(2))\,|0\rangle = 0. \tag{3.3}$$

Therefore the ground state energy of Eq. (3.2) is,

$$\begin{aligned} E_{g,e}(N) &= \frac{2t^2}{U}\left(\sum_{\alpha,\beta} - \langle 0|\, S_{\alpha\beta}(1)S_{\beta\alpha}(1)\,|0\rangle - \frac{N}{4}\right) \\ &= -\frac{J}{8}N(N+2), \end{aligned} \tag{3.4}$$

where $J=\frac{4t^2}{U}$ is the super-exchange energy scale. The ground state contains all N fermion components with $\frac{(2m)!}{(m!)^2}$ resonating spin configurations, as shown in Fig. 3.1. The first excited state belongs to the SU(N) adjoint representation. To obtain the spin gap, one can change one fermion component and calculate the energy difference. The two fermions with the same flavor occupy two different sites are inert in the virtual hopping process, which effectively reduces the fermions number to $N-2$. Therefore, the lowest energy in this sector is the same as the ground state energy E_g for the case of $N'=N-2$. In consequence, the spin gap $\Delta_s = E_{g,e}(N-2)-E_{g,e}(N)=\frac{J}{2}N$.

In the case of odd $N=2m-1$, each site contains either m or $m-1$ fermions in the large-U limit at half-filling. The size of the Hilbert space is still $\left(\frac{(2m)!}{(m!)^2}\right)^2$. Unlike the even-$N$ case, these states are connected through real hoppings. The effective Hamiltonian is

$$H_{eff,o} = -tP\left(\sum_{\alpha} c^{\dagger}_{\alpha,1}c_{\alpha,2}\right)P + h.c., \tag{3.5}$$

where P is the projection operator into the above physical Hilbert space. The ground state is also an SU(N) singlet. With the filling constraint, one can construct two singlet states $|0\rangle_a$ and $|0\rangle_b$. The former has $m-1$ and m fermions on site 1 and 2, respectively, and the latter switches the occupations of these two sites. The ground state is the superposition

of these two as

$$|0\rangle = \frac{\sqrt{2}}{2}(|0\rangle_a + |0\rangle_b). \tag{3.6}$$

The number of the resonating spin configurations is in total $\frac{(2m)!}{(m!)^2}$, the same as the case of $N = 2m$ as shown in Fig. 3.1. To calculate the ground state energy, actually it is easier to compute the expectation value of H^2 with respect to $\langle H^2 \rangle$, and then take the square root. The expression of $H^2_{eff,o}$ is

$$H^2_{eff,o} = -t^2 \left(\sum_{\alpha,\beta} S_{\alpha\beta}(1) S_{\beta\alpha}(2) + \frac{N^2-1}{4N} \right). \tag{3.7}$$

Therefore,

$$\begin{aligned} E_{g,o} &= -\sqrt{\langle 0| H^2_{eff,o} |0\rangle} \\ &= -t \left(\sum_{\alpha,\beta} \langle 0| S_{\alpha\beta}(1) S_{\beta\alpha}(1) |0\rangle + \frac{(N+1)^2}{4N} \right)^{1/2} \\ &= -\frac{N+1}{2} t. \end{aligned} \tag{3.8}$$

For the second line, we have used Eq. (3.3) again.

We now discuss the single particle gap and the spin gap of the odd-N systems. After adding an extra fermion to the system, the real hopping processes are completely forbidden by the filling constraint imposed by the strong Hubbard U, and the energy is zero. Therefore, the single particle gap $\Delta_{spg} = \frac{t}{2}(N+1)$. Similar to the even-$N$ case, the spin gap can be obtained by changing one fermion's flavor and calculate the energy difference. The two fermions with the same flavor occupy the two sites, not participating in hopping processes. As a result, the lowest energy in this sector is the ground state energy for the case of $N' = N-2$, Consequently, the spin gap can be

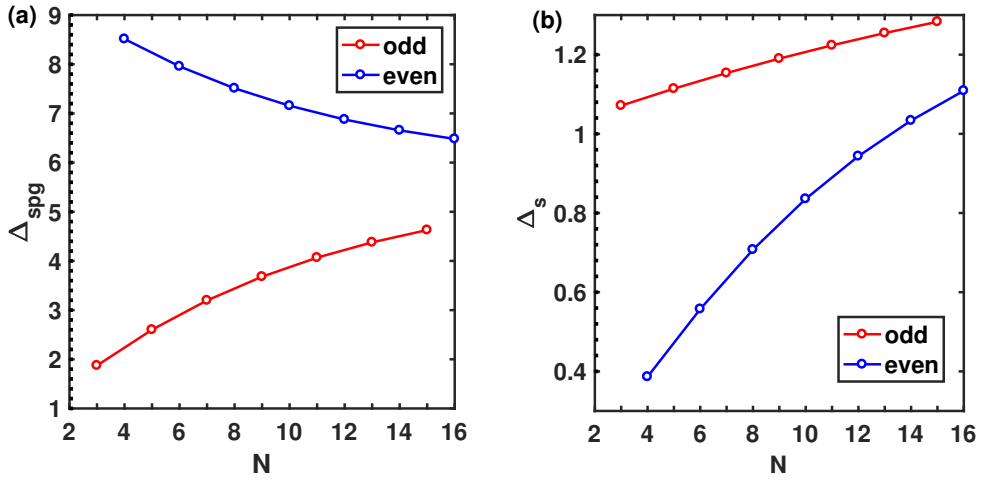

Figure 3.2: The N-dependence of the single particle gap Δ_{spg} (a) and the spin gap Δ_s (b) of the two-site problem. The parameter value is $U/t = 20$. As N increases, the different energy scales of Δ_{spg} and Δ_s between even and odd-N cases gradually merge together.

obtained as $\Delta_s = E_{g,o}(N-2) - E_{g,o}(N) = t$.

To summarize, we have,

N	even	odd
Δ_{spg}	$\frac{U}{2}$	$\frac{t}{2}(N+1)$
Δ_s	$\frac{J}{2}N$	t

(3.9)

The above analysis works in the strong interaction region $U/t \gg N$, where the even-N systems and odd-N systems exhibit distinct energy scales. Using exact diagonalization, we demonstrate that increasing N with fixed U reduces the difference, and the two kinds of systems approach the same limit, as shown in Fig. 3.2, where the N dependences of both Δ_{spg} and Δ_s are presented.

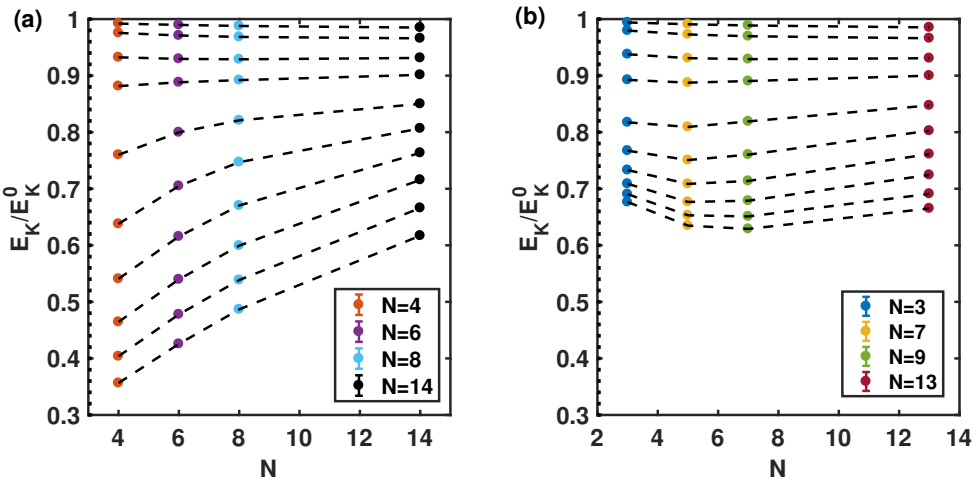

Figure 3.3: The normalized kinetic energy scale $\tilde{E}_k$ as a function of N for U varying from $0.5t$ to $15t$. $\tilde{E}_k$ equals 1 for the noninteracting limit and equals 0 when the charge degrees of freedom complete freeze. (a) The case of even N. In the weak coupling regime, $\tilde{E}_k$ decreases with N, while in the strong coupling regime, $\tilde{E}_k$ increases with N. The crossover of the two regimes occurs at $U \sim 2.5t$. (b) The case of odd N. The weak coupling behavior is similar to the even-N case. In the strong coupling regime, $\tilde{E}_k$ first decreases and then increases with N, because of the two competing effects of enlarging the symmetry.

3.3.2 Kinetic energy scale

In the charge channel, the interaction effects can be characterized by the kinetic energy scale per flavor, $E_K = \frac{1}{LN} | \sum_{k,\alpha} 2\cos k \langle c^\dagger_{k,\alpha} c_{k,\alpha} \rangle |$. In Fig. 3.3, the N dependence of the normalized kinetic energy scale E_K/E_K^0 is plotted for U ranging from 0.5 to 15, where E_K^0 is the noninteracting value. In both even N and odd N cases, the curves do not cross simply because U suppresses the kinetic energy scale. For small U, ground states are already insulating but with a small charge gap. Therefore, the single-particle correlation length is still long comparing with the lattice spacing and the itinerant picture holds. As increasing N, each particle experiences stronger impedance from other particles, and E_k decreases monotonically. This argument holds equally well for both even and odd N systems, and they show similar behavior indeed.

Conversely, dramatic even-odd effects appear in the strong coupling regime.

The systems with N odd overall have larger kinetic energy scale due to the residue charge fluctuation. When N is even, E_k increases roughly linearly with N, whereas non-monotonic behavior is observed in the odd-N case. The behavior of even N can be simply understood by considering the virtual hopping on the background of a Mott insulator where the charge fluctuation is completely frozen. The total number of virtual hopping processes scale as N^2, leading to the linear N dependence of the kinetic energy scale per flavor. Therefore, the interaction effect is reduced by increasing the number of components here. On the other hand, for odd N cases, increasing N has two competing effects. The first is to reduce the intra-dimer charge fluctuation as well as E_k; the second is to enhance the inter-dimer tunneling, which tends to increase E_k, similar to the even N systems. The first effect is more notable in the regime of small N but overcome by the second one when N is large enough. The minimal position of E_k roughly scales as U/t. When N passes the turnover point, the interaction effect is reduced, and the disparity between even N and odd N originated from the filling is diminished by the amplification of charge fluctuation, as expected from the large-N picture.

Remarkably, in the even N cases, numerical data suggests the kinetic energy is independent of N when U is $2 \sim 3t$. The corresponding curve is labeled red in Fig. 3.3(a). This curve clearly separates the weak coupling and strong coupling regime. In both cases, as N increases, the kinetic energy gradually approaches this curve, but from opposite direction. The situation is the same for odd N, as long as E_K passes the minimum. Based on this observation, we conjecture that E_k is independent of the coupling magnitude in the large N limit, as long as U is finite.

3.3.3 Momentum distribution

The kinetic energy is directly related to the momentum distribution function $n(k) = \frac{1}{N}\sum_\alpha c^\dagger_{\alpha,k} c_{\alpha,k}$, which is the standard quantity to measure in the ultracold atom

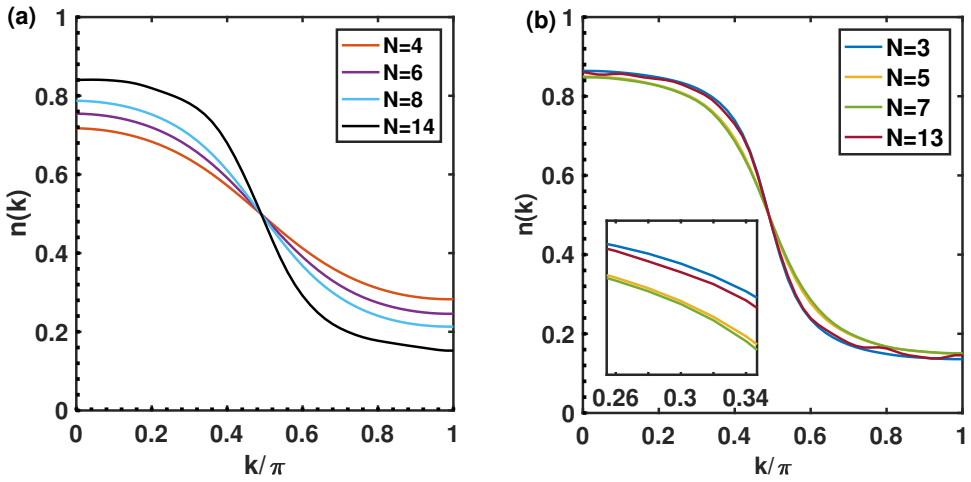

Figure 3.4: The momentum distribution functions $n(k)$ at $U = 11t$. For all values of N, $n(\pi/2) = 1/2$ because of the combination of the particle-hole and the inversion symmetries. (a) In the case of even N, increasing N enhances local charge fluctuation and drives $n(k)$ to the side of weak coupling regime. (b) In the case of odd N, $n(k)$ instead exhibits non monotonic behavior. This observation is consistent with the kinetic energy scale $\tilde{E}_k$

experiment via the time of flight method. We present the momentum distribution function for both even and odd cases in the strong coupling regime, say $U = 10t$. Due to both inversion symmetry and particle hole symmetry, all the curves cross at $1/2$ for $k = \pi/2$. In sharp contrast with monotonic broadening of $n(k)$ as increasing N, which is observed in 1D quantum gases [116], here, $n(k)$ has rather different behavior because of the Mott physics. In the even N cases, instead, $n(k)$ is sharpened by increasing N, because of the enhanced charged fluctuation above the Mott background. In odd N cases, similar to their kinetic energy, $n(k)$ exhibits non monotonic behavior. These phenomena are consistent with the analysis of the kinetic energy scale E_K above. We note that in the weak coupling regime, the usual monotonic broadening is observed.

3.3.4 The relation between SU($2m$) and SU($2m-1$) in the spin channel

In this section, we elucidate the connection between the systems with SU($2m$) and SU($2m-1$) symmetry in the strong coupling limit. When $N = 2m$, the strong on-site repulsion suppresses charge fluctuation, and each site have m fermions. The Heisenberg term resulting from the second order perturbation favors two-site singlet state, subjected to the particle number constraint. The dimer-state reads, up to a normalization factor,

$$|0\rangle_{2m} = \varepsilon^{\alpha_1 \ldots \alpha_{2m}} \prod_{k=1}^{m} c^{\dagger}_{\alpha_k, i} \prod_{k=m+1}^{2m} c^{\dagger}_{\alpha_k, j} |vac\rangle \tag{3.10}$$

with $\varepsilon^{\alpha_1 \ldots \alpha_{2m}}$ the total antisymmetric tensor. The repeated indices α_i are summed over all N flavors

On the other hand, when $N = 2m-1$, the strong repulsion U requires that the on-site particle number is either m or $m-1$. Therefore local charge fluctuation is still allowed even in the infinite coupling limit. Different from the even N case, there are two two-site singlet states. The hopping terms favors the following particular combination,

$$\begin{aligned} |0\rangle_{2m-1} = \varepsilon^{\alpha_1 \ldots \alpha_{2m-1}} (& \prod_{k=1}^{m-1} c^{\dagger}_{i,\alpha_k} \prod_{k=m}^{N} c^{\dagger}_{j,\alpha_k} + \\ & \prod_{k=1}^{m} c^{\dagger}_{i,\alpha_k} \prod_{k=m+1}^{N} c^{\dagger}_{j,\alpha_k}) |vac\rangle \end{aligned} \tag{3.11}$$

There is a way to unify these two very different pictures. We note that there is one to one correspondence between the states in the truncated Hilbert space for $N = 2m$ and $N = 2m-1$. In the latter case, we introduce a fermionic operator $c^{\dagger}_{*}$, which creates a fermion with an extra artificial flavor. For on-site states with $m-1$ particles, we assume that they also contain the fermion with this extra flavor and have total m fermions.

Now the on-site particle number constraint becomes $\sum_{\alpha} c^{\dagger}_{\alpha,i} c_{\alpha,i} = m$. The operator $\sum_{i} c^{\dagger}_{*} c_{*}$ measures the number of holes in the $N = 2m-1$ systems. With the extra fermionic operator, we can write the two-site singlet state as:

$$|0\rangle_{2m-1} = \varepsilon^{\alpha_1 \ldots \alpha_{2m}} \prod_{k=1}^{m} c^{\dagger}_{\alpha_k,i} \prod_{k=m+1}^{2m} c^{\dagger}_{\alpha_k,j} |vac\rangle \tag{3.12}$$

The repeated indices α_i are not only summed over the original $2m-1$ flavors, but also the extra flavor $*$. This special combination of the two singlet states has the exact the same form of Eq. 3.10, and manifestly exhibits hidden SU($2m$) symmetry. It follows directly that any spin-spin correlator measured from the two-site singlet states gives the same value for $N = 2m$ and $N = 2m-1$, as long as the correlator does not involve the extra flavor $*$. This explains the similarity of the spin structure factor between the two cases demonstrated in Fig. 3.5.

3.3.5 Effective spin model for system with N odd

Furthermore, we can derive an effective spin model for systems with N odd in the infinite U limit. In the Hilbert space with the extra flavor $*$, the net effect of the original hopping term $c^{\dagger}_{\alpha,i} c_{\alpha,j} + h.c$ is exchanging the real flavor α and the artificial flavor $*$. The effective spin Hamiltonian thus reads:

$$\begin{aligned} H_{eff} &= t \sum_{\langle i,j \rangle, \alpha \neq *} S_{*\alpha,i} S_{\alpha *,j} + h.c. \\ &= t \sum_{\langle i,j \rangle} \left(\sum_{\alpha\beta} S_{\beta\alpha,i} S_{\alpha\beta,j} - \sum_{\alpha \& \beta \neq *} S_{\beta\alpha,i} S_{\alpha\beta,j} - S_{**,i} S_{**,j} \right) \end{aligned} \tag{3.13}$$

The first term has emergent SU($2m$) symmetry, which is explicit broken by the second term. The whole Hamiltonian has SU($2m-1$)$\otimes$ U(1) symmetry, as expected. Comparing with usual SU($2m$) Heisenberg model, this model is more frustrated due to the sign of the

second term. This explains that in the strong coupling regime, the spin structure factor $S_{spin}(\pi)$ with $N = 2m$ surpasses that with $N = 2m-1$.

Dramatically different from the SU($2m$) Heisenberg model, where the spin energy scale is $\frac{t^2}{U}$, here the spin energy scale is t. Although the dimer order does not persist at finite temperature, the correlation length already starts to grow exponentially when the temperature reaches to the scale of the hopping energy, whereas in the even N case, this happens when the temperature reaches exchange energy scale, which is much lower. Since cooling the temperature down to the exchange energy scale of the spin system is the most severe obstacle in the ultracold atom community, this discovery provides a new perspective to realize spin models and measure the ground state property in experiments.

3.3.6 Spin structure factor

We now present the two-site spin-spin correlation function defined as

$$C_{spin}(i,j) = \frac{1}{2C(N)} \sum_{ij,\alpha\beta} \langle S_{\alpha\beta}(r_i) S_{\beta\alpha}(r_j) \rangle. \tag{3.14}$$

Where $S_{\alpha\beta}(r_i)$ is the on-site generator of the SU(N) symmetry, $S_{\alpha\beta}(r_i) = c^{\dagger}_{i,\alpha} c_{i,\beta} - \frac{n_i}{N}\delta_{\alpha\beta}$. The normalization factor $C(N)$ is the Casimir for $1^{N/2}$ representation when N is even and $1^{(N+1)/2}$ representation when N is odd. It reads $\frac{N(N+1)}{8}$ and $\frac{(N+1)^2(N-1)}{8N}$ for even and odd N, respectively. With this convention, the onsite correlation function $C_{spin}(i,i)$ approaches one in the large U limit for all values of N. Furthermore, the correlation functions $C_{spin}(i,j)$ of maximal Neel ordered states are also independent of N. Therefore the spin structure factor $S_{spin}(k = \pi)$, the Fourier transformation of $C_{spin}(i,j)$ evaluated at π is used as criteria for comparing the antiferromagnetic correlation for systems with different values of N. In our simulation, due to the SU(N) symmetry, S_k can be reduced to the average over only diagonal generators ($\alpha = \beta$), for the purpose of simpler numerical

implementation.

In Fig. 3.5 (a), we present the N dependence of $S_{spin}(\pi)$ in the strong coupling region $U = 15t$ at fairly low temperature $\beta = 30$. The spin structure factor decreases rapidly with N, since the large symmetry enhances quantum fluctuation and suppresses the antiferromagnetic correlation. It is also affected by the parity of N. Although, the spin channel properties of $N = 2m$ and $N = 2m-1$ are closely related, Fig. 3.5 (a) clearly demonstrates that systems with $N = 2m-1$ have relatively weaker Neel correlation. The charge fluctuation in the systems with odd-N further suppresses the antiferromagnetic correlation and favors dimerized states over Neel states. The reason is that in the ideal Neel states, the charge degrees of freedom are frozen whereas the dimerized states still allow for charge fluctuation.

We also study the interaction effects on the spin structure factor. We plot $S_{spin}(\pi)$ for even N and interaction strength U ranging from $0.5t$ to $15t$ in Fig. 3.5 (b). Similar to the kinetic energy scale, as U increases, $S_{spin}(\pi)$ exhibits opposite behavior in the weak and strong coupling regime. As N increases, the difference between the weak coupling regime and the strong coupling regime decreases rapidly, another evidence that the interaction effect is reduced by the large symmetry. The U dependence of $S_{spin}(\pi)$ for odd-N systems has the similar behavior and thus is omitted here.

3.4 Finite entropy and dimer-dimer correlation length

Now we discuss the experimental realization of the even-odd effects discussed before. In ultracold atom experiment, because of the extreme small tunneling amplitude or the Fermi energy scale ($\sim K$), it is usually difficult to cool the system down to the ground state or even the exchange energy scale. Currently, the lowest entropy realizable is $\sim 0.6k_B$ per particle for the fermionic Hubbard model in the Mott state. In the center

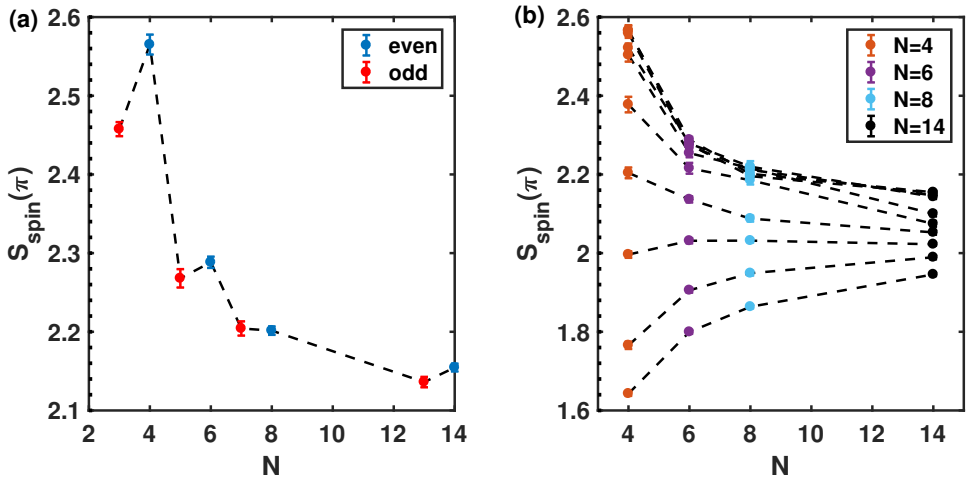

Figure 3.5: The N-dependence of the spin structure factor. (a) The N dependence of the spin structure factor $S_{spin}(\pi)$ in the strong coupling regime, where $U = 15t$. As N increases, $S_{spin}(\pi)$ drops rapidly, a signature that the large symmetry suppresses Neel correlation. Comparing the systems with opposite parity of N, $S_{spin}(\pi)$ for odd N is smaller because of the local charge fluctuation. (b) Similar to the kinetic energy scale, $S_{spin}(\pi)$ exhibits opposite N dependence in the weak and strong coupling regime for even-N. The case of odd-N is similar and is omitted here. The crossover happens around $U = 2.5t$, consistent with E_k shown in Fig. 3.3 (a).

of the harmonic trap, the entropy per particle is slightly lower, but the corresponding temperature is still above the super exchange energy scale t^2/U. However, as explained before, the dimerization of the SU(N) chains with N odd does not rely on super exchange but rather local charge fluctuation and the corresponding spin gap is on the order of the tunneling amplitude, which is one order larger than the super exchange energy scale. Therefore, we propose that the systems with N odd are better experimental candidates to observe the dimerization. This advantage of odd N is more prominent for small Ns ($N = 3,5,7$) which are experimental accessible using ^{173} Yb and ^{87}Sr atoms.

To illustrate the point, we first study the the evolution of temperatures of the systems as one adiabatically turn on the interaction. The temperature dependence of specific entropy (entropy per particle) $S(T)$ is obtained from the thermodynamic relation

as,

$$\mathcal{S}(T) = \ln 4 + \frac{E(T)}{T} - \int_T^\infty dT \frac{E(T)}{T^2}, \tag{3.15}$$

where $\ln 4$ is the entropy at the infinite temperature limit and $E(T)$ is the internal energy per particle. The entropy-temperature relations are shown for U ranging from t to $13t$ and N ranging from 3 to 8 in Fig. 3.6. Comparing the case of $N = 3$ and $N = 4$, the $\mathcal{S} - T$ for $N = 4$ displays a plateau around $\mathcal{S} = 0.6k_B$ that is missing in the odd N case. The reason is that in the even N, when the temperature is much smaller than the single-particle gap $U/2$ but much higher than the super exchange energy scale, $\mathcal{S}$ mostly comes from the spin degrees of freedom that are basically free in the temperature region, and therefore has a weak temperature dependence. As N increases, the difference between even and odd N's diminishes.

We present the isoentropy curves in the T-U plane for different values of N in Fig. 3.7(a) for different values of N, considering a specific entropy below but close to the experimental availability, say, $S = 0.3$. The corresponding temperatures vary but remain at the order of $0.1t$. An overall trend is that temperature T decreases as increasing U for all values of N as a reminiscence of the celebrated Pomeranchuk effect [119, 123, 124, 125]. Increasing U drives the system more local-moment like, and thus temperature drops to keep the entropy invariant. Remarkably, these curves behave dramatically different for even and odd values of N. This is in sharp contrast to the case of $1/N$-filling investigated before [119, 120], in which T monotonically decreases as increasing N simply because of the $\ln N$ scaling of the specific entropy. At half-filling and in the large U region, fermions in the even N case are much more local-moment-like than that in the odd N case, and thus possess higher entropy capacity. As a result, the temperatures of even-N curves fall lower than those of the odd-N's. The temperature T of

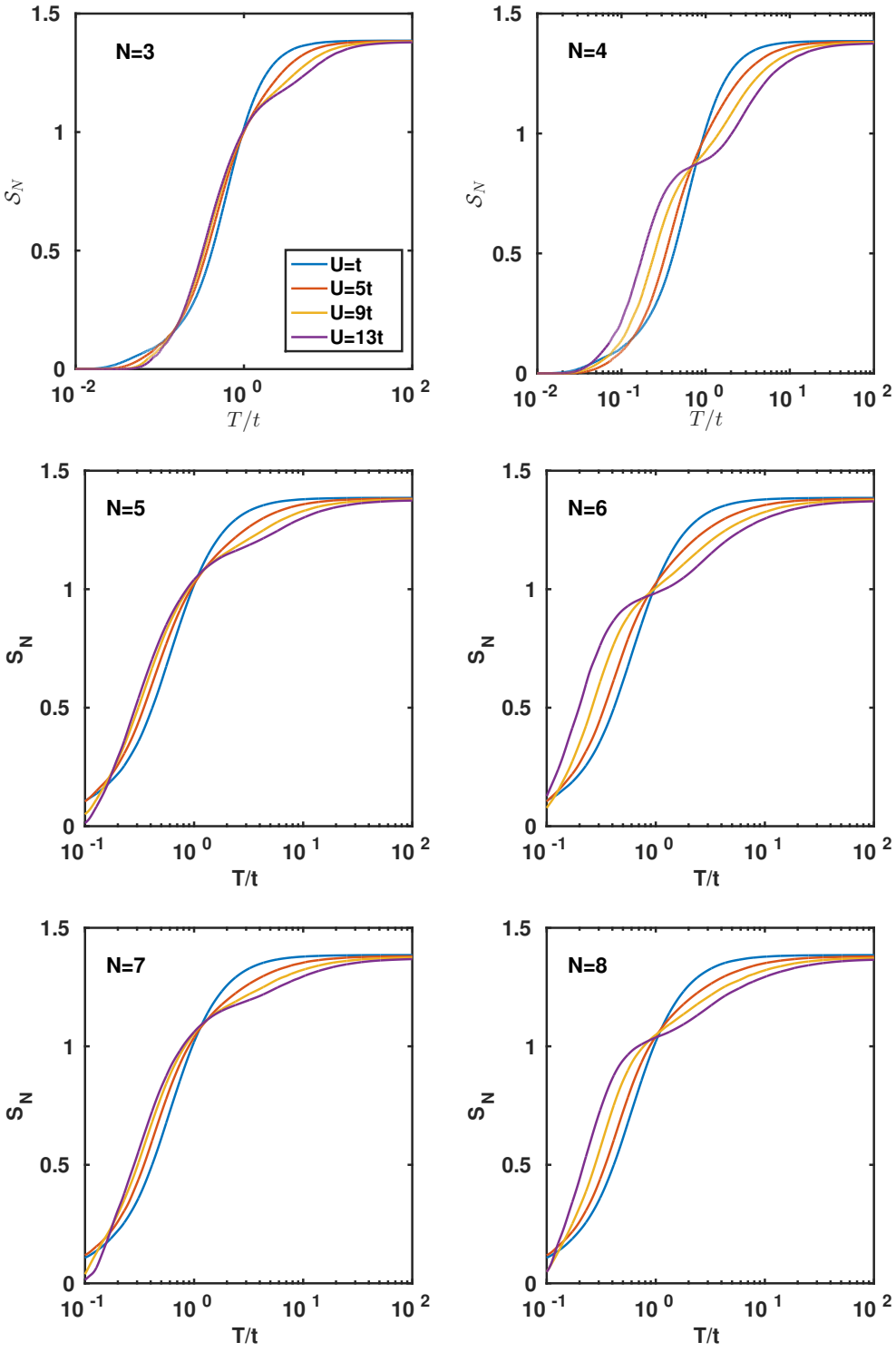

Figure 3.6: The temperature-entropy relation of N from 3 up to 8 and $U/t = 1, 5, 9, 13$ obtained by numerical integration of the energy from temperature as high as $1000t$ (not shown in the figure). The lowest T shown here is $0.1t$.

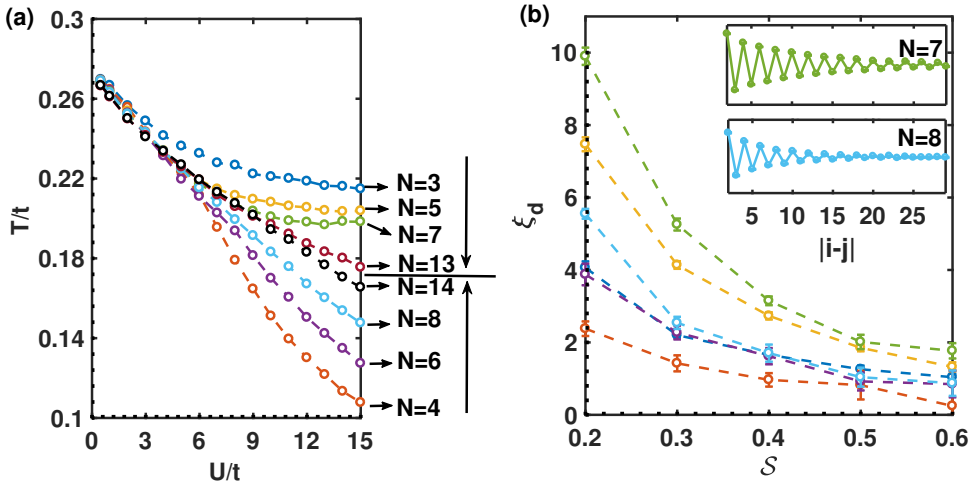

Figure 3.7: Isoentropy curves at fixed specific entropy $S = 0.3$ and the entropy-dependence of the dimer correlation length. (a) Isoentropy curves in the T-U plane at a fixed specific entropy $S = 0.3$. As adiabatically turning on the interaction to the strong coupling regime, the final temperature increases with N for even N but decreases with N for odd N. The isoentropy curves merge together in the large-N limit regardless of the parity of N. (b) The dimer correlation length increases rapidly as the entropy decreases. The odd-N systems overall exhibit stronger tendency to the dimerized phase than even-N systems. In the inset, the real space correlation function $C_{dimer}(i, j)$ is shown for $N = 7$ and $N = 8$ at $\mathcal{S} = 0.2k_B$ for comparison.

the odd-N curves tend to saturate in the large-U limit. This is consistent with the picture that every two sites form a dimer where finite charge fluctuation persists. Furthermore, as shown in previous studies [124, 123], increasing N enhances charge fluctuations when N is even, which softens the Mott gap and drives the system less local-moment-like. This reduces the entropy capacity and thus temperatures increase as N increases. In contrast, there are still significant local charge fluctuations in the odd N case even in the large U limit. Increasing N further enhances the collision among fermions, and reduces the fermion itinerary, which increases the entropy capacity and reduces the temperature.

After adiabatically turning on the interaction, as shown in Fig. 3.7(a), the final temperatures are well-below the ordering energy scale of odd N but above the super exchange energy. Strictly speaking, the fermionic chains cannot order at finite temperature, but the systems with N odd should develop longer correlation length ξ_{dimer}. To confirm this, we calculate the kinetic energy correlation functions,

$$C_{dimer}(r_i - r_j) = \frac{1}{N}\sum_{\alpha}\langle K_{\alpha,r_i} K_{\alpha,r_j}\rangle, \tag{3.16}$$

where $K_i = c^{\dagger}_{\alpha,i} c_{\alpha,i+1} + h.c.$. The dimer correlation lengths are extracted from the correlation function and plotted in Fig. 3.7(b) as a function of the specific entropy. We are interested in the strong coupling regime and thus set the interaction strength to $15t$. As expected, the odd-N systems overall exhibit longer correlation lengths. As S decreases, ξ_{dimer} grows much faster in the odd N case. The real space correlation functions of $N = 7$ and $N = 8$ are shown in the inset for comparison. The dimer correlation is visible ~ 30 lattice spacing away for $N = 7$. This indicates that systems with N odd are better candidates for detecting the dimer order. Experimentally, the dimer ordering can be detected using the double-well technique.

3.5 Conclusion

We have non-perturbatively studied the one-dimensional SU(N) fermion lattice systems at half-filling. In the strong interaction region, the odd-N systems exhibit stronger charge fluctuations and dimerization than the even N. As N reaches the level of U/t, the virtual hopping processes dominate in both even and odd N systems, and the interaction effects are weakened as increasing N. Whereas from the weak interaction limit, increasing N enhances particle collisions and strengthens the interaction effect. These two distinct behaviors approach a crossover region around $U \sim 2.5t$ from opposite directions, as demonstrated in experimentally measurable quantities including the kinetic energy scale, the momentum distribution functions and spin structure factors. The above features of how interaction effects scale with N are expected to be qualitatively valid in two and higher dimensions as well, which will be deferred to a future study.

This chapter contains material from the following preprint being prepared for submission for publication: Shenglong Xu, Julio Barreiro, Yu Wang, and Congjun Wu. "Interaction effects from the parity of N in SU(N) symmetric fermion lattice systems." arXiv:1707.01463 (2017). The dissertation author was the primary investigator and author of this paper.

Chapter 4

Electrons in the lattices with mixing space-time symmetry

4.1 Introduction

The fundamental concept of energy bands in crystals based on the Bloch theorem lays the foundation of modern condensed matter physics. In the past decade, studies on band structure symmetry and topology lead to important discoveries of the topological insulating state, topological superconductivity, and the Weyl semi-metal state [126, 127, 15]. More recently, periodically driven systems have also attracted increasing interests. Periodic driving provides a new route to engineer topological states in systems originally topologically trivial in the absence of driving. Such possibilities have been explored in various systems, including the irradiated graphene [128, 129], semiconducting quantum wells [130], dynamically modulated cold atom optical lattices [131], and photonic systems [132, 133]. For driven systems with a temporal period T, Bloch bands are replaced by Bloch-Floquet bands, which are periodic in energy space since the quasi-energy is only conserved module $2\pi/T$. This feature further enriches topological band

structures [134, 135, 136]. For non-interacting systems, this extra periodicity leads to the dynamically generated Majorana modes in 1D [137], and anomalous edge states with zero Chern number in 2D [138]. Topological classifications for interacting Floquet systems have also been investigated [139, 140, 141, 142, 143].

Symmetry plays a fundamental role in analyzing topological properties of periodically driven systems. However, previous studies mostly treat the temporal periodicity separated from the spatial one. In fact, the driven system can exhibit much richer symmetry structures than a simple direct product of symmetries in space and time domains. In particular, a temporal translation at a *fractional* period can be combined with space group symmetries to form novel space-time intertwined symmetries, which, to the best of our knowledge, have not yet been fully explored. For static lattices, the intrinsic connections between the space-group symmetries and physical properties, especially the topological phases, have been extensively studied [144, 145, 12, 146, 147]. Therefore, it is expected that the intertwined space-time symmetries could also protect novel trivial properties of the driven system, regardless of microscopic details.

In this article, we generalize the concept of Floquet-Bloch lattices to space-time crystals, which exhibit intertwined space-time symmetries. Space-time crystals exhibit the periodicities characterized by $D+1$ linearly independent basis vectors, which are space-time mixed in general. The usual Floquet-Bloch systems are a special case exhibiting separate spatial and temporal periodicities. The full discrete space-time symmetries of space-time crystals form groups – dubbed "space-time" groups, which are generalizations of space groups for static crystals by including "time-screw" and "time-glide" operations. A complete classification of the 13 space-time groups in 1+1 D is performed, and their constraints on band structure winding numbers are studied. In 2+1 D, the non-symmorphic space-time symmetry operations, similar to their static space-group counterparts, lead to spectral degeneracies for periodically driven systems,

even when the instantaneous spectra are gapped at any given time t.

4.2 Space-time lattice

We consider the time-dependent Hamiltonian $H = P^2/(2m) + V(\mathbf{r},t)$ in the $D+1$ dimensional space-time. $V(\mathbf{r},t)$ exhibits the intertwined discrete space-time translational symmetry as

$$V(\mathbf{r},t) = V(\mathbf{r}+\mathbf{u}^i, t+\tau^i), \quad i = 1,2,...,D+1, \tag{4.1}$$

where $(\mathbf{u}^i, \tau^i) = a^i$ is the primitive basis vector of the space-time lattice. Eq. 4.1 extends the usual Floquet-Bloch lattice with the separated spatial and temporal periodicities to the more general case with space-time mixed primitive vectors. In general, the space-time primitive unit cell is not a direct product between spatial and temporal domains. There may not even exist spatial translational symmetry at any given time t, nor temporal translational symmetry at any spatial location $\mathbf{r}$. Consequently, the frequently used time-evolution operator $U(T)$ of one period for the Floquet problem generally does not apply. The reciprocal lattice is spanned by the momentum-energy basis vectors $b^i = (\mathbf{G^i}, \Omega^i)$ defined through $b^i \cdot a^j = \sum_{m=1}^{D} G^i_m u^j_m - \Omega^i \tau^j = 2\pi\delta^{ij}$. The $D+1$ dimensional momentum-energy Brillouin zone (MEBZ) may also be momentum-energy mixed.

We generalize the Floquet-Bloch theorem for the time-dependent Schrödinger equation $i\hbar\partial_t \psi(\mathbf{r},t) = H(\mathbf{r},t)\psi(\mathbf{r},t)$. Due to the space-time translation symmetry, the lattice momentum-energy vector $\kappa = (\mathbf{k}, \omega)$ is conserved. Only the κ vectors inside the first MEBZ are non-equivalent, and the κ vectors outside are equivalent to those inside up to integer reciprocal lattice vectors. The states characterized by κ take the form of

$$\psi_{\kappa,m}(\mathbf{r},t) \quad = \quad e^{i(\mathbf{k}\cdot\mathbf{r} - \omega_m t)} u_m(\mathbf{r},t), \tag{4.2}$$

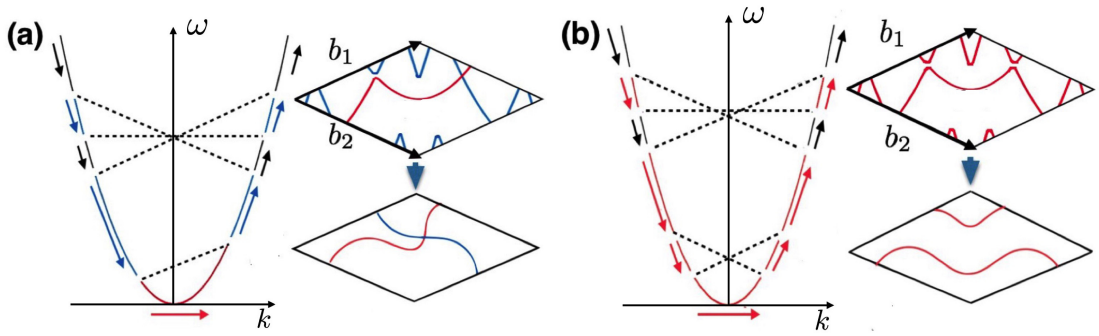

Figure 4.1: Folding the band dispersions of the 1+1 D space-time crystal into the 1st rhombic MEBZ in the weak lattice limit. The momentum-energy reciprocal lattice vectors of nonzero V_B's are represented by dashed lines. The low-energy part of the free dispersion curve evolves to closed loops. (a) Two loops with the winding numbers $\mathbf{w_r} = (1,0)$ (red) and $\mathbf{w_b} = (0,1)$ (blue). (b) An extra nonzero V_G connects two loops in (a) forming a new one with $\mathbf{w} = \mathbf{w_r} + \mathbf{w_b}$.

where m marks different states sharing the common κ. $u_m(\mathbf{r},t)$ processes the same space-time periodicity as $H(\mathbf{r},t)$, and is expanded as $u_m = \sum_B c_{m,B} e^{i(\mathbf{G}\cdot\mathbf{r}-\Omega t)}$ with $B = (\mathbf{G},\Omega)$ taking all the momentum-energy reciprocal lattice vectors. The eigen-frequency ω_m is determined through the eigenvalue problem defined as

$$\begin{aligned} \sum_{B'}\{[-\Omega &+ \varepsilon_0(\mathbf{k}+\mathbf{G})]\delta_{B,B'} + V_{B-B'}\}c_{m,B'} \\ &= \omega_m c_{m,B}, \end{aligned} \tag{4.3}$$

where $\varepsilon_0(\mathbf{k})$ is the free dispersion, and V_B is the momentum-energy Fourier component of the space-time lattice potential $V(\mathbf{r},t)$. The dispersion based on Eq. 4.3 is represented by a D-dimensional surface in the MEBZ which is a D+1 dimensional torus.

4.2.1 1+1 D

The energy band structures of the space-time lattice exhibit novel features different from those with separated spatial and temporal periodicities. For simplicity, below we use the 1+1 D case to investigate the symmetry and topological properties of the

space-time crystal.

The dispersion relation $\omega(k)$ forms closed loops in the 2D toroidal MEBZ, each of which is characterized by a pair of winding numbers $\mathbf{w} = (w_1, w_2)$. Compared to the static lattice case in which the band dispersion only winds around the momentum direction, here $\omega(k)$ is typically not single-valued and its winding patterns are much richer. The dispersions in the limit of a weak space-time potential $V(x,t)$ with a rhombic MEBZ are illustrated in Fig. 4.1 (a) and (b). When folded into the MEBZ, the free dispersion curve $\varepsilon(k)$ can cross at general points not just on high symmetry ones. A crossing point corresponds to two equivalent momentum-energy points related by a reciprocal vector G before folding. When $V_G \neq 0$, the crossing is avoided by forming a gap at the magnitude of $2|V_G|$. The winding directions of the dispersion loops are generally momentum-energy mixed. Furthermore, different momentum-energy reciprocal lattice vectors can cross each other, leading to composite loops winding around the MEBZ along both directions as shown in Fig. 4.1 (b). The total number of states at each $\mathbf{k}$ is invariant with lattice potential, then crossing can only split along the ω-direction and $d\omega/dk$ is always finite. Consequently, trivial loops with the winding numbers $(0,0)$ are forbidden, while all other patterns (w_1, w_2) are possible in general.

The intertwined space-time lattice symmetries besides translations can protect crossings and impose further constraints on band structures. Consider a 1+1 D crystal structure with the space-time unit cell as the direct product of spatial and temporal periods λ and T, respectively. Its first MEBZ is also a direct-product as $[-\pi/\lambda, \pi/\lambda] \otimes [-\pi/T, \pi/T]$. We further assume the system is invariant under a combined time-reversal transformation followed by the translation of a half spatial period. This operation denoted as g_t can be viewed as a "glide time-reflection" defined as $g_t(x,t) = (x + \frac{1}{2}\lambda, -t)$. Its operation on the Hamiltonian is defined as $g_t^{-1} H g_t = H^*(g_t(x,t))$. The corresponding transformation M_{g_t} on the Bloch-Floquet wavefunction $\psi_\kappa(x,t)$ of Eq. 4.2 is anti-unitary

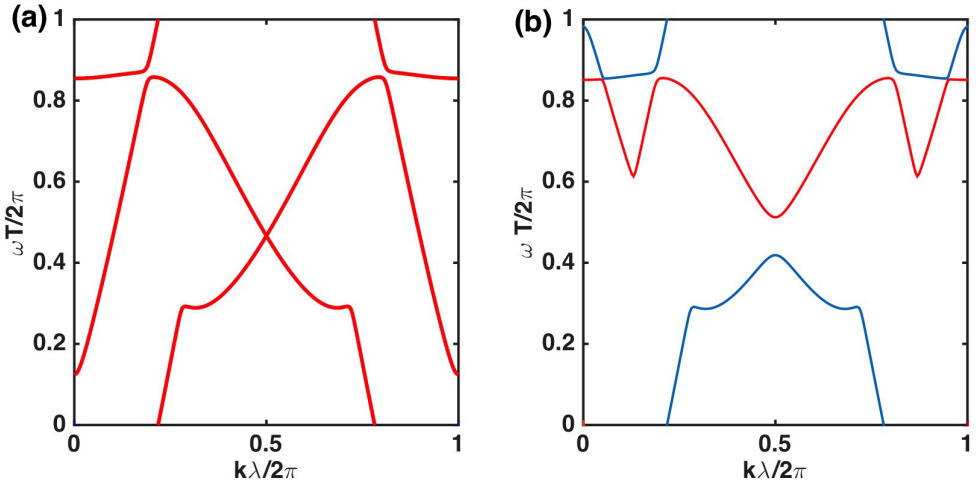

Figure 4.2: The glide time-reflection symmetry leads to the double-degeneracy in the spectrum. (a) The Floquet-Bloch band spectrum with the space-time lattice potential possessing the glide time-reflection symmetry g_t. When applied to the states with $\kappa_x = \pi/\lambda$, g_t becomes a Kramers symmetry protecting the double-degeneracy. (b) Lifting the Kramers degeneracy by adding a glide time-reflection symmetry breaking term.

.

defined as $M_{g_t}\psi_\kappa = \psi^*_\kappa(g_t^{-1}(x,t))$. The glide time-reflection leaves the line of $\kappa_x = \pi/\lambda$ in the MEBZ invariant. M_{g_t} becomes a Kramers symmetry for states along this line,

$$M^2_{g_t}\psi_\kappa = \psi_\kappa(x-\lambda,t) = e^{-i\kappa_x\lambda}\psi_\kappa = -\psi_\kappa, \tag{4.4}$$

which arises purely from the space-time crystal symmetry without involving the half-integer spinor structure. It protects the double degeneracy of the momentum-energy quantum numbers of ψ_κ and $M_{g_t}\psi_\kappa$. Hence the crossing at $\kappa_x = \pi/\lambda$ cannot be avoided and the dispersion winding numbers along the momentum direction must be even.

As a concrete example, we study a crystal potential with the above spatial and temporal periodicities, $V(x,t) = V_0\big(\sin\frac{2\pi}{T}t\cos\frac{2\pi}{\lambda}x + \cos\frac{2\pi}{T}t\big)$. Except the glide time-reflection symmetry, it does not possess other space-time symmetries. Its Bloch-Floquet spectrum is calculated based on Eq. 4.3, and a representative dispersion loop is plotted in

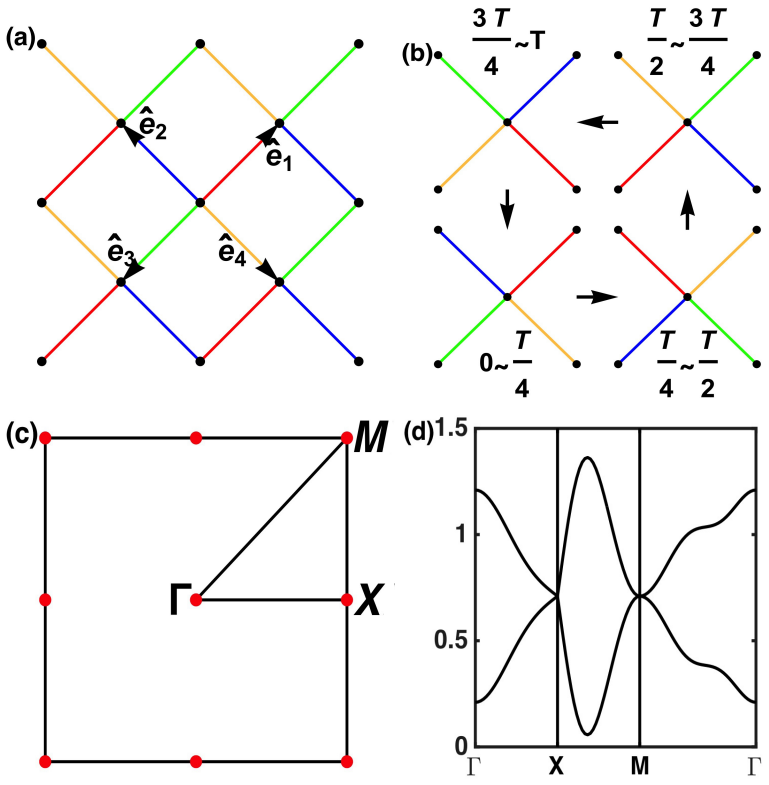

Figure 4.3: A specific model demonstrates that the time-screw rotation protects spectrum degeneracy at high symmetric points. (*a*) The 2+1 D space-time lattice structure of the Hamiltonian Eq. 4.6. The bond directions are marked as $\vec{e}_{1,3} = \pm\frac{1}{2}(\hat{x}+\hat{y})$, $\vec{e}_{2,4} = \mp\frac{1}{2}(\hat{x}-\hat{y})$. (*b*) The time-dependent hopping pattern rotates 90° every one quarter period. The bonding strengths $w_{e_i}(t)$ of the *R*, *B*, *G* and *Y* bonds equal 0.2, 3, -3.2, and 0.5, respectively. (*c*) The momentum Brillouin zone with high symmetry points $\Gamma = (0,0)$, $M = (\pm\pi,\pm\pi)$, and $X = (0,\pm\pi)$ and $(\pm\pi,0)$. (*d*) The dispersions along the cuts from Γ to X to M to Γ. Two-fold degeneracies appear at X and M.

the MEBZ shown in Fig. 4.2 (a). The crossing at $\kappa_x = \pi/\lambda$ is protected by the glide time-reflection symmetry giving rise to a pair of Kramers doublet. As a result, the winding number of this loop is $\mathbf{w} = (w_x, w_t) = (2,0)$. If a glide time-reflection symmetry breaking term $\delta V = V_0' \cos(\frac{2\pi}{\lambda}x)$ is added into the crystal potential, the crossing is avoided due to the Kramers symmetry breaking as shown in Fig. 4.2 (b). Consequently, the dispersion splits into two loops, both of which exhibit the winding number $(1,0)$.

4.2.2 2+1 D

Below we show that the space-time group operations protect robust spectrum degeneracies and lead to the Floquet semi-metal state by using a 2+1D example. Consider the case that the space-time little group of the momentum $\mathbf{k}$ contains two non-symmorphic space-time group operations $g_{1,2}$ satisfying

$$g_1 g_2 = T(\mathbf{u}) g_2 g_1, \quad \text{and,} \quad \mathbf{k}\cdot\mathbf{u} = 2\pi p/q, \tag{4.5}$$

where $T(\mathbf{u})$ is a space translation of integer lattice vectors, and p and q coprime. We find that the Bloch-Floquet wavefunctions exhibit a q-fold degeneracy at the momentum-energy vector $\kappa = (\mathbf{k}, \omega)$ proved as follows. Since g_1 belongs to the little group, $\psi_\kappa(\mathbf{r}, t)$ can be chosen to satisfy $M_{g_1}\psi_{\kappa,1} = \mu\psi_{\kappa,1}$, then $\psi_\kappa, M_{g_2}\psi_\kappa, M_{g_2}^2\psi_\kappa, ..., M_{g_2}^{q-1}\psi_\kappa$ are the common Bloch-Floquet eigenstates sharing the same κ but exhibiting a set of different eigenvalues of g_1 as $\eta, \mu\eta, \mu\eta^2, ..., \mu\eta^{q-1}$ with $\eta = e^{i\pi p/q}$. Then they are orthogonal to each other forming a q-fold degeneracy. Compared to the case of non-symmorphic space group protected degeneracy [145, 12, 147], here $g_{1,2}$ are space-time operations for a dynamic space-time crystal.

We employ a 2+1 D tight-binding space-time model as an example to illustrate the above protected degeneracy. A snap shot of the lattice is depicted in Fig. 4.3 (a), which consists of two sublattices: The A-type sites are with integer coordinates (i, j), and each A-site emits four bonds along $\vec{e}_i$ to its four neighboring B sites at $(i \pm \frac{1}{2}, j \pm \frac{1}{2})$. The space-time Hamiltonian within the period T is

$$H(t) = -\sum_{\vec{r}\in A,\ \vec{r}+\frac{a}{2}\vec{e}_i \in B} \left\{ w_{\vec{e}_i}(t) c_{\vec{r}}^\dagger d_{\vec{r}+\frac{a}{2}\vec{e}_i} + h.c., \right\}, \tag{4.6}$$

where a is the distance between two nearest A sites, and $w_{\vec{e}_i}(t)$'s are hopping amplitudes

with different strengths. Their time-dependence is illustrated in Fig. 4.3 (*b*): Within each quarter period, $w_{\vec{e}_i}$ does not vary, and their pattern rotates 90° after every $T/4$. At each given time, the lattice possesses a simple 2D space group symmetry $p2111$, which only includes two-fold rotations around the *AB*-bond centers without reflection and glide-plane symmetries. For example, the rotation R_π around $(\frac{a}{4},\frac{a}{4})$ transforms the coordinate $(x,y,t) \to (\frac{a}{2}+x,\frac{a}{2}+y,t)$. In addition, there exist "time-screw" operations, say, an operation S defined as a rotation around an A-site $(0,0)$ at 90° followed by a time-translation at $T/4$, which transforms $(x,y,t) \to (y,-x,t+\frac{T}{4})$. R_π and S are generators of the space-time group for Eq. 4.6. Since S is a time-screw rotation, this space-time group is non-symmorphic. It is isomorphic to the 3D space-group $I4_1$, while its 2D space subgroup $p2111$ is symmorphic. We have checked that, for a static Hamiltonian taking any of the bond configuration in Fig. 4.3 (*b*), the energy spectra are fully gapped. However, the non-symmorphic space-time group gives rise to spectral degeneracies. Its momentum Brillouin zone is depicted in Fig. 4.3 (*c*). The space-time little group of the M-point (π,π) contains both R and S satisfying $RS = T(a\hat{y})SR = -SR$. Similarly, the X-point $(\pi,0)$ is invariant under both R and S^2 satisfying $RS^2 = T(a\hat{x}+a\hat{y})S^2R = -S^2R$. Hence, the Floquet eigen-energies are doubly degenerate at M and X-points as shown in Fig. 4.3 (*d*), showing a semi-metal structure.

4.3 Space-time group

4.3.1 General descriptions and the classification scheme

We propose the concept of "space-time" group for a full description of the symmetry properties of the $D+1$ dimensional space-time crystal structures. It not only includes space group and magnetic group transformations in the D-spatial dimensions, but also is extended to include operations involving fractional translations along the

time-direction. Since space and time are non-equivalent in the Schrödinger equation, space-time rotations are not allowed except the 2-fold case. For a symmetry operation Γ of the space-time crystal, its operation on $(\mathbf{r},t)$ is defined as,

$$\Gamma(\mathbf{r},t) = (R\mathbf{r}+\mathbf{u}, st+\tau), \tag{4.7}$$

where R is a D-dimensional point group operation, $s=\pm 1$ and $s=-1$ indicates time-reflection, *i.e.*, time-reversal, and $(\mathbf{u},\tau)=\sum_i m_i a^i$ represents a space-time translation with m_i either integers or fractions. At $\tau=0$, Γ is reduced to a space group or magnetic group operation according to $s=\pm 1$, respectively. At $\tau\neq 0$, when $(\mathbf{u},\tau)$ contains fractions of a^i, new symmetry operations arise due to the dynamic nature of the crystal potential, including the "time-screw" rotation and "time-glide" reflection, which are a spatial rotation or a reflection followed by a fractional time translation, respectively. The operation of Γ on the Hamiltonian is defined as $\Gamma^{-1}H(\mathbf{r},t)\Gamma = H(\Gamma(\mathbf{r},t))$, or, $\Gamma^{-1}H(\mathbf{r},t)\Gamma = H^*(\Gamma(\mathbf{r},t))$ for $s=\pm 1$, respectively. Correspondingly, the transformation M_Γ on the Bloch-Floquet wavefunctions $\psi_\kappa(\mathbf{r},t)$ is $M_\Gamma\psi_\kappa = \psi_\kappa(\Gamma^{-1}(\mathbf{r},t))$, or, $\psi^*_\kappa(\Gamma^{-1}(\mathbf{r},t))$ for $s=\pm 1$, respectively.

The space-time groups in $d+1$ dimensions $G(d,1)$ are discrete subgroups of the Euclidean group $E_d \otimes E_1$. Each space-time group is constructed from a Bravais lattice M constituted of $d+1$ space-time mixing discrete translations, and a magnetic point groups (MPG) in d dimensions $G_m(d)$ that leaves M invariant. The hierarchal classification scheme of the space-time groups starts with crystal systems, which are labeled by a set of Bravais lattices $\{M\}$ sharing the same magnetic point group symmetry and a set of MPGs $\{G_m\}$ that only leaves Bravais lattices in $\{M\}$ invariant. One crystal system contains all the space-time groups constructed from Bravais lattices in $\{M\}$ and MPGs in $\{G_m\}$. Each crystal system contains several geometry crystal classes (GCC). Space-time groups

belong to the same GCC if they are constructed from the same MPG. Each GCC can be further classified into different arithmetic crystal classes (ACC). Each ACC contains all the space-time groups constructed from the same Bravais lattice and the same MPG. It is worth noting that, in some cases, the ACC also depends on the relative orientation between the Bravais lattice and the MPG. Such hierarchy is in parallel to the conventional classification scheme[148].

Given an ACC labeled by M and G_m, the classification of all the space-time groups can be done using group cohomology theory, similar to the classification of the space groups [149]. A space-time group G is the group extension of an abelian discrete translation group of M by the magnetic point group G_m, described by the following exact sequence,

$$1 \to M \to G \to G_m \to 1 \tag{4.8}$$

Such group extension can be constructed by associating each element g in $G_m(d)$ a fractional translation $c(g) \in T(d+1)/M$, where $T(d+1)$ is the group of continuous translations in $d+1$ dimensions. The map c needs to satisfy

$$c(1) = 0, \;\; c(g_1 g_2) = c(g_1) + g_1 c(g_2), \tag{4.9}$$

so that the elements $(c(g), g)$ form a group. In order to classify all the space-time groups within the ACC, a key observation is that all maps c's themselves form an abelian group. Given two distinct assignments c_1 and c_2, one can check that their product $c_1 \cdot c_2$, defined as,

$$c_1 \cdot c_2(g) = c_1(g) + c_2(g) \tag{4.10}$$

satisfies Eq. 4.9 as well. This group is denoted as $Z^1(G_m, T/M)$. However, not all the elements in $Z^1(G_m, T/M)$ are corresponding to distinct types of space-time groups.

Without specifying the equivalence relations, the group $Z^1(G_m, T/M)$ is not finite. An obvious condition is that space groups that related by origin shifting are of the same type. This is to say that the map with the following form,

$$c_u(g) = gu - u \tag{4.11}$$

for any origin shifting vector $u \in T/M$, should be identified with the trivial map $c(g) = 0$. The map with the structure in Eq. 4.11 also form a group $B^1(G_m, T/M)$. We are interested in the quotient group $Z^1(G_m, T/M)/B^1(G_m, T/M)$, which is the one-dimensional cohomology group of G_m with coefficients in T/M, denoted as $H^1(G_m, T/M)$.

Each element of $H^1(G_m, T/M)$ is corresponding to a type of space-time groups. Since $H^1(G_m, T/M)$ is finite, we have a finite list of space-time groups within the ACC. The trivial element of $H^1(G_m, T/M)$ is that $c(g) = 1$ for all g in the MPG, and the corresponding space-time group is the semi-direct product of the Bravais lattice M and the MPG $G_m(d)$, called symmorphic space-time group. Each ACC only contains one symmorphic space-time group. The other elements in $H^1(G_m, T/M)$ are corresponding to the nonsymmorphic space-time groups in which there is not a single site that the whole symmetry group G_m can be realized.

However, not all the elements of the cohomology group $H^1(G_m, T/M)$ lead to distinct type of the space-time groups neither. For example, two elements in $H^1(G_m, T/M)$ related by global rotation should be identified. Here we invoke the second equivalence relation, which generalizes the one used in classifying space group. All elements in $H^1(G_m, T/M)$ related by linear transformations ρ are identified, where ρ leaves *all* the MPGs within the given crystal system unchanged. According to the definition, the second equivalent relation depending on the crystal system that contains the ACC.

4.3.2 Classification in 1+1 dimensions

As a concrete example, we present a complete classification of the space-time groups for 1+1 D space-time crystal structures. Due to the non-equivalence between spatial and temporal directions, there are no square and hexagonal space-time crystal systems. The point-group like operations are isomorphic to D_2, including reflection m_x, time reversal m_t, and their combination $m_x m_t$, *i.e.*, the 2-fold space-time rotation. Consequently, only two space-time crystal systems are allowed – oblique and orthorhombic. In addition to g_t, symmetries involving fractional translations also include the "time glide reflection" g_x - spatial reflection followed by a fractional time-translation. The space-time crystal structures marked with m_x and m_t, or those with g_x and g_t, should be different, respectively.

The above 1+1 D space-time symmetries give rise to 13 space-time groups in contrast to the 17 wallpaper space groups characterizing the 2D static lattices. The oblique Bravais lattice is simply monoclinic, while the orthorhombic ones include both the primitive and centered Bravais lattices. The monoclinic lattice gives rise to two different crystal structures with and without the 2-fold space-time axes, whose space-time groups are denoted by $P_{1,2}$, respectively, as shown in Fig. 4.4 (a). For the primitive orthorhombic lattices, the associated crystal structures can exhibit the point-group symmetries m_x and m_t, and the space-time symmetries g_t and g_x. Their combinations give rise to crystal structures with 8 space-time group symmetries denoted as Pm_x, Pm_t, $P2m_x m_t$, Pg_x, Pg_t, $P2g_x g_t$, $P2m_x g_t$, $P2g_x m_t$, respectively, as shown in Fig. 4.4 (b). Four of them possess the 2-fold space-time axes as indicated by "2" in their symbols. For the centered orthorhombic Bravais lattices, 3 crystal structures exist with space-time groups denoted as Cm_x, Cm_y, and $C2m_x m_t$, respectively, as shown in Fig. 4.4 (c). They all exhibit glide-reflection symmetries, and the last one possesses the 2-fold space-time axes as well. Two unit cells are plotted for the centered lattices to show the full symmetries explicitly,

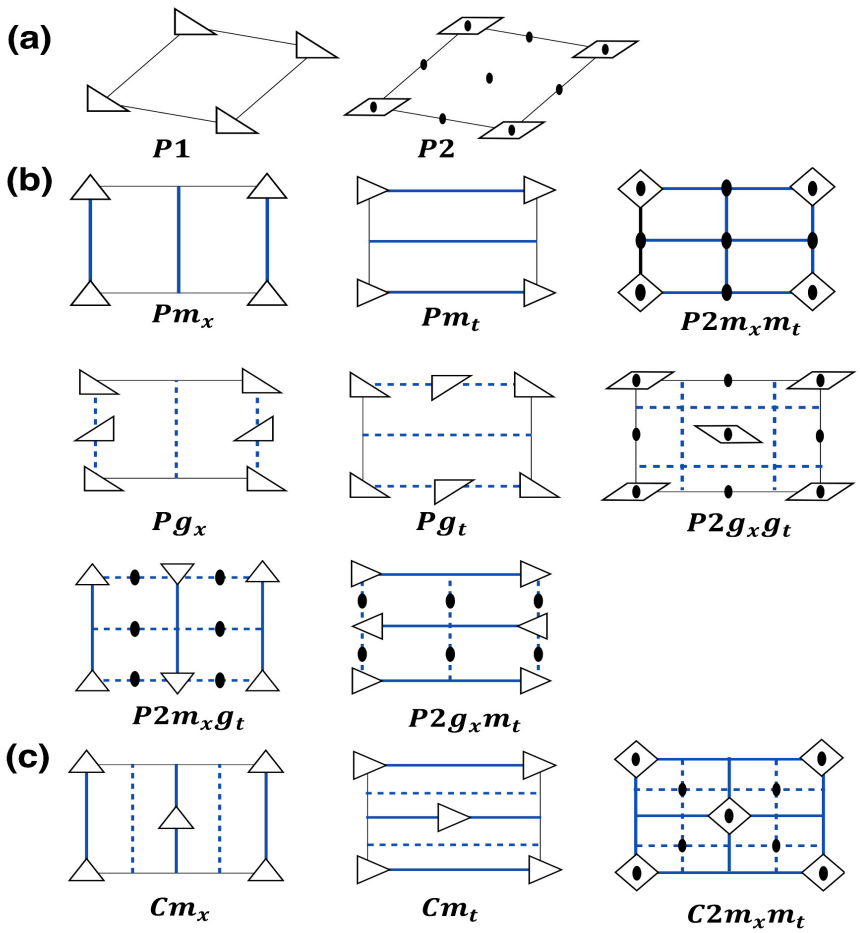

Figure 4.4: The classification of 13 space-time groups in 1+1D and the associated lattice configurations. The solid oval marks the 2-fold space-time axis, and the parallelogram means the 2-fold axis without reflection symmetries. The thick solid and dashed lines represent reflection and glide-reflection axes, respectively. Configurations of triangles and the diamond denote the local symmetries under reflections. (*a*) The oblique lattices with and without 2-fold axes. Their basis vectors are generally space-time mixed. The primitive (*b*) and centered (*c*) orthorhombic lattices: According to their reflection and glide reflection symmetries, they are classified to 8 groups in (*b*), and 3 groups in (*c*).

and their primitive basis vectors are actually space-time mixed.

4.3.3 Classification of 2+1D space-time groups

Table 4.1: The magnetic point groups in 2 dimensions and their relations to the usual 10 2-dimensional point groups. In the third column, the symmetry generator for each MGP is listed. The symmetry operation m_t stands for the time reversal, R_θ represents rotation in the $x-y$ plane through the angle θ, m_x is the reflection in the x direction and m_y is the reflection along the y direction.

Point Group	$G_m(2)$	Generators
C_1	1	
	$11'$	m_t
C_2	2	R_π
	$21'$	R_π, m_t
	$2'$	$R_\pi m_t$
C_3	3	$R_{2\pi/3}$
	$31'$	$R_{2\pi/3}, m_t$
C_4	4	$R_{\pi/2}$
	$41'$	$R_{\pi/2}, m_t$
	$4'$	$R_{\pi/2} m_t$
C_6	6	$R_{\pi/3}$
	$61'$	$R_{\pi/3}, m_t$
	$6'$	$R_{\pi/3} m_t$

Point Group	$G_m(2)$	Generators
D_1	m	m_x
	$m1'$	m_x, m_t
	m'	$m_x m_t$
D_2	$mm2$	m_x, m_y
	$mm21'$	m_x, m_y, m_t
	$m'm2'$	$m_x m_t, m_y$
	$m'm'2$	$m_x m_t, m_y m_t$
D_3	$3m$	$R_{2\pi/3}, m_x$
	$3m1'$	$R_{2\pi/3}, m_x, m_t$
	$3m'$	$R_{2\pi/3}, m_x m_t$
D_4	$4mm$	$R_{\pi/2}, m_x$
	$4mm1'$	$R_{\pi/2}, m_x, m_t$
	$4'm'm$	$R_{\pi/2} m_t, m_x$
	$4m'm'$	$R_{\pi/2}, m_x m_t$
D_6	$6mm$	$R_{\pi/3}, m_x$
	$6mm1'$	$R_{\pi/3}, m_x, m_t$
	$6'm'm$	$R_{\pi/3} m_t, m_x$
	$6m'm'$	$R_{\pi/3}, m_x m_t$

In this section, we focus on the case of $d = 2$. The case of $d = 3$ is left for future study. In 2 dimensions, the conventional 10 crystallographic point groups, combining with the time reversal symmetry, can be enriched to 31 MPGs listed in Table. 4.1. By combining the MPGs with three independent discrete translations in $T(3)$, we obtain 7 crystal systems, 14 Bravais lattices and 275 space-time groups. The relation between

Table 4.2: Summary of the space-group classification in 2+1 dimensions. There are 7 space-time crystal systems and 14 space-time Bravais lattices (The primitive trigonal lattice is the same as the primitive hexagonal lattice). The 31 magnetic point groups are uniquely assigned to the 7 crystal systems, as listed in the third column. In the fourth and fifth column, we list the number of arithmetical crystal classes and the space-time groups within each Bravais lattice.

Crystal System	Bravais Lattice	MP Group	ACC	$G(2,1)$
Triclinic	Primitive	$1, 2'$	2	2
T-Monoclinic	Primitive	$11', 2, 21'$	3	8
	Centered		3	5
R-Monoclinic	Primitive	$m, m', m'm2'$	3	8
	Centered		3	5
Orthorhombic	Primitive	$mm2, m'm'2$ $mm21', m1'$	4	68
	T-Base-Centered		4	15
	R-Base-Centered		5	22
	Face-Centered		4	7
	Body-Centered		4	15
Tetragonal	Primitive	$4, 41', 4'$ $4mm, 4mm1'$ $4'm'm, 4m'm'$	8	49
	Body-Centered		8	19
Trigonal	Primitive	$3, 6', 3m$ $3m', 6'm'm$	8	18
	Rhombohedral		5	7
Hexagonal	Primitive	$6, 61', 31'$ $6mm, 6m'm'$ $6mm1', 3m1'$	8	27

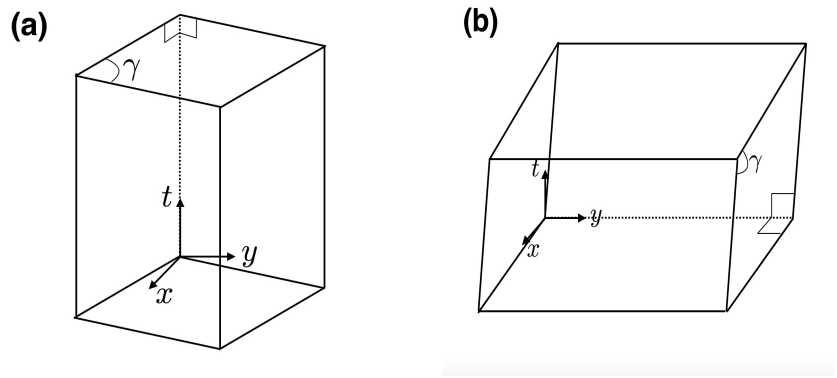

Figure 4.5: The two kinds of monoclinic crystal systems in the space-time group classification. (a) The t-monoclinic lattice. One lattice basis vector is along the temporal direction and perpendicular to the other two basis vectors which are not orthogonal. The angle γ is not $\pi/2$. The maximal MPG is $21'$. (b) The r-monoclinic lattice. One lattice basis vector is along purely spatial direction and perpendicular to the other two basis vectors which are not orthogonal. The maximal MPG is $m'm2$.

space-time crystal systems, MPGs, Bravais lattices and space-time lattices are summarized in Table 4.2. We adopt the terminology mostly from 3D crystallography [150] when it is possible.

Before going into the details of each space-time group, we emphasize that the classification of the space-time group $G(2,1)$ is different from the usual space group $G(3)$ [150]. The differences already appear on the level of crystal systems. The familiar cubic crystal system from space group classification is absent in 2+1 D, because its symmetry operation necessarily involves four-fold space-time rotation, which is not an isometry in $E_2 \otimes E_1$. On the other hand, there are two crystal systems, r-monoclinic and t-monoclinic, respectively, corresponding to the 3D monoclinic crystal system. The primitive unit cell of the two lattice are plotted in Fig. 4.5. The maximal MPG of the two crystal systems are inequivalent. The first case is $21'$, generated by spatial rotation R_π and time reversal m_t, while the second case is $m'm2$ generated by $m_y m_t, m_x$. The space-time crystals in each crystal system are further classified according to their Bravais lattices. The main difference from the 3D cases occurs in the orthogonal space-time crystal systems, which

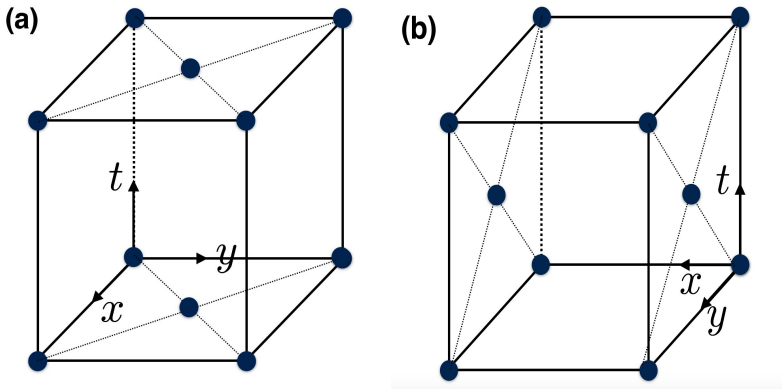

Figure 4.6: The two kinds of base-centered Bravais lattices in the space-time orthorhombic crystal system. (a) The t-base-centered lattice. The additional point is at the center of the spatial face. (b) The r-base-centered lattice. The additional point is at the center of the face containing temporal axis.

contains 5 Bravais lattices rather than 4 in its static counterpart. As illustrated in Fig. 4.6, there are two base-centered lattices. In the t-base-centered lattice, the additional point locates at the center of the face in the $x-y$ plane, while the additional point in r-base-centered lattice is at the center of the face in the $y-t$ plane.

In the following, we will discuss the space-time group classification of each crystal system in detail and enumerate all the space-time groups $G(2,1)$.

4.3.4 Triclinic Crystal System

The triclinic crystal system contains the simplest space-time lattice. There is no constraint on the 3 lattice basis vectors $a_1 \sim a_3$ and thus only Bravais lattice is involved in this crystal system. The maximal symmetry of the lattices in this crystal system is described by the MGP $2'$, generated by the space-time inversion $R_\pi m_t$. There are two MGPs assigned to crystal system, the trivial one 1 and the MPG $2'$. The combination of each of two MPGs and the primitive lattice leads to two ACCs. Both of the first cohomology groups of two ACCs are identities, indicating that there is no non-trivial group extension of the primitive triclinic lattice by MPGs. In consequence, each ACC

only contains one type of space-time group, and there is no nonsymmorphic space-time group in the triclinic crystal system. Physically, the combination of $R_\pi m_t$ with any translations is also space-time inversion but with a shifted origin. The two types of space-time groups are listed in Table. 4.3.

Table 4.3: Space-time groups in 2+1 dimensions for oblique lattices.

Primitive Triclinic		
ACC NO. 1: $1P$ $G_m(2)=1, \quad H^1(1,T(3)/P)=\mathbb{I}$		
$P1$		1
ACC NO. 2: $2'P$ $G_m(2)=2', \quad H^1(2',T(3)/P)=\mathbb{I}$		
$P\bar{1}$	$R_\pi m_t$	1

4.3.5 T-Monoclinic and R-Monoclinic Crystal Systems

Before classifying the space-time groups in the monoclinic crystal systems, we briefly review the conventional monoclinic lattice here. In 3 dimensions, the monoclinic lattice has a unique direction that either is a twofold rotation axis or perpendicular to a mirror plane. There are two kinds of Bravais lattices. The first is the primitive monoclinic, hosting 8 space groups. The second is the base-centered monoclinic with an addition point at the center of the face parallel to the unique direction. There are 5 space groups in the base-centered monoclinic lattice.

In the dynamic space-time lattices considered here, however, there are two types of monoclinic lattices. This arises from the speciality of the time direction, which requires that the unique direction in the monoclinic lattice is either purely temporal or purely spatial, corresponding to the t-monoclinic crystal system and the r-monoclinic crystal system, respectively. Each of them contains two Bravais lattices and 13 space-time groups.

In the t-monoclinic crystal system, the unique direction coincides with the temporal direction. The maximal symmetry of a general t-monoclinic lattice is described by the MGP $21'$ generated by the spatial two-fold rotation R_π and time reversal m_t. Three MGP, 2, $11'$ and $21'$, are assigned to this crystal system, and therefore the t-monoclinic crystal system contains three GCCs. Although the MPG $2'$ also leave the lattices in this crystal system invariant, it also acts on the triclinic lattices with lower symmetry and thus is excluded here.

The primitive lattice basis vectors are

$$\begin{aligned} a_1^P &= (x_1, y_1, 0) \\ a_2^P &= (x_2, y_2, 0) \\ a_3^P &= (0, 0, t_0). \end{aligned} \tag{4.12}$$

Among the three vectors, a_1 and a_2 generally mix space and time, while a_3 is purely temporal. The combination of the three MGPs and the primitive Bravais lattice leads to three ACCs. Unlike the 2 ACCs in the triclinic crystal system, here we have nontrivial group extension of the lattice by the MGPs, and each ACC contains more than one space-time group. For example, let us look at the ACC No. 3 $2P$ and consider the interplay between the MGP 2 ($\{I, R_\pi\}$) and the translations in Eq. 4.12. There are two space-time groups $P112$ and $P112_1$ in this arithmetic crystal class. The space-time group $P112$ is the semi-direct product of the MGP and the lattice described by Eq. 4.12. The space-time group $P112_1$ extends $P112$ by replacing the 2-fold rotational symmetry R_π with the 2-fold time-screw rotational symmetry $R_\pi T_t^{1/2}$. The space-time group is nonsymmorphic because $R_\pi T_t^{1/2}$ does not fix any space-time coordinate. Mathematically, the first cohomology group of the ACC $2P$ is isomorphic to $\mathbb{Z}_2$ with the following

generator,

$$c_1^{(3)}(R_\pi) = \frac{1}{2}a_3^P \tag{4.13}$$

where the superscript of c stands for the ACC id and the subscript of c labels the generator of the cohomology group. This result indicates that there are two space-time groups within the ACC $2P$.

On the other hand, $H^1(11', T(3)/P)$ is $\mathbb{Z}_2^2$ with the generators,

$$\begin{aligned} c_1^{(4)}(m_t) &= \frac{1}{2}a_1^P \\ c_2^{(4)}(m_t) &= \frac{1}{2}a_2^P \end{aligned} \tag{4.14}$$

There are four elements in this cohomology group, in principle corresponding to four types of space-time groups. However, it turns out that c_1, c_2 and $c_1 \cdot c_2$ can be related each other under the second equivalence relation, and there are only two distinct types of space-time groups. Physically, the symmetry operation of the time reversal with gliding along a_1^P, a_2^P and $a_1^P + a_2^P$ are identified. For the ACC $21'P$, the first cohomology group is $\mathbb{Z}_2^3$, and the three generators are

$$\begin{aligned} &c_1^{(5)}(R_\pi) = a_3^P/2,\ c_1^{(5)}(m_t) = 0 \\ &c_2^{(5)}(R_\pi) = 0,\ c_1^{(5)}(m_t) = \frac{1}{2}a_1^P \\ &c_3^{(5)}(R_\pi) = 0,\ c_3^{(5)}(m_t) = \frac{1}{2}a_2^P \end{aligned} \tag{4.15}$$

There are eight group elements, but only four of them are inequivalent due to the similar reason as before. The total 8 types of the space-time groups within the primitive monoclinic lattice is listed in Table. 4.4.

Table 4.4: Space-time groups in 2+1 dimensions for primitive t-monoclinic lattices. The action of the glide refection g_t on the coordinate is $g_t(x,y,t) = (x,y,-t) + a_1^p/2$, and $T_t^{1/n}$ is the temporal fractional translation so that $T_t^{1/n}(x,y,t) = (x,y,t) + a_3^p/n$, where $a_1^p \sim a_3^p$ are the primitive lattice basis for the t-monoclinic crystal system defined in Eq. 4.12.

Primitive T-Monoclinic		
ACC NO. 3: $2P$, $G_m(2) = 2, \quad H^1(2, T(3)/P) = \mathbb{Z}_2$		
$P112$	R_π	1
$P112_1$	$R_\pi T_t^{1/2}$	c_1
ACC NO. 4: $11'P$, $G_m(2) = 11', \quad H^1(11', T(3)/P) = \mathbb{Z}_2^2$		
$P11m$	m_t	1
$P11c$	g_t	c_1
ACC NO. 5: $21'P$, $G_m(2) = 21', \quad H^1(21', T(3)/P) = \mathbb{Z}_2^3$		
$P112/m$	R_π, m_t	1
$P112_1/m$	$R_\pi T_t^{1/2}, m_t$	c_1
$P112/c$	R_π, g_t	c_2
$P112_1/c$	$R_\pi T_t^{1/2}, g_t$	$c_1 \cdot c_2$

For the base-centered Bravais lattice, $a_1 \sim a_3$ are

$$\begin{aligned} a_1^B &= (x_1, y_1, 0) \\ a_2^B &= (x_2, y_2, 0) \\ a_3^B &= \frac{1}{2}(x_1, y_1, t_0). \end{aligned} \tag{4.16}$$

Combining the Bravais lattice with the same set of MPGs leads to 3 ACCs but 5 space-time groups listed in Table. 4.5. The key difference between the base-centered Bravais lattice and the primitive one is that, in the formal case, the combination of space-time inversion R_π with temporal translation of $a_3^P/2$ is equivalent to the usual space-time reflection with a shifted origin. As a result, the first cohomology group of the ACC $2C$ is trivial and that of the ACC $21'C$ downgrades to $\mathbb{Z}_2^2$, resulting in fewer types of space-time groups in these two ACCs, while the case of the ACC $11'C$ is unchanged from

the primitive one. The 5 types of space-time groups are listed in Table. 4.5.

Table 4.5: Space-times group in 2+1 dimensions for base-centered t-monoclinic lattices. The action of the glide refection g_t on the coordinate is $g_t(x,y,t) = (x,y,-t) + a_1^P/2$, where $a_1^p \sim a_3^p$ are the primitive lattice basis for the t-monoclinic crystal system defined in Eq. 4.12.

Base-Centered T-Monoclinic		
ACC NO. 6: $2C$, $G_m(2) = 2, \quad H^1(2, T(3)/C) = \mathbb{I}$		
$C112$	R_π	1
ACC NO. 7: $11'C$, $G_m(2) = 11', \quad H^1(11', T(3)/C) = \mathbb{Z}_2^2$		
$C11m$	m_t	1
$C11c$	g_t	c_1
ACC NO. 8: $21'C$, $G_m(2) = 21', \quad H^1(21', T(3)/C) = \mathbb{Z}_2^2$		
$C112/m$	R_π, m_t	1
$C112/c$	R_π, g_t	c_1

As to the r-monoclinic crystal system, the unique direction is purely spatial, taken to be the x axis. Two symmetry operations m_x and $m_y m_t$ leave the lattice invariant and generates the maximal MGP $m'm2$. As a result, three MGPs, m', m and $m'm2$, are assigned to this crystal system. This crystal system also has two Bravais lattices. The lattice basis for the primitive one is

$$\begin{aligned} a_1^P &= (0, y_1, t_1) \\ a_2^P &= (0, y_2, t_2) \\ a_3^P &= (x_0, 0, 0), \end{aligned} \tag{4.17}$$

and the basis for the based-centered one is

$$\begin{aligned} a_1^B &= (0, y_1, t_1) \\ a_2^B &= (0, y_2, t_2) \\ a_3^B &= \frac{1}{2}(x_0, y_1, t_2). \end{aligned} \tag{4.18}$$

The classification of the space-time groups for the r-monoclinic crystal system is completely in parallel with the t-monoclinic crystal system, and is not repeated here. The resulting 6 ACCs, the corresponding cohomology groups and 15 distinct types of space-time groups are listed in Table. 4.6 for the primitive lattice and Table. 4.7 for the centered lattice.

Table 4.6: Space-time groups in 2+1 dimensions for the primitive r-monoclinic crystal system. The action of the glide refection g_x on the coordinate is $g_x(x,y,t) = (-x,y,t) + a_1^p/2$, and $T_x^{1/n}$ is the spatial fractional translation so that $T_x^{1/n}(x,y,t) = (x,y,t) + a_3^p/n$, where $a_1^p \sim a_3^p$ are the primitive lattice lattice basis for r-monoclinic crystal system defined in Eq. 4.17.

Primitive R-Monoclinic		
ACC NO. 9: $m'P$, $G_m(2) = m'$, $H^1(m', T(3)/P) = \mathbb{Z}_2$		
$P211$	$m_y m_t$	1
$P2_111$	$m_y m_t T_x^{1/2}$	c_1
ACC NO. 10: mP, $G_m(2) = m$, $H^1(m, T(3)/P) = \mathbb{Z}_2^2$		
$Pm11$	m_x	1
$Pc11$	g_x	c_1
ACC NO. 11: $m'm2'P$, $G_m(2) = m'm2'$, $H^1(m'm2', T(3)/P) = \mathbb{Z}_2^3$		
$P2/m11$	$m_x, m_y m_t$	1
$P2_1/m11$	$m_x, m_y m_t T_x^{1/2}$	c_1
$P2/c11$	$g_x, m_y m_t$	c_2
$P2_1/c11$	$g_x, m_y m_t T_x^{1/2}$	$c_1 \cdot c_2$

4.3.6 Orthorhombic Crystal System

The space-time orthorhombic crystal system has at least two reflection/glide planes, and therefore requires three mutually orthogonal primitive lattice basis vectors. The fact that the space-time group is subgroup of $E_2 \otimes E_1$ requires that one of the three axises is purely temporal. The relevant symmetries are three reflections, m_x, m_y and m_t. The maximal symmetry of a general lattice within this crystal system is described by

Table 4.7: Space-time groups in 2+1 dimensions for base-centered r-monoclinic lattices. The action of the glide refection g_x on the coordinate is $g_x(x,y,t) = (-x,y,t) + a_1^p/2$, where $a_1^p \sim a_3^p$ are the primitive lattice lattice basis for r-monoclinic crystal system defined in Eq. 4.17.

Base-Centered R-Monoclinic		
ACC NO. 12: $m'C$, $G_m(2) = m'$, $H^1(m', T(3)/C) = \mathbb{I}$		
$C211$	$m_y m_t$	1
ACC NO. 13: mC, $G_m(2) = m$, $H^1(m, T(3)/C) = \mathbb{Z}_2^2$		
$Cm11$	m_x	1
$Cc11$	g_x	c_1
ACC NO. 14: $m'm2'C$, $G_m(2) = m'm2'$, $H^1(m'm2'C, T(3)/C) = \mathbb{Z}_2^2$		
$C2/m11$	$m_x, m_y m_t$	1
$C2/c11$	$g_x, m_y m_t$	c_1

the MPG $mm21'$. Four MGPs, $m'm'2$, $mm2$, $m1'$ and $mm21'$, are assigned to this crystal system. In order to preserve all the MPGs, the linear map ρ in the second equivalence relation is restricted in the $x-y$ plane.

The lattice basis vectors of the primitive Bravais lattice are along the three orthogonal axises,

$$\begin{aligned} a_1^P &= (x_0, 0, 0) \\ a_2^P &= (0, y_0, 0) \\ a_3^P &= (0, 0, t_0) \end{aligned} \tag{4.19}$$

The combination of the Bravais lattice and the 4 MPGs leads to 4 ACCs and 68 distinct space-time groups listed in Table. 4.8 and Table. 4.10.

The first cohomology group of the ACC $m'm'2P$ is $\mathbb{Z}_2^3$ with the following 3 generators,

$$\begin{aligned} c_1^{(15)}(m_x m_t) &= \frac{1}{2} a_3^P, \quad c_1^{(15)}(m_y m_t) = 0 \\ c_2^{(15)}(m_x m_t) &= \frac{1}{2} a_2^P, \quad c_2^{(15)}(m_y m_t) = 0 \\ c_3^{(15)}(m_x m_t) &= 0, \qquad c_3^{(15)}(m_y m_t) = \frac{1}{2} a_1^P \end{aligned} \tag{4.20}$$

Table 4.8: Space-time groups in 2+1 dimensions for primitive orthorhombic lattice (1). The fractional translation $T^{1/n}_{x,y,z}$ acting on the coordinate as $T^{1/n}_{x,y,z}(x,y,z) = (x,y,z) + a^P_{1,2,3}/n$, where $a^P_1 \sim a^P_3$ are the primitive lattice basis for space-time orthorhombic crystal system defined in Eq. 4.19.

Primitive Orthorhombic (1)		
ACC No.15 : $m'm'2P$, $G_m(2)$: $m'm'2$, $H^1(m'm'2, T(3)/P) = \mathbb{Z}_2^3$		
$P222$	$m_y m_t, m_x m_t$	1
$P222_1$	$m_y m_t, m_x m_t T_t^{1/2}$	c_1
$P2_122$	$m_y m_t T_x^{1/2}, m_x m_t$	c_2
$P2_12_12$	$m_y m_t T_x^{1/2}, m_x m_t T_y^{1/2}$	$c_2 \cdot c_3$
$P2_122_1$	$m_y m_t T_x^{1/2}, m_x m_t T_t^{1/2}$	$c_1 \cdot c_2$
$P2_12_12_1$	$m_y m_t T_x^{1/2}, m_x m_t T_y^{1/2} T_t^{1/2}$	$c_1 \cdot c_2 \cdot c_3$
ACC No.16 : $mm2P$, $G_m(2)$: $mm2$, $H^1(mm2, T(3)/P) = \mathbb{Z}_2^4$		
$Pmm2$	m_x, m_y	1
$Pmc2_1$	$m_x, m_y T_t^{1/2}$	c_3
$Pma2$	$m_x, m_y T_x^{1/2}$	c_4
$Pcc2$	$m_x T_t^{1/2}, m_y T_t^{1/2}$	$c_2 \cdot c_3$
$Pca2_1$	$m_x T_t^{1/2}, m_y T_x^{1/2}$	$c_2 \cdot c_4$
$Pmn2_1$	$m_x, m_y T_x^{1/2} T_t^{1/2}$	$c_3 \cdot c_4$
$Pba2$	$m_x T_y^{1/2}, m_y T_x^{1/2}$	$c_1 \cdot c_4$
$Pnc2$	$m_x T_y^{1/2} T_t^{1/2}, m_y T_t^{1/2}$	$c_1 \cdot c_2 \cdot c_3$
$Pna2_1$	$m_x T_y^{1/2} T_t^{1/2}, m_y T_x^{1/2}$	$c_1 \cdot c_2 \cdot c_4$
$Pnn2$	$m_x T_y^{1/2} T_t^{1/2}, m_y T_x^{1/2} T_t^{1/2}$	$\prod_{i=1}^{4} c_i$
ACC No.17 : $m1'P$, $G_m(2)$: $m1'$, $H^1(m1', T(3)/P) = \mathbb{Z}_2^4$		
$P2mm$	m_y, m_t	1
$P2_1ma$	$m_y, m_t T_x^{1/2}$	c_1
$P2_1am$	$m_y T_x^{1/2}, m_t$	c_2
$P2mb$	$m_y, m_t T_y^{1/2}$	c_3
$P2cm$	$m_y T_t^{1/2}, m_t$	c_4
$P2aa$	$m_y T_x^{1/2}, m_t T_x^{1/2}$	$c_1 \cdot c_2$
$P2_1ab$	$m_y T_x^{1/2}, m_t T_y^{1/2}$	$c_2 \cdot c_3$
$P2_1ca$	$m_y T_t^{1/2}, m_t T_x^{1/2}$	$c_1 \cdot c_4$
$P2_1mn$	$m_y, m_t T_x^{1/2} T_y^{1/2}$	$c_1 \cdot c_3$
$P2_1nm$	$m_y T_x^{1/2} T_t^{1/2}, m_t$	$c_2 \cdot c_4$
$P2cb$	$m_y T_t^{1/2}, m_t T_y^{1/2}$	$c_3 \cdot c_4$

Table 4.9: Space-time groups in 2+1 dimensions for primitive orthorhombic lattice (2).

Primitive Orthorhombic (2)		
ACC No.17 (cont.): $m1'P$, $G_m(2)$: $m1'$, $H^1(m1',T(3)/P)=\mathbb{Z}_2^4$		
$P2na$	$m_y T_x^{1/2} T_t^{1/2}, m_t T_x^{1/2}$	$c_1\cdot c_2\cdot c_4$
$P2an$	$m_y T_x^{1/2}, m_t T_x^{1/2} T_y^{1/2}$	$c_1\cdot c_2\cdot c_3$
$P2_1nb$	$m_y T_x^{1/2} T_t^{1/2}, m_t T_y^{1/2}$	$c_2\cdot c_3\cdot c_4$
$P2_1cn$	$m_y T_t^{1/2}, m_t T_x^{1/2} T_y^{1/2}$	$c_1\cdot c_3\cdot c_4$
$P2nn$	$m_y T_x^{1/2} T_t^{1/2}, m_t T_x^{1/2} T_y^{1/2}$	$\prod_{i=1}^{4} c_i$
ACC No.18: $mm21'P$, $G_m(2)$: $mm21'$, $H^1(mm21',T(3)/P)=\mathbb{Z}_2^6$		
$Pmmm$	m_x, m_y, m_t	1
$Pmma$	$m_x, m_y, m_t T_x^{1/2}$	c_5
$Pbmm$	$m_x T_y^{1/2}, m_y, m_t$	c_1
$Pcmm$	$m_x T_t^{1/2}, m_y, m_t$	c_2
$Pbam$	$m_x T_y^{1/2}, m_y T_x^{1/2}, m_t$	$c_2\cdot c_4$
$Pmcb$	$m_x, m_y T_t^{1/2}, m_t T_y^{1/2}$	$c_3\cdot c_6$
$Pccm$	$m_x T_t^{1/2}, m_y T_t^{1/2}, m_t$	$c_2\cdot c_3$
$Pmaa$	$m_x, m_y T_x^{1/2}, m_t T_x^{1/2}$	$c_4\cdot c_5$
$Pbcm$	$m_x T_y^{1/2}, m_y T_t^{1/2}, m_t$	$c_1\cdot c_2$
$Pmca$	$m_x, m_y T_t^{1/2}, m_t T_x^{1/2}$	$c_3\cdot c_5$
$Pmab$	$m_x, m_y T_x^{1/2}, m_t T_b^{1/2}$	$c_4\cdot c_6$
$Pmmn$	$m_x, m_y, m_t T_x^{1/2} T_y^{1/2}$	$c_5\cdot c_6$
$Pnmm$	$m_x T_y^{1/2} T_t^{1/2}, m_y, m_t$	$c_1\cdot c_2$

Table 4.10: Space-time groups in 2+1 dimensions for primitive orthorhombic lattice (3).

Primitive Orthorhombic (3)		
ACC No.18 (cont.): $mm21'P$, $G_m(2)$: $mm21'$, $H^1(mm21', T(3)/P) = \mathbb{Z}_2^6$		
Pmna	$m_x, m_y T_x^{1/2} T_t^{1/2}, m_t T_x^{1/2}$	$c_3 \cdot c_4 \cdot c_5$
Pbmn	$m_x T_y^{1/2}, m_y, m_t T_x^{1/2} T_y^{1/2}$	$c_1 \cdot c_5 \cdot c_6$
Pncm	$m_x T_y^{1/2} T_t^{1/2}, m_y T_t^{1/2}, m_t$	$c_1 \cdot c_2 \cdot c_3$
Pcca	$m_x T_t^{1/2}, m_y T_t^{1/2}, m_t T_x^{1/2}$	$c_2 \cdot c_3 \cdot c_5$
Pbaa	$m_x T_y^{1/2}, m_y T_x^{1/2}, m_t T_x^{1/2}$	$c_2 \cdot c_4 \cdot c_5$
Pbcb	$m_x T_y^{1/2}, m_y T_t^{1/2}, m_t T_y^{1/2}$	$c_2 \cdot c_3 \cdot c_6$
Pbca	$m_x T_y^{1/2}, m_y T_t^{1/2}, m_t T_x^{1/2}$	$c_1 \cdot c_3 \cdot c_5$
Pnma	$m_x T_y^{1/2} T_t^{1/2}, m_y, m_t T_x^{1/2}$	$c_1 \cdot c_2 \cdot c_5$
Pbnm	$m_x T_y^{1/2}, m_y T_x^{1/2} T_t^{1/2}, m_t$	$c_1 \cdot c_3 \cdot c_4$
Pmcn	$m_x, m_y T_t^{1/2}, m_t T_x^{1/2} T_y^{1/2}$	$c_3 \cdot c_5 \cdot c_6$
Pban	$m_x T_y^{1/2}, m_y T_x^{1/2}, m_t T_x^{1/2} T_y^{1/2}$	$c_1 \cdot c_4 \cdot c_5$
Pncb	$m_x T_x^{1/2} T_y^{1/2}, m_y T_t^{1/2}, m_t T_y^{1/2}$	$c_1 \cdot c_2 \cdot c_3 \cdot c_6$
Pccn	$m_x T_t^{1/2}, m_y T_t^{1/2}, m_t T_x^{1/2} T_y^{1/2}$	$c_2 \cdot c_3 \cdot c_5 \cdot c_6$
Pnaa	$m_x T_y^{1/2} T_t^{1/2}, m_y T_x^{1/2}, m_t T_x^{1/2}$	$c_1 \cdot c_2 \cdot c_4 \cdot c_5$
Pnnm	$m_x T_y^{1/2} T_t^{1/2}, m_y T_x^{1/2} T_t^{1/2}, m_t$	$c_1 \cdot c_2 \cdot c_3 \cdot c_4$
Pmnn	$m_x, m_y T_x^{1/2} T_t^{1/2}, m_t T_x^{1/2} T_y^{1/2}$	$c_3 \cdot c_4 \cdot c_5 \cdot c_6$
Pbcn	$m_x T_y^{1/2}, m_y T_t^{1/2}, m_t T_x^{1/2} T_y^{1/2}$	$c_1 \cdot c_3 \cdot c_5 \cdot c_6$
Pnca	$m_x T_y^{1/2} T_t^{1/2}, m_y T_t^{1/2}, m_t T_x^{1/2}$	$c_1 \cdot c_2 \cdot c_3 \cdot c_5$
Pnab	$m_x T_y^{1/2} T_t^{1/2}, m_y T_x^{1/2}, m_t T_y^{1/2}$	$c_1 \cdot c_2 \cdot c_4 \cdot c_6$
Pnna	$m_x T_y^{1/2} T_t^{1/2}, m_y T_x^{1/2} T_t^{1/2}, m_t T_x^{1/2}$	$c_1 \cdot c_2 \cdot c_3 \cdot c_4 \cdot c_5$
Pbnn	$m_x T_y^{1/2}, m_y T_x^{1/2} T_t^{1/2}, m_t T_x^{1/2} T_y^{1/2}$	$c_1 \cdot c_3 \cdot c_4 \cdot c_5 \cdot c_6$
Pcnn	$m_x T_t^{1/2}, m_y T_x^{1/2} T_t^{1/2}, m_t T_x^{1/2} T_y^{1/2}$	$c_2 \cdot c_3 \cdot c_4 \cdot c_5 \cdot c_6$
Pnnn	$m_x T_y^{1/2} T_t^{1/2}, m_y T_x^{1/2} T_t^{1/2}, m_t T_x^{1/2} T_y^{1/2}$	$\prod_{i=1}^{6} c_i$

Since c_2 and c_3 are related by $\rho = R_{\pi/2}$, 6 of total 8 group elements are inequivalent as space-time group types, listed in the third column of Table. 4.8. For the ACC $mm2P$, $H^1(mm2, T(3)/P) = \mathbb{Z}_2^4$ with the 4 generators reading,

$$\begin{aligned} c_1^{(16)}(m_x) &= \frac{1}{2}a_2^P, \quad & c_1^{(16)}(m_y) &= 0 \\ c_2^{(16)}(m_x) &= \frac{1}{2}a_3^P, \quad & c_2^{(16)}(m_y) &= 0 \\ c_3^{(16)}(m_x) &= 0, & c_3^{(16)}(m_y) &= \frac{1}{2}a_3^P \\ c_4^{(16)}(m_x) &= 0, & c_4^{(16)}(m_y) &= \frac{1}{2}a_1^P \end{aligned} \tag{4.21}$$

Given the equivalence condition ρ, c_1 is related to c_4, and c_2 is related c_3. Therefore the total 16 group elements give rise to 10 distinct types of space-time groups.

For the ACC $m1'P$, $H^1(mm2, T(3)/P)$ is also $\mathbb{Z}_2^4$ with the 4 generators reading,

$$\begin{aligned} c_1^{(17)}(m_y) &= \frac{1}{2}a_3^P, \quad & c_1^{(17)}(m_t) &= 0 \\ c_2^{(17)}(m_y) &= \frac{1}{2}a_1^P, \quad & c_2^{(17)}(m_y) &= 0 \\ c_3^{(17)}(m_y) &= 0, & c_3^{(17)}(m_t) &= \frac{1}{2}a_1^P \\ c_4^{(17)}(m_y) &= 0, & c_4^{(17)}(m_t) &= \frac{1}{2}a_2^P \end{aligned} \tag{4.22}$$

None of these generators are related and there are 16 distinct types for space-groups for this ACC.

For the ACC $mm21'P$ with the largest symmetry in this crystal system, the

cohomology group is isomorphic to $\mathbb{Z}_2^6$. The 6 generators read

$$\begin{aligned}
&c_1^{(18)}(m_x) = \frac{1}{2}a_2^P,\ c_1^{(18)}(m_y) = 0,\ c_1^{(18)}(m_t) = 0\\
&c_2^{(18)}(m_x) = \frac{1}{2}a_3^P,\ c_2^{(18)}(m_y) = 0,\ c_2^{(18)}(m_t) = 0\\
&c_3^{(18)}(m_x) = 0,\ c_3^{(18)}(m_y) = \frac{1}{2}a_3^P,\ c_3^{(18)}(m_t) = 0\\
&c_4^{(18)}(m_x) = 0,\ c_4^{(18)}(m_y) = \frac{1}{2}a_1^P,\ c_4^{(18)}(m_t) = 0\\
&c_5^{(18)}(m_x) = 0,\ c_5^{(18)}(m_y) = \frac{1}{2}a_3^P,\ c_5^{(18)}(m_t) = \frac{1}{2}a_1^P\\
&c_6^{(18)}(m_x) = 0,\ c_6^{(18)}(m_y) = \frac{1}{2}a_1^P,\ c_6^{(18)}(m_t) = \frac{1}{2}a_2^P
\end{aligned} \tag{4.23}$$

Under the equivalence relation, $c_1 \sim c_4$, $c_2 \sim c_3$ and $c_5 \sim c_6$, and there are 36 distinct types of the space-time groups out of the 64 group elements.

Now we consider the base-centered Bravais lattice. As explained in Fig. 4.6, different from the static counterpart, there are two base-centered Bravais lattices, t-base-centered and r-base-centered, in the space-time group classification depending on whether the base face perpendicular to the time axis or not. The lattice basis vectors of the t-base-centered Bravais lattice are

$$\begin{aligned}
a_1^{tB} &= \frac{1}{2}(x_0, y_0, 0)\\
a_2^{tB} &= \frac{1}{2}(x_0, -y_0, 0)\\
a_3^{tB} &= (0, 0, t_0)
\end{aligned} \tag{4.24}$$

The combination of the lattice and 4 MPGs leads to 4 ACCs and 15 space-time groups listed in Table. 4.11. The first cohomology group of ACC $m'm'2C$ is $\mathbb{Z}_2$ with the generator,

$$c_1^{(19)}(m_x m_t) = \frac{1}{2}a_3^P, c_1^{(19)}(m_y m_t) = 0. \tag{4.25}$$

There are two types of space-time group within this ACC, c_1 and the symmorphic one.

For the ACC $mm2C$, $H^1(mm2, T(3)/C) = \mathbb{Z}_2^2$ with the two generators,

$$\begin{aligned} c_1^{(20)}(m_x) &= \frac{1}{2}a_3^P, \quad c_1^{(20)}(m_y) = 0 \\ c_2^{(20)}(m_x) &= 0, \qquad c_2^{(20)}(m_y) = \frac{1}{2}a_3^P \end{aligned} \tag{4.26}$$

Under the equivalent condition, $c_1 \sim c_2$ and there are three space-time types within this ACC. For the ACC $m1'C$, $H^1(m1', T(3)/C) = \mathbb{Z}_2^2$ with the two generators,

$$\begin{aligned} c_1^{(21)}(m_x) &= \frac{1}{2}a_3^P, \quad c_1^{(21)}(m_t) = 0 \\ c_2^{(21)}(m_x) &= 0, \qquad c_2^{(21)}(m_t) = \frac{1}{2}a_1^P \end{aligned} \tag{4.27}$$

These two generators are not related and constitute 4 space-time group types. For the ACC $mm21'C$, $H^1(mm21', T(3)/C) = \mathbb{Z}_2^3$ with the three generators,

$$\begin{aligned} &c_1^{(22)}(m_x) = a_3^P/2, c_1^{(22)}(m_y) = 0, c_1^{(22)}(m_t) = 0 \\ &c_1^{(22)}(m_x) = 0,\ c_1^{(22)}(m_y) = a_3^P/2, c_1^{(22)}(m_t) = 0 \\ &c_1^{(22)}(m_x) = 0,\ c_1^{(22)}(m_y) = 0, c_1^{(22)}(m_t) = a_1^P/2 \end{aligned} \tag{4.28}$$

The generator c_1 is related to c_2 by R_π, and the three generators lead 6 types of space-time groups.

On the other hand, the lattice basis vectors of r-base-centered Bravais lattice take the following form,

$$\begin{aligned} a_1^{rB} &= (x_0, 0, 0) \\ a_2^{rB} &= \frac{1}{2}(0, y_0, t_0) \\ a_3^{rB} &= \frac{1}{2}(0, -y_0, t_0) \end{aligned} \tag{4.29}$$

There are 5 ACCs and 22 space-time groups, as listed in Table. 4.12. The MPG $m1'$ has two different ways acting on the lattice, depending on the orientation of the reflection

Table 4.11: Space-time groups in 2+1 dimensions for t-base-centered orthorhombic lattice. The fractional translation $T^{1/n}_{x,y,z}$ acts on the coordinate as $T^{1/n}_{x,y,t}(x,y,t) = (x,y,t) + a^P_{1,2,3}/n$, where $a^P_1 \sim a^P_3$ are the primitive lattice basis for the space-time orthorhombic crystal system defined in Eq. 4.19.

T-Base-Centered Orthorhombic		
ACC No.19: $m'm'2C$, $G_m(2)$: $m'm'2$, $H^1(m'm'2, T(3)/C) = \mathbb{Z}_2$		
$C222$	$m_x m_t, m_y m_t$	1
$C222_1$	$m_x m_t T_t^{1/2}, m_y m_t$	c_1
ACC No.20 : $mm2C$, $G_m(2)$: $mm2$, $H^1(mm2, T(3)/C) = \mathbb{Z}_2^2$		
$Cmm2$	m_x, m_y	1
$Cmc2_1$	$m_x, m_y T_t^{1/2}$	c_1
$Ccc2$	$m_x T_t^{1/2}, m_y T_t^{1/2}$	$c_1 \cdot c_2$
ACC No. 21 : $m1'C$, $G_m(2)$: $m1'$, $H^1(m1', T(3)/C) = \mathbb{Z}_2^2$		
$Cm2m$	m_x, m_t	1
$Cm2a$	$m_x, m_t T_x^{1/2}$	c_1
$Cc2m$	$m_x T_t^{1/2}, m_t$	c_2
$Cc2a$	$m_x T_t^{1/2}, T_x^{1/2} m_t$	$c_1 \cdot c_2$
ACC No.22 : $mm21'C$, $mm21'$, $H^1(mm21', T(3)/C) = \mathbb{Z}_2^3$		
$Cmmm$	m_x, m_y, m_t	1
$Cmcm$	$m_x, m_y T_t^{1/2}, m_t$	c_2
$Cmme$	$m_x, m_y, T_x^{1/2} m_t$	c_3
$Cmca$	$m_x, m_y T_t^{1/2}, m_t T_x^{1/2}$	$c_2 \cdot c_3$
$Cccm$	$m_x T_t^{1/2}, m_y T_t^{1/2}, m_t$	$c_1 \cdot c_2$
$Ccce$	$m_x T_t^{1/2}, m_y T_t^{1/2}, m_t T_x^{1/2}$	$c_1 \cdot c_2 \cdot c_3$

planes and the base face. In the ACC $m_x1'A$, the base face is within the reflection plane, while it is not in $m_y1'A$. In the r-base-centered Bravais lattice, x and y direction is not equivalent. In consequence, for each of the 5 ACCs, none of the generators of the first cohomology group are equivalent, and the number of space-time group within each ACC is the same as the order of $H^1(G_m, T(3)/A)$. The generators of each $H^1(G_m, T/A)$ are already listed in Table. 4.12 and not repeated here.

The face-centered orthorhombic lattice is obtained by including lattice points on each face of the primitive lattice, and the lattice basis are,

$$\begin{aligned} a_1^F &= \frac{1}{2}(x_0, y_0, 0) \\ a_2^F &= \frac{1}{2}(x_0, 0, t_0) \\ a_3^F &= \frac{1}{2}(0, y_0, t_0) \end{aligned} \tag{4.30}$$

The 4 ACCs and 7 space-time groups obtained by combining the translations generated by Eq. 4.30 and the 4 MPGs are listed in Table. 4.13. Each generators of the 4 cohomology groups are nonequivalent.

The body-centered orthorhombic lattice has one additional lattice point located at the center of the primitive Bravais lattice, and the corresponding lattice basis vectors are,

$$\begin{aligned} a_1^I &= \frac{1}{2}(-x_0, y_0, t_0) \\ a_2^I &= \frac{1}{2}(x_0, -y_0, t_0) \\ a_3^I &= \frac{1}{2}(x_0, y_0, -t_0) \end{aligned} \tag{4.31}$$

The 4 ACCs and 16 space-time groups are listed in Table. 4.14. For the ACC $mm2I$, the

Table 4.12: Space-time group in 2+1 dimension for r-base-centered orthorhombic lattice. The fractional translation $T^{1/n}_{x,y,z}$ acting on the coordinate as $T^{1/n}_{x,y,z}(x,y,z) = (x,y,z) + a^P_{1,2,3}/n$, where $a^P_1 \sim a^P_3$ are the primitive lattice basis for the orthorhombic crystal system defined in Eq. 4.19.

R-Base-Centered Orthorhombic		
ACC No.23: $m'm'2A$, $G_m(2)$: $m'm'2$, $H^1(m'm'2, T(3)/A) = \mathbb{Z}_2$		
$A222$	$m_y m_t, m_x m_t$	1
$A2_122$	$m_y m_t, T_x^{1/2} m_x m_t$	c_1
ACC No.24 : $m_y 1'A$, $G_m(2)$: $m1'$, $H^1(m1', T(3)/A) = \mathbb{Z}_2^2$		
$A2mm$	m_y, m_t	1
$A2_1ma$	$m_y, m_t T_x^{1/2}$	c_2
$A2_1am$	$m_y T_x^{1/2}, m_t$	c_1
$A2aa$	$m_y T_x^{1/2}, m_t T_x^{1/2}$	$c_1 \cdot c_2$
ACC No.25 : $m_x 1'A$, $G_m(2)$: $m1'$, $H^1(m1', T(3)/A) = \mathbb{Z}_2^2$		
$Am2m$	m_x, m_t	1
$Ab2m$	$m_x T_y^{1/2}, m_t$	c_1
$Am2a$	$m_x, m_t T_x^{1/2}$	c_2
$Ac2a$	$m_x T_t^{1/2}, m_t T_x^{1/2}$	$c_1 \cdot c_2$
ACC No.26 : $mm2A$, $G_m(2)$: $mm2$, $H^1(mm2A, T(3)/A) = \mathbb{Z}_2^2$		
$Amm2$	m_x, m_y	1
$Abm2$	$m_x T_y^{1/2}, m_y$	c_1
$Ama2$	$m_x, m_y T_x^{1/2}$	c_2
$Aba2$	$m_x T_y^{1/2}, m_y T_x^{1/2},$	$c_1 \cdot c_2$
ACC No.27 : $mm21'A$, $G_m(2)$: $mm21'$, $H^1(mm21'A, T(3)/A) = \mathbb{Z}_2^3$		
$Ammm$	m_x, m_y, m_t	1
$Aemm$	$m_x T_y^{1/2}, m_y, m_t$	c_1
$Amam$	$m_x, m_y T_x^{1/2}, m_t$	c_2
$Amma$	$m_x, m_y, m_t T_x^{1/2}$	c_3
$Abma$	$m_x T_y^{1/2}, m_y, m_t T_x^{1/2}$	$c_1 \cdot c_3$
$Abam$	$m_x T_y^{1/2}, m_y T_x^{1/2}, m_t$	$c_1 \cdot c_2$
$Amaa$	$m_x, m_y T_x^{1/2}, m_t T_x^{1/2}$	$c_2 \cdot c_3$
$Aeaa$	$m_x T_y^{1/2}, m_y T_x^{1/2}, m_t T_x^{1/2}$	$c_1 \cdot c_2 \cdot c_3$

Table 4.13: Space-time groups in 2+1 dimensions for face-centered orthorhombic lattices. The fractional translation $T^{1/n}_{x,y,t}$ acting on the coordinate as $T^{1/n}_{x,y,t}(x,y,t) = (x,y,t) + a^P_{1,2,3}/n$, where $a^P_1 \sim a^P_3$ are the primitive lattice basis for the space-time orthorhombic crystal class defined in Eq. 4.19.

Face-Centered Orthorhombic		
ACC No.28 : $m'm'2F$, $G_m(2)$: $mm2F$, $H^1(m'm'2, T(3)/F) = \mathbb{I}$		
$F222$	$m_x m_t, m_y m_t$	1
ACC No.29 : $mm2F$, $G_m(2)$: $mm2$, $H^1(mm2, T(3)/F) = \mathbb{Z}_2$		
$Fmm2$	m_x, m_y	1
$Fdd2$	$m_x T_y^{1/4} T_t^{1/4}, m_y T_x^{1/4} T_t^{1/4}$	c_1
ACC No.30 : $m1'F$, $G_m(2)$: $m1'$, $H^1(m1', T(3)/F) = \mathbb{Z}_2$		
$F2mm$	m_y, m_t	1
$F2dd$	$m_y T_x^{1/4} T_t^{1/4}, m_t T_x^{1/4} T_y^{1/4}$	c_1
ACC No.31 : $mm21'F$, $G_m(2)$: $mm21'$, $H^1(mm21', T(3)/F) = \mathbb{Z}_2$		
$Fmmm$	m_x, m_y, m_t	1
$Fddd$	$m_x T_y^{1/4} T_t^{1/4}, m_y T_x^{1/4} T_t^{1/4}, m_t T_x^{1/4} T_y^{1/4}$	c_1

cohomology group is $\mathbb{Z}_2^2$ with the two generators

$$\begin{aligned} c_1^{(33)}(m_x) = a_2^P/2, c_1^{(33)}(m_y) = 0 \\ c_2^{(33)}(m_x) = 0, c_2^{(33)}(m_y) = a_1^P/2 \end{aligned} \tag{4.32}$$

Under the equivalent relation, c_1 is related to c_2 and there are 3 space-time types. For the ACC $mm21'I$, the cohomology group is $\mathbb{Z}_2^2$. The three generators are

$$\begin{aligned} c_1^{(35)}(m_x) = a_2^P/2, c_1^{(35)}(m_y) = 0, c_1^{(35)}(m_t) = 0 \\ c_2^{(35)}(m_x) = 0, c_2^{(35)}(m_y) = a_1^P/2, c_2^{(35)}(m_t) = 0 \\ c_3^{(35)}(m_x) = 0, c_3^{(35)}(m_y) = 0, c_3^{(35)}(m_t) = a_1^P/2. \end{aligned} \tag{4.33}$$

Among the three generators, $c_1 \sim c_2$, and there are 6 types of space-groups.

Table 4.14: Space-time groups in 2+1 dimensions for body-centered orthorhombic lattices. The fractional translations $T^{1/n}_{x,y,t}$ act on the coordinate as $T^{1/n}_{x,y,t}(x,y,t) = (x,y,t) + a^P_{1,2,3}/n$, where $a^P_1 \sim a^P_3$ are the primitive lattice basis for the space-time orthorhombic crystal system defined in Eq. 4.19.

Body-Centered Orthorhombic		
ACC No.32 : $m'm'2I$, $G_m(2)$: $m'm'2$, $H^1(m'm'2, T(3)/I) = \mathbb{Z}_2$		
$I222$	$m_x m_t, m_y m_t$	1
$I2_12_12_1$	$m_x m_t T_y^{1/2} T_t^{1/2}, m_y m_t T_x^{1/2} T_y^{1/2}$	c_1
ACC No.33 : $mm2I$, $G_m(2)$: $mm2$, $H^1(mm2, T(3)/I) = \mathbb{Z}_2^2$		
$Imm2$	m_x, m_y	1
$Ima2$	$m_x, m_y T_x^{1/2}$	c_1
$Iba2$	$m_x T_y^{1/2}, m_y T_x^{1/2}$	$c_1 \cdot c_2$
ACC No.34 : $m1'I$, $G_m(2)$: $m1'$, $H^1(mm2, T(3)/I) = \mathbb{Z}_2^2$		
$I2mm$	m_y, m_t	1
$I2mb$	$m_y, m_t T_y^{1/2}$	c_2
$I2cm$	$m_y T_t^{1/2}, m_t$	c_1
$I2bc$	$m_y T_t^{1/2}, m_t T_y^{1/2}$	$c_1 \cdot c_2$
ACC No.35 : $mm21'I$, $G_m(2)$: $mm21'$, $H^1(mm21', T(3)/I) = \mathbb{Z}_2^3$		
$Immm$	m_x, m_y, m_t	1
$Imma$	$m_x, m_y, m_t T_x^{1/2}$	c_3
$Ibmm$	$m_x T_y^{1/2}, m_y, m_t$	c_1
$Ibam$	$m_x T_y^{1/2}, m_y T_x^{1/2}, m_t$	$c_1 \cdot c_2$
$Imcb$	$m_x, m_y T_t^{1/2}, m_t T_y^{1/2}$	$c_2 \cdot c_3$
$Ibca$	$m_x T_y^{1/2}, m_y T_t^{1/2}, m_t T_x^{1/2}$	$c_1 \cdot c_2 \cdot c_3$

4.3.7 Tetragonal Crystal System

The tetragonal crystal system has 4-fold rotational symmetry. In the space-time group classification, due to the absence of the rotational symmetry mixing space and time, the rotation plane has to be purely spatial. In consequence, there is one to one correspondence between the space groups and space-time groups in this crystal system. The relevant MPG symmetry operations are 4-fold rotation $R_{\pi/2}$, spatial reflection m_x and time reversal m_t. Seven MPGs constructed from these symmetry operations are assigned to this crystal system. They are 4, $4'$, $41'$, $4mm$, $4mm1'$, $4'm'm$ and $4m'm'$.

There are two Bravais lattices. The primitive one has the following the basis vectors,

$$\begin{aligned} a_1^P &= (u,0,0) \\ a_2^P &= (0,u,0) \\ a_3^P &= (0,0,t_0) \end{aligned} \tag{4.34}$$

The semi-direct products of the 7 MGPs and the translation generated by Eq. 4.34 lead to 8 arithmetic crystal classes and total 49 space-time groups listed in Table. 4.15 and 4.17.

The reason 7 MGPs lead to 8 arithmetic crystal class is that the MGP $4'm'm$ can act on the Bravais lattice in two different ways depending on the direction of the reflection line. In the first case, the reflection line is parallel to a_1^P or a_2^P, and the matrix representations of the two generators $R_{\pi/2}m_t$ and m, in term of the three lattice vectors, are

$$\mathcal{D}_1(R_{\pi/2}m_t) = \begin{pmatrix} 0 & -1 & 0 \\ 1 & 0 & 0 \\ 0 & 0 & -1 \end{pmatrix}, \mathcal{D}_1(m) = \begin{pmatrix} -1 & 0 & 0 \\ 0 & 1 & 0 \\ 0 & 0 & 1 \end{pmatrix}. \tag{4.35}$$

In the second case, the reflection is parallel to $a_1^P \pm a_2^P$, and the matrix representation of

the reflection is different from the first case,

$$\mathcal{D}_2(R_{\pi/2}m_t) = \begin{pmatrix} 0 & -1 & 0 \\ 1 & 0 & 0 \\ 0 & 0 & -1 \end{pmatrix}, \mathcal{D}_2(m) = \begin{pmatrix} 0 & 1 & 0 \\ 1 & 0 & 0 \\ 0 & 0 & 1 \end{pmatrix}. \tag{4.36}$$

These two cases actually belong to the same geometry crystal class but different arithmetic crystal classes.

The body-centered Bravais lattice is obtained by adding one more lattice point at the body center of the primitive lattice with the following basis vectors

$$\begin{aligned} a_1^I &= \frac{1}{2}(-u,u,t_0) \\ a_2^I &= \frac{1}{2}(u,-u,t_0) \\ a_3^I &= \frac{1}{2}(u,u,-t_0), \end{aligned} \tag{4.37}$$

Due to the same reason for the primitive lattice, there are also 8 arithmetic crystal classes, which is constituted of 19 space-time groups, as listed in Table. 4.18.

For all ACCs within the tetragonal crystal system, all the elements of the cohomology group are one-to-one corresponding to distinct space-time group types. All the generators are indicated in Table. 4.15, 4.17 and 4.18.

4.3.8 Trigonal Crystal System

The symmetry operation of the trigonal crystal system contains 3-fold rotation. Since rotations mixing space and time is forbidden, the plane of the 3-fold rotation is spatial. In consequence, the space-time groups in this crystal system have one to one correspondence to the 3D trigonal space groups.

There are two Bravais lattices, the primitive trigonal lattice and the rhombohedral

Table 4.15: Space-time groups in 2+1 dimensions for primitive tetragonal lattices (1). The fractional translation $T^{1/n}_{x,y,t}$ acting on the coordinate as $T^{1/n}_{x,y,t}(x,y,t) = (x,y,t) + a^P_{1,2,3}/n$, where $a^P_1 \sim a^P_3$ are the lattice basis for the space-time tetragonal crystal system defined in Eq. 4.34.

Primitive Tetragonal		
ACC No.36 : $4P$, $G_m(2):4$, $H^1(4,T(3)/P) = \mathbb{Z}_4$		
$P4$	$R_{\pi/2}$	1
$P4_1$	$R_{\pi/2}T_t^{1/4}$	c_1
$P4_2$	$R_{\pi/2}T_t^{1/2}$	c_1^2
$P4_3$	$R_{\pi/2}T_t^{3/4}$	c_1^3
ACC No.37 : $4'P$, $G_m(2):4$, $H^1(4',T(3)/P) = \mathbb{I}$		
$P\bar{4}$	$R_{\pi/2}m_t$	1
ACC No.38 : $41'P$, $G_m(2):41'$, $H^1(41',T(3)/P) = \mathbb{Z}_2^2$		
$P4/m$	$R_{\pi/2}, m_t$	1
$P4_2/m$	$R_{\pi/2}T_t^{1/2}, m_t$	c_1
$P4/n$	$R_{\pi/2}, m_t T_x^{1/2} T_y^{1/2}$	c_2
$P4_2/n$	$R_{\pi/2}T_t^{1/2}, m_t T_x^{1/2} T_y^{1/2}$	$c_1 \cdot c_2$
ACC No.39 : $4m'm'P$, $G_m(2):4m'm'$, $H^1(4m'm',T(3)/P) = \mathbb{Z}_4 \otimes \mathbb{Z}_2$		
$P422$	$R_{\pi/2}, m_x m_t$	1
$P42_12$	$R_{\pi/2}, m_x m_t T_x^{1/2} T_y^{1/2}$	c_1
$P4_122$	$R_{\pi/2}T_t^{1/4}, m_x m_t$	c_2
$P4_222$	$R_{\pi/2}T_t^{1/2}, m_x m_t$	c_2^2
$P4_322$	$R_{\pi/2}T_t^{3/4}, m_x m_t$	c_2^3
$P4_12_12$	$R_{\pi/2}T_t^{1/4}, m_x m_t T_x^{1/2} T_y^{1/2}$	$c_1 \cdot c_2$
$P4_22_12$	$R_{\pi/2}T_t^{1/2}, m_x m_t T_x^{1/2} T_y^{1/2}$	$c_1 \cdot c_2^2$
$P4_32_12$	$R_{\pi/2}T_t^{3/4}, m_x m_t T_x^{1/2} T_y^{1/2}$	$c_1 \cdot c_2^3$

Table 4.16: Space-time groups in 2+1 dimensions for primitive tetragonal lattices (2). The fractional translation $T^{1/n}_{x,y,t}$ act on the coordinate as $T^{1/n}_{x,y,t}(x,y,t) = (x,y,t) + a^P_{1,2,3}/n$, where $a^P_1 \sim a^P_3$ are the primitive lattice basis for the tetragonal crystal system defined in Eq. 4.34.

Primitive Tetragonal (*cont.*)		
ACC No.40 : $4mmP$, $G_m(2) : 4mm$, $H^1(4mm, T(3)/P) = \mathbb{Z}_2^3$		
$P4mm$	$R_{\pi/2}, m_x$	1
$P4_2mc$	$R_{\pi/2}T_t^{1/2}, m_x$	c_1
$P4bm$	$R_{\pi/2}, m_x T_x^{1/2} T_y^{1/2}$	c_2
$P4cc$	$R_{\pi/2}, m_x T_t^{1/2}$	c_3
$P4_2cm$	$R_{\pi/2}T_t^{1/2}, m_x T_t^{1/2}$	$c_1 \cdot c_3$
$P4nc$	$R_{\pi/2}, m_x T_x^{1/2} T_y^{1/2} T_t^{1/2}$	$c_2 \cdot c_3$
$P4_2bc$	$R_{\pi/2}T_t^{1/2}, m_x T_x^{1/2} T_y^{1/2}$	$c_1 \cdot c_2$
$P4_2nm$	$R_{\pi/2}T_t^{1/2}, m_x T_x^{1/2} T_y^{1/2} T_t^{1/2}$	$c_1 \cdot c_2 \cdot c_3$
ACC No.41 : $4'm'mP$, $G_m(2) : 4'm'm$, $H^1(4'm'm, T(3)/P) = \mathbb{Z}_2^2$		
$P\bar{4}2m$	$R_{\pi/2}m_t, m_x m_t$	1
$P\bar{4}2c$	$R_{\pi/2}m_t, m_x m_t T_t^{1/2}$	c_1
$P\bar{4}2_1m$	$R_{\pi/2}m_t, m_x m_t T_x^{1/2} T_y^{1/2}$	c_2
$P\bar{4}2_1c$	$R_{\pi/2}m_t, m_x m_t T_x^{1/2} T_y^{1/2} T_t^{1/2}$	$c_1 \cdot c_2$
ACC No.42: $4'mm'P$, $G_m(2) : 4'mm'$, $H^1(4'm'm, T(3)/P) = \mathbb{Z}_2^2$		
$P\bar{4}m2$	$R_{\pi/2}m_t, m_x$	1
$P\bar{4}c2$	$R_{\pi/2}m_t, m_x T_t^{1/2}$	c_1
$P\bar{4}b2$	$R_{\pi/2}m_t, m_x T_x^{1/2} T_y^{1/2}$	c_2
$P\bar{4}n2$	$R_{\pi/2}m_t, m_x T_x^{1/2} T_y^{1/2} T_t^{1/2}$	$c_1 \cdot c_2$

Table 4.17: Space-time groups in 2+1 dimensions for primitive tetragonal lattices (3). The fractional translation $T^{1/n}_{x,y,t}$ act on the coordinate as $T^{1/n}_{x,y,t}(x,y,t) = (x,y,t) + a^P_{1,2,3}/n$, where $a^P_1 \sim a^P_3$ are the primitive lattice basis for the tetragonal crystal system defined in Eq. 4.34.

Primitive Tetragonal (*cont.*)		
ACC No.43 : $4mm1'P$, $G_m(2) : 4mm1'$, $H^1(4mm1', T(3)/P) = \mathbb{Z}_2^4$		
$P4/mmm$	$R_{\pi/2}, m_x, m_t$	1
$P4_2/mmc$	$R_{\pi/2}T_t^{1/2}, m_x, m_t$	c_1
$P4/mbm$	$R_{\pi/2}, m_x T_x^{1/2} T_y^{1/2}, m_t$	c_2
$P4/mcc$	$R_{\pi/2}, m_x T_t^{1/2}, m_t$	c_3
$P4/nmm$	$R_{\pi/2}, m_x, m_t T_x^{1/2} T_y^{1/2}$	c_4
$P4/nbm$	$R_{\pi/2}, m_x T_x^{1/2} T_y^{1/2}, m_t T_x^{1/2} T_y^{1/2}$	$c_2 \cdot c_4$
$P4/mnc$	$R_{\pi/2}, m_x T_x^{1/2} T_y^{1/2} T_t^{1/2}, m_t$	$c_2 \cdot c_3$
$P4/ncc$	$R_{\pi/2}, m_x T_t^{1/2}, m_t T_x^{1/2} T_y^{1/2}$	$c_3 \cdot c_4$
$P4_2/nmc$	$R_{\pi/2}T_t^{1/2}, m_x, m_t T_x^{1/2} T_y^{1/2}$	$c_1 \cdot c_4$
$P4_2/mcm$	$R_{\pi/2}T_t^{1/2}, m_x T_t^{1/2}, m_t$	$c_1 \cdot c_3$
$P4_2/mbc$	$R_{\pi/2}T_t^{1/2}, m_x T_x^{1/2} T_y^{1/2}, m_t$	$c_1 \cdot c_2$
$P4_2/nbc$	$R_{\pi/2}T_t^{1/2}, m_x T_x^{1/2} T_y^{1/2}, T_x^{1/2} T_y^{1/2} m_t$	$c_1 \cdot c_2 \cdot c_4$
$P4/nnc$	$R_{\pi/2}, m_x T_x^{1/2} T_y^{1/2} T_t^{1/2}, m_t T_x^{1/2} T_y^{1/2}$	$c_2 \cdot c_3 \cdot c_4$
$P4_2/mnm$	$R_{\pi/2}T_t^{1/2}, m_x T_x^{1/2} T_y^{1/2} T_t^{1/2}, m_t$	$c_1 \cdot c_2 \cdot c_3$
$P4_2/ncm$	$R_{\pi/2}T_t^{1/2}, m_x T_t^{1/2}, m_t T_x^{1/2} T_y^{1/2}$	$c_1 \cdot c_3 \cdot c_4$
$P4_2/nnm$	$R_{\pi/2}T_t^{1/2}, m_x T_x^{1/2} T_y^{1/2} T_t^{1/2}, T_x^{1/2} T_y^{1/2} m_t$	$\prod_{i=1}^{4} c_i$

Table 4.18: Space-time groups in 2+1 dimensions for body-centered-tetragonal lattices. The fractional translation $T^{1/n}_{x,y,z}$ act on the coordinate as $T^{1/n}_{x,y,t}(x,y,t) = (x,y,t) + a^P_{1,2,3}/n$, where $a^P_1 \sim a^P_3$ are the primitive lattice basis for the space-time tetragonal crystal system defined in Eq. 4.34.

Body-Centered Tetragonal		
ACC No.44 : $4I$, $G_m(2):4$, $H^1(4,T(3)/I) = \mathbb{Z}_2$		
$I4$	$R_{\pi/2}$	1
$I4_1$	$R_{\pi/2}T_t^{1/4}$	c_1
ACC No.45 : $4'I$, $G_m(2):4'$, $H^1(4',T(3)/I) = \mathbb{I}$		
$I\bar{4}$	$R_{\pi/2}m_t$	1
ACC No.46 : $41'I$, $G_m(2):41'$, $H^1(41',T(3)/I) = \mathbb{Z}_2$		
$I4/m$	$R_{\pi/2}, m_t$	1
$I4_1/a$	$R_{\pi/2}T_t^{1/4}, m_t T_x^{1/2}$	c_1
ACC No.47 : $4m'm'I$, $G_m(2):4m'm'$, $H^1(4m'm',T(3)/I) = \mathbb{Z}_2$		
$I422$	$R_{\pi/2}, m_x m_t$	1
$I4_122$	$R_{\pi/2}T_t^{1/4}, m_x m_t$	c_1
ACC No.48 : $4mmI$, $G_m(2):4mm$, $H^1(4mm,T(3)/I) = \mathbb{Z}_2^2$		
$I4mm$	$R_{\pi/2}, m_x$	1
$I4cm$	$R_{\pi/2}, m_x T_t^{1/2}$	c_2
$I4_1cd$	$R_{\pi/2}T_t^{1/4}, m_x T_y^{1/2}$	c_1
$I4_1md$	$R_{\pi/2}T_t^{1/4}, m_x T_y^{1/2}T_t^{1/2}$	$c_1 \cdot c_2$
ACC No.49 : $4'mm'I$, $G_m(2):4'mm'$, $H^1(4'mm',T(3)/I) = \mathbb{Z}_2$		
$I\bar{4}m2$	$R_{\pi/2}m_t, m_x$	1
$I\bar{4}c2$	$R_{\pi/2}m_t, m_x T_t^{1/2}$	c_1
ACC No.50 : $4'mm'I$, $G_m(2):4'mm'$, $H^1(4'mm',T(3)/I) = \mathbb{Z}_2$		
$I\bar{4}2m$	$R_{\pi/2}m_t, m_x m_t$	1
$I\bar{4}2d$	$R_{\pi/2}m_t, m_x m_t T_x^{1/2}T_t^{1/4}$	c_1
ACC No.51 : $4mm1'I$, $G_m(2):4mm1'$, $H^1(4mm1',T(3)/I) = \mathbb{Z}_2^2$		
$I4/mmm$	$R_{\pi/2}, m_x, m_t$	1
$I4/mcm$	$R_{\pi/2}, m_x T_t^{1/2}, m_t$	c_2
$I4_1/amd$	$R_{\pi/2}T_t^{1/4}, m_x T_x^{1/2}, m_t T_x^{1/2}$	c_1
$I4_1/acd$	$R_{\pi/2}T_t^{1/4}, m_x T_x^{1/2}T_t^{1/2}, m_t T_x^{1/2}$	$c_1 \cdot c_2$

lattice. The primitive lattice basis vectors are

$$\begin{aligned} a_1^P &= (u, 0, 0) \\ a_2^P &= (-\frac{1}{2}u, \frac{\sqrt{3}}{2}u, 0) \\ a_3^P &= (0, 0, t_0). \end{aligned} \tag{4.38}$$

The rhombohedral lattice is obtained by including two additional lattice points trisecting the body diagonal of the primitive unit cell, with the lattice basis vectors

$$\begin{aligned} a_1^R &= (-\frac{u}{2}, -\frac{\sqrt{3}u}{6}, \frac{t_0}{3}) \\ a_2^R &= (\frac{u}{2}, -\frac{\sqrt{3}u}{6}, \frac{t_0}{3}) \\ a_3^R &= (0, \frac{\sqrt{3}u}{3}, \frac{t_0}{3}). \end{aligned} \tag{4.39}$$

There are 5 MPGs, 3, $6'$, $3m$, $3m'$ and $6'm'm$, leaving both the primitive lattice and the rhombohedra lattice invariant and therefore assigned to the trigonal crystal system.

The combination of the 5 MPGs and the primitive lattice defined in Eq. 4.38 gives rise to 8 arithmetic crystal classes because the three among the 5 MGPs, $3m$, $3m'$ and $6'm'm$, have two inequivalent ways acting on the lattice according to the orientation of the reflection plane. There are 18 space-time groups falling into the 8 arithmetic crystal classes for the primitive trigonal lattice.

On the other hand, there are only 5 arithmetic crystal classes for the rhombohedra lattice as there is no ambiguity on how the MGPs act on lattice basis in Eq. 4.39. There are total 6 space-time groups defined on the rhombohedra lattice, as listed in Table. 4.20.

All the generators of the first cohomology groups for each of the 13 ACCs are independent, and are listed in Table. 4.19 and 4.20.

Table 4.19: Space-time groups in 2+1 dimensions for primitive trigonal lattices. The fractional temporal translation $T_t^{1/n}$ acts on coordinate as $T_t^{1/n}(x,y,z) = (x,y,z) + a_3^P/n$, where $a_1^P \sim a_3^P$ are the primitive lattice basis for the space-time trigonal crystal system defined in Eq. 4.38.

Primitive Trigonal		
ACC No.52 : $3P$, $G_m(2):3$, $H^1(3,T(3)/P) = \mathbb{Z}_3$		
$P3$	$R_{2\pi/3}$	1
$P3_1$	$R_{2\pi/3}T_t^{1/3}$	c_1
$P3_2$	$R_{2\pi/3}T_t^{2/3}$	c_1^2
ACC No.53 : $6'P$, $G_m(2):6'$, $H^1(6',T(3)/P) = \mathbb{Z}_2$		
$P\bar{3}$	$R_{\pi/3}m_t$	1
ACC No.54 : $312P$, $G_m(2):3m'$, $H^1(3m',T(3)/P) = \mathbb{Z}_3$		
$P312$	$R_{2\pi/3}, m_x m_t$	1
$P3_112$	$R_{2\pi/3}T_t^{1/3}, m_x m_t$	c_1
$P3_212$	$R_{2\pi/3}T_t^{2/3}, m_x m_t$	c_1^2
ACC No.55 : $321P$, $G_m(2):3m'$, $H^1(3m',T(3)/P) = \mathbb{Z}_3$		
$P321$	$R_{2\pi/3}, m_y m_t$	1
$P3_121$	$R_{2\pi/3}T_t^{1/3}, m_y m_t$	c_1
$P3_221$	$R_{2\pi/3}T_t^{2/3}, m_y m_t$	c_1^2
ACC No.56 : $3m1P$, $G_m(2):3m$, $H^1(3m,T(3)/P) = \mathbb{Z}_2$		
$P3m1$	$R_{2\pi/3}, m_x$	1
$P3c1$	$R_{2\pi/3}, m_x T_t^{1/2}$	c_1
ACC No.57 : $31mP$, $G_m(2):3m$, $H^1(3m,T(3)/P) = \mathbb{Z}_2$		
$P31m$	$R_{2\pi/3}, m_y$	1
$P31c$	$R_{2\pi/3}, m_y T_t^{1/2}$	c_1
ACC No.58 : $6'm'mP$, $G_m(2):6'm'm$, $H^1(6'm'm,T(3)/P) = \mathbb{Z}_2$		
$P\bar{3}1m$	$R_{\pi/3}m_t, m_y$	1
$P\bar{3}1c$	$R_{\pi/3}m_t, m_y T_t^{1/2}$	c_1
ACC No.59 : $6'mm'P$, $G_m(2):6'm'm$, $H^1(6'm'm,T(3)/P) = \mathbb{Z}_2$		
$P\bar{3}m1$	$R_{\pi/3}m_t, m_x$	1
$P\bar{3}c1$	$R_{\pi/3}m_t, m_x T_t^{1/2}$	c_1

Table 4.20: Space-time groups in 2+1 dimensions for rhombohedral lattices. The fractional temporal translation $T_t^{1/n}$ acts on the space-time coordinate as $T_t^{1/n}(x,y,t) = (x,y,t) + a_3^P/n$, where $a_1^P \sim a_3^P$ are the primitive lattice basis for the trigonal crystal system defined in Eq. 4.38.

Rhombohedral		
ACC No.60 : $3R$, $G_m(2):3$, $H^1(3,T(3)/R) = \mathbb{I}$		
$R3$	$R_{2\pi/3}$	1
ACC No.61 : $6'R$, $G_m(2):6'$, $H^1(6',T(3)/R) = \mathbb{I}$		
$R\bar{3}$	$R_{\pi/3}m_t$	1
ACC No.62 : $3m'R$, $G_m(2):3m'$, $H^1(3m',T(3)/R) = \mathbb{I}$		
$R32$	$R_{2\pi/3}, m_x m_t$	1
ACC No.63 : $3mR$, $G_m(2):3m$, $H^1(3m,T(3)/R) = \mathbb{Z}_2$		
$R3m$	$R_{2\pi/3}, m_x$	1
$R3c$	$R_{2\pi/3}, m_x T_t^{1/2}$	c_1
ACC No.64 : $6'm'mR$, $G_m(2):6'm'm$, $H^1(6'm'm,T(3)/R) = \mathbb{Z}_2$		
$R\bar{3}m$	$R_{\pi/3}m_t, m_x$	1
$R\bar{3}c$	$R_{\pi/3}m_t, m_x T_t^{1/2}$	c_1

4.3.9 Hexagonal Crystal System

The symmetry of hexagonal crystal system involves 6-fold rotation. The rotation plane is purely spatial. This crystal system only contains the primitive Bravais lattice, generated by the following vectors

$$\begin{aligned} a_1^P &= (u,0,0) \\ a_2^P &= (-\frac{1}{2}u, \frac{\sqrt{3}}{2}u, 0) \\ a_3^P &= (0,0,t_0). \end{aligned} \tag{4.40}$$

There are 7 MGPs, 6, $61'$, $31'$, $6mm$, $6m'm'$, $6mm1'$ and $3m1'$, leaving the lattice invariant and assigned to the hexagonal crystal system. It is worth noting that the primitive hexagonal lattice is the same as the primitive trigonal lattice in Eq. 4.38. But the 7 MGPs

assigned to the hexagonal crystal system *only* act on the primitive lattice, while the 5 MPGs assigned to the trigonal crystal system are the symmetry groups of both primitive lattice and rhombohedral lattice. The 7 MGPs act on the primitive lattice unambiguously except $3m1'$ which has two inequivalent ways acting on the primitive lattice, giving rise to 8 ACCs. All the generators of the first cohomology groups for each of the 8 ACCs are independent, resulting in 27 space-time group types listed in Table. 4.22.

4.4 Conclusion

we have studied a novel class of $D+1$ dimensional crystal structures exhibiting the general space-time periodicities. Their momentum-energy Brillouin zones are $D+1$ dimensional torus and are typically momentum-energy entangled. The band dispersions exhibit non-trivial windings around the momentum-energy Brillouin zones. The space-time crystal structures are classified by the "space-time" symmetry groups, which extend the space group for static crystal structures by incorporating "time-screw" rotations and "time-glide" reflections. In 1+1D, a complete classification of the 13 space-time groups is performed. Space-time symmetries give rise to novel Kramers degeneracy independent of the half-integer spinor structure. The non-symmorphic space-time group operations lead to protected spectral degeneracies for the 2+1 D space-time lattices.

This chapter contains material from the following preprint being prepared for submission for publication: Shenglong Xu, Congjun Wu, "Space-time crystal and space-time group symmetry", arXiv:1703.03388 (2017). The dissertation author was the primary investigator and author of this paper.

Table 4.21: Space-time groups in 2+1 dimensions for primitive hexagonal lattices. The fractional temporal translation $T_t^{1/n}$ acts on the coordinate as $T_t^{1/n}(x,y,t) = (x,y,t) + a_3^P/n$, where $a_1^P \sim a_3^P$ are the primitive lattice basis for the space-time hexagonal crystal class defined in Eq. 4.40.

Primitive Hexagonal		
ACC No.65 : $6P$, $G_m(2):6$, $H^1(6,T(3)/P) = \mathbb{Z}_6$		
$P6$	$R_{\pi/3}$	1
$P6_1$	$R_{\pi/3}T_t^{1/6}$	c_1
$P6_2$	$R_{\pi/3}T_t^{1/3}$	c_1^2
$P6_3$	$R_{\pi/3}T_t^{1/2}$	c_1^3
$P6_4$	$R_{\pi/3}T_t^{2/3}$	c_1^4
$P6_5$	$R_{\pi/3}T_t^{5/6}$	c_1^5
ACC No.66 : $31'P$, $G_m(2):31'$, $H^1(31',T(3)/P) = \mathbb{I}$		
$P\bar{6}$	$R_{2\pi/3}, m_t$	1
ACC No.67 : $61'P$, $G_m(2):61'$, $H^1(61',T(3)/P) = \mathbb{Z}_2$		
$P6/m$	$R_{\pi/3}, m_t$	1
$P6_3/m$	$R_{\pi/3}T_t^{1/2}, m_t$	c_1
ACC No.68 : $6m'm'P$, $G_m(2):6m'm'$, $H^1(6m'm',T(3)/P) = \mathbb{Z}_6$		
$P6222$	$R_{\pi/3}, m_x m_t$	1
$P6_1222$	$R_{\pi/3}T_t^{1/6}, m_x m_t$	c_1
$P6_2222$	$R_{\pi/3}T_t^{1/3}, m_x m_t$	c_1^2
$P6_3222$	$R_{\pi/3}T_t^{1/2}, m_x m_t$	c_1^3
$P6_4222$	$R_{\pi/3}T_t^{2/3}, m_x m_t$	c_1^4
$P6_5222$	$R_{\pi/3}T_t^{5/6}, m_x m_t$	c_1^5
ACC No.69 : $6mmP$, $G_m(2):6mm$, $H^1(6mm,T(3)/P) = \mathbb{Z}_2^2$		
$P6mm$	$R_{\pi/3}, m_x$	1
$P6_3mc$	$R_{\pi/3}T_t^{1/2}, m_x$	c_1
$P6cc$	$R_{\pi/3}, m_x T_t^{1/2}$	c_2
$P6_3cm$	$R_{\pi/3}T_t^{1/2}, m_x T_t^{1/2}$	$c_1 \cdot c_2$

Table 4.22: Space-time groups in 2+1 dimensions for primitive hexagonal lattices (cont.). The fractional temporal translation $T_t^{1/n}$ acts on the coordinate as $T_t^{1/n}(x,y,t) = (x,y,t) + a_3^P/n$, where $a_1^P \sim a_3^P$ are the primitive lattice basis for the space-time hexagonal crystal class defined in Eq. 4.40.

Primitive Hexagonal (cont.)		
ACC No.70 : $3m_x1'P$, $G_m(2) : 3m1'$, $H^1(3m',T(3)/P) = \mathbb{Z}_2$		
$P\bar{6}m2$	$R_{2\pi/3}, m_x, m_t$	1
$P\bar{6}c2$	$R_{2\pi/3}, m_x T_t^{1/2}, m_t$	c_1
ACC No.71 : $3m_y1'P$, $G_m(2) : 3m1'$, $H^1(3m',T(3)/P) = \mathbb{Z}_2$		
$P\bar{6}2m$	$R_{2\pi/3}, m_y, m_t$	1
$P\bar{6}2c$	$R_{2\pi/3}, m_y T_t^{1/2}, m_t$	c_1
ACC No.72 : $6mm1'P$, $G_m(2) : 6mm1'$, $H^1(6mm1',T(3)/P) = \mathbb{Z}_2^2$		
$P6/mmm$	$R_{\pi/3}, m_x, m_t$	1
$P6_3/mcm$	$R_{\pi/3} T_t^{1/2}, m_x T_t^{1/2}, m_t$	c_1
$P6_3/mmc$	$R_{\pi/3} T_t^{1/2}, m_x, m_t$	c_2
$P6/mcc$	$R_{\pi/3}, m_x T_t^{1/2}, m_t$	$c_1 \cdot c_2$

Bibliography

[1] A. A. (Alekse Alekseevich) Abrikosov. *Fundamentals of the theory of metals*. North-Holland, 1988.

[2] Leon N. Cooper. Bound electron pairs in a degenerate fermi gas. *Phys. Rev.*, 104(4):1189–1190, 1956.

[3] Richard E. Prange and Steven M. Girvin, editors. *The Quantum Hall Effect*. Springer New York, 1990.

[4] Hilbert v. Löhneysen, Achim Rosch, Matthias Vojta, and Peter Wölfle. Fermi-liquid instabilities at magnetic quantum phase transitions. *Rev. Mod. Phys.*, 79(3):1015–1075, 2007.

[5] P. W. Anderson. Infrared catastrophe in fermi gases with local scattering potentials. *Phys. Rev. Lett.*, 18(24):1049–1051, 1967.

[6] Luca De'Medici, Jernej Mravlje, and Antoine Georges. Janus-Faced Influence of Hund's Rule Coupling in Strongly Correlated Materials. *Phys. Rev. Lett.*, 107(25):256401, 2011.

[7] Patrick Fazekas. *Lecture Notes on Electron Correlation and Magnetism*. WORLD SCIENTIFIC, 1999.

[8] J. E. Hirsch. Two-dimensional Hubbard model: Numerical simulation study. *Phys. Rev. B*, 31(7):4403–4419, 1985.

[9] J. Brad Marston and Ian Affleck. Large-n limit of the hubbard-heisenberg model. *Phys. Rev. B*, 39:11538–11558, 1989.

[10] C. Wu, D. Bergman, L. Balents, and S. Das Sarma. Flat bands and wigner crystallization in the honeycomb optical lattice. *Phys. Rev. Lett.*, 99:70401, 2007.

[11] Christopher Bradley and Arthur Cracknell. *The Mathematical Theory of Symmetry in Solids: Representation Theory for Point Groups and Space Groups (Oxford Classic Texts in the Physical Sciences)*. 2010.

[12] Steve M. Young and Charles L. Kane. Dirac Semimetals in Two Dimensions. *Phys. Rev. Lett.*, 115(12):126803, 2015.

[13] C. Wu. Orbital frustration and ordering in p-band mott insulators. *Phys. Rev. Lett.*, 100:200406, 2008.

[14] Andreas Mielke. Ferromagnetic ground states for the hubbard model on line graphs. *J. Phys. A: Math. Gen.*, 24(2):L73, 1991.

[15] Ching Kai Chiu, Jeffrey C Y Teo, Andreas P. Schnyder, and Shinsei Ryu. Classification of topological quantum matter with symmetries. *Rev. Mod. Phys.*, 88(3):1–63, 2016.

[16] Yi Li and F. D. M. Haldane. Topological nodal Cooper pairing in doped Weyl metals. *arXiv*, 1510.01730, 2015.

[17] E. C. Stoner. Collective electron ferromagnetism. *Proc. R. Soc. Lond. A*, 169(938):339, 1938.

[18] Clarence Zener. Interaction between the d-shells in the transition metals. ii. ferromagnetic compounds of manganese with perovskite structure. *Phys. Rev.*, 82:403–405, 1951.

[19] J. C. Slater. Ferromagnetism and the band theory. *Rev. Mod. Phys.*, 25:199–210, 1953.

[20] P. W. Anderson and H. Hasegawa. Considerations on double exchange. *Phys. Rev.*, 100:675–681, 1955.

[21] Elliott H. Lieb and Daniel Mattis. Theory of ferromagnetism and the ordering of electronic energy levels. *Phys. Rev.*, 125:164–172, 1962.

[22] Yosuke Nagaoka. Ferromagnetism in a narrow, almost half-filled s band. *Phys. Rev.*, 147:392–405, 1966.

[23] C. Herring. *Magnetism*. Academic, Berlin, 1966.

[24] John A. Hertz. Quantum critical phenomena. *Phys. Rev. B*, 14(3):1165–1184, 1976.

[25] K. K. Murata and S. Doniach. Theory of magnetic fluctuations in itinerant ferromagnets. *Phys. Rev. Lett.*, 29:285–288, 1972.

[26] Tôru Moriya. *Spin Fluctuations in Itinerant Electron Magnetism*, volume 56 of *Springer Series in Solid-State Sciences*. Springer, Berlin Heidelberg, 1985.

[27] J. E. Hirsch. Metallic ferromagnetism in a single-band model. *Phys. Rev. B*, 40:2354–2361, 1989.

[28] Andreas Mielke and Hal Tasaki. Ferromagnetism in the hubbard model–examples from models with degenerate single-electron ground states. *Commun. Math. Phys.*, 158:341, 1993.

[29] Hal Tasaki. Ferromagnetism in the hubbard models with degenerate single-electron ground states. *Phys. Rev. Lett.*, 69:1608–1611, 1992.

[30] A. J. Millis. Effect of a nonzero temperature on quantum critical points in itinerant fermion systems. *Phys. Rev. B*, 48(10):7183–7196, 1993.

[31] K. Baberschke, W. Noting, and M Donath, editors. *Band-Ferromagnetism*. Springer-Verlag, Berlin, 2001.

[32] D. Belitz, T. R. Kirkpatrick, and Thomas Vojta. How generic scale invariance influences quantum and classical phase transitions. *Rev. Mod. Phys.*, 77:579–632, 2005.

[33] J. Jackiewicz and K. S. Bedell. Quantum fluctuation driven first-order phase transition in weak ferromagnetic metals. *Philosophical Magazine*, 85:1755–1763, 2005.

[34] Hilbert v. Löhneysen, Achim Rosch, Matthias Vojta, and Peter Wölfle. Fermi-liquid instabilities at magnetic quantum phase transitions. *Rev. Mod. Phys.*, 79:1015–1075, 2007.

[35] Dmitrii L. Maslov and Andrey V. Chubukov. Nonanalytic paramagnetic response of itinerant fermions away and near a ferromagnetic quantum phase transition. *Phys. Rev. B*, 79:075112, 2009.

[36] Gang Chen and Leon Balents. Ferromagnetism in itinerant two-dimensional t_{2g} systems. *Phys. Rev. Lett.*, 110:206401, 2013.

[37] Yi Li, Elliott H. Lieb, and Congjun Wu. Exact results for itinerant ferromagnetism in multiorbital systems on square and cubic lattices. *Phys. Rev. Lett.*, 112:217201, 2014.

[38] Y. Sang, D. Belitz, and T. R. Kirkpatrick. Disorder dependence of the ferromagnetic quantum phase transition. *arXiv*, 1406.5745, 2014.

[39] Daniel C. Mattis. *The Theory of Magnetism Made Simple*. World Scientific, Singapore, 2006.

[40] R. A. Duine and A. H. MacDonald. Itinerant ferromagnetism in an ultracold atom fermi gas. *Phys. Rev. Lett.*, 95:230403, 2005.

[41] G.-B. Jo, Y.-R. Lee, J.-H. Choi, C. A. Christensen, T. H. Kim, J. H. Thywissen, D. E. Pritchard, and W. Ketterle. Itinerant Ferromagnetism in a Fermi Gas of Ultracold Atoms. *Science*, 325:1521–1524, 2009.

[42] Shizhong Zhang, Hsiang-hsuan Hung, and Congjun Wu. Proposed realization of itinerant ferromagnetism in optical lattices. *Phys. Rev. A*, 82:053618, 2010.

[43] I. Berdnikov, P. Coleman, and S. H. Simon. Itinerant ferromagnetism in an atom trap. *Phys. Rev. B.*, 79(22):224403, 2009.

[44] D. Pekker and E. Demler. Competing instabilities in quench experiments with ultracold Fermi gases near a Feshbach resonance. *arXiv*, 1107.3930, 2011.

[45] Chia-Chen Chang, Shiwei Zhang, and David M. Ceperley. Itinerant ferromagnetism in a fermi gas with contact interaction: Magnetic properties in a dilute hubbard model. *Phys. Rev. A*, 82:061603, 2010.

[46] Xiaoling Cui and Tin-Lun Ho. Ground-state ferromagnetic transition in strongly repulsive one-dimensional fermi gases. *Phys. Rev. A*, 89:023611, 2014.

[47] S. Pilati, I. Zintchenko, and M. Troyer. Ferromagnetism of a repulsive atomic fermi gas in an optical lattice: A quantum monte carlo study. *Phys. Rev. Lett.*, 112:015301, 2014.

[48] W. Kohn and L. J. Sham. Self-consistent equations including exchange and correlation effects. *Phys. Rev.*, 140:A1133–A1138, 1965.

[49] U. V. Barth and L. Hedin. A local exchange-correlation potential for the spin polarized case. i. *J. Phys. C: Solid State Phys*, 5:1629, 1972.

[50] V. L. Moruzzi, J. F. Janak, and A. R. Williams. *Calculated Electronic Properties of Metals*. Pergamon Press Inc., 1978.

[51] B. Himmetoglu, A. Floris, S. de Gironcoli, and M. Cococcioni. Hubbard-corrected DFT energy functionals: the LDA+U description of correlated systems. *arXiv*, 1309.3355, 2013.

[52] Antoine Georges, Gabriel Kotliar, Werner Krauth, and Marcelo J. Rozenberg. Dynamical mean-field theory of strongly correlated fermion systems and the limit of infinite dimensions. *Rev. Mod. Phys.*, 68:13–125, 1996.

[53] E. Gull, A. J. Millis, A. I. Lichtenstein, A. N. Rubtsov, M. Troyer, and P. Werner. Continuous-time Monte Carlo methods for quantum impurity models. *Rev. Mod. Phys.*, 83:349–404, 2011.

[54] K. Held, I. A. Nekrasov, G. Keller, V. Eyert, N. Blümer, A. K. McMahan, R. T. Scalettar, T. Pruschke, V. I. Anisimov, and D. Vollhardt. The LDA+DMFT Approach to Materials with Strong Electronic Correlations. *arXiv*, 0112079, 2001.

[55] Martin C. Gutzwiller. Effect of correlation on the ferromagnetism of transition metals. *Phys. Rev. Lett.*, 10:159–162, 1963.

[56] Jia Ning Zhuang, Lei Wang, Zhong Fang, and Xi Dai. Fast impurity solver based on gutzwiller variational approach. *Phys. Rev. B*, 79:165114, 2009.

[57] W. Weber, J. Bünemann, and F. Gebhard. *Band-Ferromagnetism*. Springer-Verlag, Berlin, 2001.

[58] B. S. Shastry, H. R. Krishnamurthy, and P. W. Anderson. Instability of the nagaoka ferromagnetic state of the $u = \infty$ hubbard model. *Phys. Rev. B*, 41:2375–2379, 1990.

[59] Guang-Shan Tian. Stability of the nagaoka state in the one-band hubbard model. *Phys. Rev. B*, 44:4444–4448, 1991.

[60] Hal Tasaki. Extension of nagaoka's theorem on the large-U hubbard model. *Phys. Rev. B*, 40:9192–9193, 1989.

[61] Li Liu, Hong Yao, Erez Berg, Steven R. White, and Steven A. Kivelson. Phases of the infinite u hubbard model on square lattices. *Phys. Rev. Lett.*, 108:126406, 2012.

[62] Z.-C. Gu, H.-C. Jiang, and G. Baskaran. Emergence of $p+ip$ superconductivity in $2D$ strongly correlated Dirac fermions. *arXiv*, 1408.6820, 2014.

[63] Tru Moriya and Arisato Kawabata. Effect of spin fluctuations on itinerant electron ferromagnetism. *Journal of the Physical Society of Japan*, 34(3):639–651, 1973.

[64] Joachim Stoehr and Hans Christoph Siegmann. *Magnetism, From Fundamentals to Nanoscale Dynamics*. Springer, 2006.

[65] P. Rhodes and E. P. Wohlfarth. The effective curie-weiss constant of ferromagnetic metals and alloys. *Proc. R. Soc. Lond. A*, 273:247–258, 1962.

[66] J. E. Hirsch. Metallic ferromagnetism in a single-band model. ii. finite-temperature magnetic properties. *Phys. Rev. B*, 40:9061–9069, 1989.

[67] C. Aron and G. Kotliar. Analytic theory of Hund's metals: a renormalization group perspective. *arXiv*, 1401.0331, 2014.

[68] Luca de Medici, S. R. Hassan, Massimo Capone, and Xi Dai. Orbital-selective mott transition out of band degeneracy lifting. *Phys. Rev. Lett.*, 102:126401, 2009.

[69] V. I. Anisimov, I. A. Nekrasov, D. E. Kondakov, T. M. Rice, and M. Sigrist. Localization in ruthenates: magnetic and electronic properties of $ca_{2-x}sr_xruo_4$. *Eur. Phys. J. B*, 25:191, 2002.

[70] A. Lichtenstein, M. Katsnelson, and G. Kotliar. Finite-Temperature Magnetism of Transition Metals: An ab initio Dynamical Mean-Field Theory. *Phys. Rev. Lett.*, 87(6):067205, 2001.

[71] N. D. Mermin and H. Wagner. Absence of Ferromagnetism or Antiferromagnetism in One- or Two-Dimensional Isotropic Heisenberg Models. *Phys. Rev. Lett.*, 17(22):1133–1136, 1966.

[72] Laura M. Roth. Simple narrow-band model of ferromagnetism due to intra-atomic exchange. *Phys. Rev.*, 149:306–308, 1966.

[73] KI Kugel and DI Khomskii. Crystal structure and magnetic properties of substances with orbital degeneracy. *Zh. Eksp. Teor. Fiz*, 64:1429–1439, 1973.

[74] M. Cyrot and C. Lyon-Caen. Orbital superlattice in the degenerate hubbard model. *J. Phys. France*, 36(3):253–266, 1975.

[75] A. M. Oleś. Antiferromagnetism and correlation of electrons in transition metals. *Phys. Rev. B*, 28:327–339, 1983.

[76] Anders W. Sandvik and Juhani Kurkijärvi. Quantum monte carlo simulation method for spin systems. *Phys. Rev. B*, 43:5950–5961, 1991.

[77] Naoki Kawashima and Kenji Harada. Recent developments of world-line monte carlo methods. *Journal of the Physical Society of Japan*, 73(6):1379–1414, 2004.

[78] Bernard Borodel Beard and U-J Wiese. Simulations of discrete quantum systems in continuous euclidean time. *Phys. Rev. Lett.*, 77(25):5130, 1996.

[79] Pinaki Sengupta, Anders W Sandvik, and David K Campbell. Bond-order-wave phase and quantum phase transitions in the one-dimensional extended hubbard model. *Phys. Rev. B*, 65(15):155113, 2002.

[80] Olav F. Syljuå sen and Anders W. Sandvik. Quantum Monte Carlo with directed loops. *Phys. Rev. E*, 66(4):046701, 2002.

[81] Maw Lin Foo, Yayu Wang, Satoshi Watauchi, H. W. Zandbergen, Tao He, R. J. Cava, and N. P. Ong. Charge ordering, commensurability, and metallicity in the phase diagram of the layered na_xCoo_2. *Phys. Rev. Lett.*, 92:247001, 2004.

[82] J. Merino, B. J. Powell, and Ross H. McKenzie. Ferromagnetism, paramagnetism, and a curie-weiss metal in an electron-doped hubbard model on a triangular lattice. *Phys. Rev. B*, 73:235107, 2006.

[83] Gregory A. Fiete. Colloquium. *Rev. Mod. Phys.*, 79:801–820, 2007.

[84] T. A. Zaleski and T. K. Kopeć. Antiferromagnetic order in the Hubbard model: Spin-charge rotating reference frame approach. In *Acta Phys. Pol. A*, volume 114, pages 247–251. American Physical Society, 2008.

[85] Daniel P. Arovas and Assa Auerbach. Functional integral theories of low-dimensional quantum heisenberg models. *Phys. Rev. B*, 38:316–332, 1988.

[86] Minoru Takahashi. Classical heisenberg ferromagnet in two dimensions. *Phys. Rev. B*, 36:3791–3797, 1987.

[87] A. Isacsson and S. M. Girvin. Multi-flavor bosonic Hubbard models in the first excited Bloch band of an optical lattice. *Phys. Rev. A*, 72:053604, 2005.

[88] W. V. Liu and C. Wu. Atomic matter of nonzero-momentum bose-einstein condensation and orbital current order. *Phys. Rev. A*, 74:13607, 2006.

[89] Lei Wang, Xi Dai, Shu Chen, and X. C. Xie. Magnetism of cold fermionic atoms on the *p* band of an optical lattice. *Phys. Rev. A*, 78:023603, 2008.

[90] Lu Li, C Richter, J Mannhart, and RC Ashoori. Coexistence of magnetic order and two-dimensional superconductivity at laalo3/srtio3 interfaces. *Nat. Phys.*, 7(10):762–766, 2011.

[91] Julie A Bert, Beena Kalisky, Christopher Bell, Minu Kim, Yasuyuki Hikita, Harold Y Hwang, and Kathryn A Moler. Direct imaging of the coexistence of ferromagnetism and superconductivity at the laalo3/srtio3 interface. *Nat. Phys.*, 7(10):767–771, 2011.

[92] S. Banerjee, O. Erten, and M. Randeria. Ferromagnetic exchange, spin-orbit coupling and spiral magnetism at the $LaAlO_3/SrTiO_3$ interface. *Nature Physics*, 9:626–630, 2013.

[93] Ian Affleck and J. Brad Marston. Large-n limit of the Heisenberg-Hubbard model: Implications for high-Tc superconductors. *Phys. Rev. B*, 37(7):3774–3777, 1988.

[94] N. Read and Subir Sachdev. Large- *N* expansion for frustrated quantum antiferromagnets. *Phys. Rev. Lett.*, 66:1773–1776, 1991.

[95] Subir Sachdev and N. Read. Large n expansion for frustrated and doped quantum antiferromagnets. *International Journal of Modern Physics B*, 05(01n02):219–249, 1991.

[96] N. Read and Subir Sachdev. Spin-peierls, valence-bond solid, and néel ground states of low-dimensional quantum antiferromagnets. *Phys. Rev. B*, 42:4568–4589, 1990.

[97] Arun Paramekanti and J B Marston. Su (n) quantum spin models: a variational wavefunction study. *Journal of Physics: Condensed Matter*, 19(12):125215, 2007.

[98] Michael Hermele, Victor Gurarie, and Ana Maria Rey. Mott insulators of ultracold fermionic alkaline earth atoms: Underconstrained magnetism and chiral spin liquid. *Phys. Rev. Lett.*, 103:135301, 2009.

[99] Carsten Honerkamp and Walter Hofstetter. Ultracold fermions and the SU(n) hubbard model. *Phys. Rev. Lett.*, 92:170403, 2004.

[100] Kenji Harada, Naoki Kawashima, and Matthias Troyer. Néel and spin-peierls ground states of two-dimensional SU(n) quantum antiferromagnets. *Phys. Rev. Lett.*, 90:117203, 2003.

[101] Philippe Corboz, Andreas M. Läuchli, Karlo Penc, Matthias Troyer, and Frédéric Mila. Simultaneous dimerization and su(4) symmetry breaking of 4-color fermions on the square lattice. *Phys. Rev. Lett.*, 107:215301, 2011.

[102] Philippe Corboz, Miklós Lajkó, Andreas M. Läuchli, Karlo Penc, and Frédéric Mila. Spin-orbital quantum liquid on the honeycomb lattice. *Phys. Rev. X*, 2(4):041013, 2012.

[103] Thomas C. Lang, Zi Yang Meng, Alejandro Muramatsu, Stefan Wessel, and Fakher F. Assaad. Dimerized Solids and Resonating Plaquette Order in SU(N)-Dirac Fermions. *Phys. Rev. Lett.*, 111(6):066401, 2013.

[104] Congjun Wu, Jiang-Ping Hu, and Shou-Cheng Zhang. Exact so(5) symmetry in the spin-$3/2$ fermionic system. *Phys. Rev. Lett.*, 91:186402, 2003.

[105] Congjun Wu. Hidden symmetry and quantum phases in spin-3/2 cold atomic systems. *Modern Physics Letters B*, 20(27):1707–1738, 2006.

[106] AV Gorshkov, M Hermele, V Gurarie, C Xu, PS Julienne, J Ye, P Zoller, E Demler, MD Lukin, and AM Rey. Two-orbital su (n) magnetism with ultracold alkaline-earth atoms. *Nature Physics*, 6(4):289–295, 2010.

[107] Hideaki Hara, Yosuke Takasu, Yoshifumi Yamaoka, John M. Doyle, and Yoshiro Takahashi. Quantum degenerate mixtures of alkali and alkaline-earth-like atoms. *Phys. Rev. Lett.*, 106:205304, 2011.

[108] Shintaro Taie, Yosuke Takasu, Seiji Sugawa, Rekishu Yamazaki, Takuya Tsujimoto, Ryo Murakami, and Yoshiro Takahashi. Realization of a SU$(2) \times$ SU(6) system of fermions in a cold atomic gas. *Phys. Rev. Lett.*, 105:190401, 2010.

[109] F. Scazza, C. Hofrichter, M. Höfer, P. C. De Groot, I. Bloch, and S. Fölling. Observation of two-orbital spin-exchange interactions with ultracold SU(N)-symmetric fermions. *Nat. Phys.*, 10(10):779–784, 2014.

[110] X. Zhang, M. Bishof, S. L. Bromley, C. V. Kraus, M. S. Safronova, P. Zoller, A. M. Rey, and J. Ye. Spectroscopic observation of SU(N)-symmetric interactions in Sr orbital magnetism. *Science*, 345(6203):1467–1473, 2014.

[111] Shintaro Taie, Rekishu Yamazaki, Seiji Sugawa, and Yoshiro Takahashi. An su(6) mott insulator of an atomic fermi gas realized by large-spin pomeranchuk cooling. *Nature Physics*, 8(11):825–830, 2012.

[112] Pedro M Duarte, Russell A Hart, Tsung-Lin Yang, Xinxing Liu, Thereza Paiva, Ehsan Khatami, Richard T Scalettar, Nandini Trivedi, and Randall G Hulet. Compressibility of a Fermionic Mott Insulator of Ultracold Atoms. *Phys. Rev. Lett.*, 114(7):070403, 2015.

[113] B. J. DeSalvo, M. Yan, P. G. Mickelson, Y. N. Martinez de Escobar, and T. C. Killian. Degenerate fermi gas of ^{87}Sr. *Phys. Rev. Lett.*, 105:030402, 2010.

[114] Ahmed Omran, Martin Boll, Timon A Hilker, Katharina Kleinlein, Guillaume Salomon, Immanuel Bloch, and Christian Gross. Microscopic Observation of Pauli Blocking in Degenerate Fermionic Lattice Gases. *Phys. Rev. Lett.*, 115(26):263001, 2015.

[115] Christian Hofrichter, Luis Riegger, Francesco Scazza, Moritz Höfer, Diogo Rio Fernandes, Immanuel Bloch, and Simon Fölling. Direct Probing of the Mott Crossover in the SU(N) Fermi-Hubbard Model. *Phys. Rev. X*, 6(2):021030, 2016.

[116] Guido Pagano, Marco Mancini, Giacomo Cappellini, Pietro Lombardi, Florian Schäfer, Hui Hu, Xia-Ji Liu, Jacopo Catani, Carlo Sias, Massimo Inguscio, and Leonardo Fallani. A one-dimensional liquid of fermions with tunable spin. *Nat. Phys.*, 10(3):198–201, 2014.

[117] Salvatore R. Manmana, Kaden R. A. Hazzard, Gang Chen, Adrian E. Feiguin, and Ana Maria Rey. Su(n) magnetism in chains of ultracold alkaline-earth-metal atoms: Mott transitions and quantum correlations. *Phys. Rev. A*, 84:043601, 2011.

[118] Laura Messio and Frédéric Mila. Entropy dependence of correlations in one-dimensional SU(n) antiferromagnets. *Phys. Rev. Lett.*, 109:205306, 2012.

[119] Kaden R. A. Hazzard, Victor Gurarie, Michael Hermele, and Ana Maria Rey. High-temperature properties of fermionic alkaline-earth-metal atoms in optical lattices. *Phys. Rev. A*, 85:041604, 2012.

[120] Lars Bonnes, Kaden R. A. Hazzard, Salvatore R. Manmana, Ana Maria Rey, and Stefan Wessel. Adiabatic loading of one-dimensional SU(n) alkaline-earth-atom fermions in optical lattices. *Phys. Rev. Lett.*, 109:205305, 2012.

[121] Ian Affleck and J. Brad Marston. Large- n limit of the heisenberg-hubbard model: Implications for high-T_c superconductors. *Phys. Rev. B*, 37:3774–3777, 1988.

[122] Jérôme Dufour, Pierre Nataf, and Frédéric Mila. Variational Monte Carlo investigation of SU (N) Heisenberg chains. *Phys. Rev. B*, 91(17):174427, 2015.

[123] Zi Cai, Hsiang-hsuan Hung, Lei Wang, Dong Zheng, and Congjun Wu. Pomeranchuk cooling of SU($2n$) ultracold fermions in optical lattices. *Phys. Rev. Lett.*, 110:220401, 2013.

[124] Zhichao Zhou, Zi Cai, Congjun Wu, and Yu Wang. Quantum Monte Carlo simulations of thermodynamic properties of SU(2N) ultracold fermions in optical lattices. *Phys. Rev. B*, 90(23):235139, 2014.

[125] Zhichao Zhou, Da Wang, Congjun Wu, and Yu Wang. Finite-temperature valence-bond-solid transitions and thermodynamic properties of interacting SU(2N) Dirac fermions. *Phys. Rev. B*, 95(8):085128, 2017.

[126] M. Z. Hasan and C. L. Kane. Colloquium: Topological insulators. *Rev. Mod. Phys.*, 82(4):3045–3067, 2010.

[127] Xiao-Liang Qi and Shou-Cheng Zhang. Topological insulators and superconductors. *Rev. Mod. Phys.*, 83(4):1057–1110, 2011.

[128] Takashi Oka and Hideo Aoki. Photovoltaic Hall effect in graphene. *Phys. Rev. B*, 79(8):081406, 2009.

[129] Zhenghao Gu, H. A. Fertig, Daniel P. Arovas, and Assa Auerbach. Floquet spectrum and transport through an irradiated graphene ribbon. *Phys. Rev. Lett.*, 107(21):216601, 2011.

[130] Netanel H. Lindner, Gil Refael, and Victor Galitski. Floquet topological insulator in semiconductor quantum wells. *Nat. Phys.*, 7(6):490–495, 2011.

[131] Gregor Jotzu, Michael Messer, Rémi Desbuquois, Martin Lebrat, Thomas Uehlinger, Daniel Greif, and Tilman Esslinger. Experimental realization of the topological Haldane model with ultracold fermions. *Nature*, 515(7526):237–240, 2014.

[132] Mikael C. Rechtsman, Julia M. Zeuner, Yonatan Plotnik, Yaakov Lumer, Daniel Podolsky, Felix Dreisow, Stefan Nolte, Mordechai Segev, and Alexander Szameit. Photonic Floquet topological insulators. *Nature*, 496(7444):196–200, 2013.

[133] Daniel Leykam, M. C. Rechtsman, and Y. D. Chong. Anomalous Topological Phases and Unpaired Dirac Cones in Photonic Floquet Topological Insulators. *Phys. Rev. Lett.*, 117(1):013902, 2016.

[134] Takuya Kitagawa, Erez Berg, Mark Rudner, and Eugene Demler. Topological characterization of periodically driven quantum systems. *Phys. Rev. B*, 82(23):235114, 2010.

[135] J. K. Asbóth, B. Tarasinski, and P. Delplace. Chiral symmetry and bulk-boundary correspondence in periodically driven one-dimensional systems. *Phys. Rev. B*, 90(12):125143, 2014.

[136] Rahul Roy and Fenner Harper. Periodic Table for Floquet Topological Insulators. *arXiv*, 1603.06944, 2016.

[137] Manisha Thakurathi, Aavishkar A. Patel, Diptiman Sen, and Amit Dutta. Floquet generation of Majorana end modes and topological invariants. *Phys. Rev. B*, 88(15):155133, 2013.

[138] Mark S. Rudner, Netanel H. Lindner, Erez Berg, and Michael Levin. Anomalous Edge States and the Bulk-Edge Correspondence for Periodically Driven Two-Dimensional Systems. *Phys. Rev. X*, 3(3):031005, 2013.

[139] Andrew C Potter and Takahiro Morimoto. Dynamically enriched topological orders in driven two-dimensional systems. *Phys. Rev. B*, 95(15):155126, 2017.

[140] Andrew C. Potter, Takahiro Morimoto, and Ashvin Vishwanath. Classification of Interacting Topological Floquet Phases in One Dimension. *Phys. Rev. X*, 6(4):041001, 2016.

[141] C. W. Von Keyserlingk and S. L. Sondhi. Phase structure of one-dimensional interacting Floquet systems. I. Abelian symmetry-protected topological phases. *Phys. Rev. B*, 93(24):245145, 2016.

[142] C. W. von Keyserlingk and S. L. Sondhi. Phase structure of one-dimensional interacting Floquet systems. II. Symmetry-broken phases. *Phys. Rev. B*, 93(24):245146, jun 2016.

[143] Dominic V. Else and Chetan Nayak. Classification of topological phases in periodically driven interacting systems. *Phys. Rev. B.*, 93(20):201103, 2016.

[144] Liang Fu. Topological Crystalline Insulators. *Phys. Rev. Lett.*, 106(10):106802, 2011.

[145] Siddharth A Parameswaran, Ari M Turner, Daniel P Arovas, and Ashvin Vishwanath. Topological order and absence of band insulators at integer filling in non-symmorphic crystals. *Nat. Phys.*, 9(5):299–303, 2013.

[146] Zhijun Wang, A. Alexandradinata, R. J. Cava, and B. Andrei Bernevig. Hourglass fermions. *Nature*, 532(7598):189–194, 2016.

[147] Haruki Watanabe, Hoi Chun Po, Michael P. Zaletel, and Ashvin Vishwanath. Filling-Enforced Gaplessness in Band Structures of the 230 Space Groups. *Phys. Rev. Lett.*, 117(9):096404, 2016.

[148] Edward Prince. *International Tables for Crystallography,Volume C: Mathematical, Physical and Chemical Tables*. International Union of Crystallography, 2004.

[149] Howard Hiller. Crystallography and Cohomology of Groups. *Am. Math. Mon.*, 93(10):765, 1986.

[150] Mois Ilia. Aroyo. *International tables for crystallography. Volume A. Space-group symmetry*. International Union of Crystallography, 2016.